Effects of interface morphology and geometry on the thermoelectric properties of artificially structured ZnO-based thin-films

Dissertation
zur Erlangung des Doktorgrades
der Naturwissenschaften
(Dr. rer. nat.)

vorgelegt von

Dipl.-Phys. Gert Homm

-anno 2012-

Betreuer:
Prof. Dr. P. J. Klar

Justus-Liebig-Universität Gießen
Fachbereich 07: I. Physikalisches Institut

Contents

1 Introduction

Since Thomas Seebeck discovered the Seebeck effect in 1821 [1] a lot of applications based on this effect have been developed. The most spreaded one surely is the very precise measurement of temperatures by forming a thermocouple out of two different metals. Practical applications for thermoelectric devices, however, only arised more than 100 years later in the mid 20th century, due to many advancements in semiconductor technology. To define the quality of a thermoelectric material, the so called figure of merit firstly was deduced by E. Altenkirch in 1910 to [2, 3]:

$$ZT = \frac{S^2\sigma}{\kappa}T. \tag{1.1}$$

Here S is the Seebeck coefficient, σ the electrical conductivity and κ the thermal conductivity. The higher the ZT-value of a material, the higher its efficiency in energy generation. As can be seen from equation (1.1), an improvement can be achieved by either increasing $S^2\sigma$ (the so called power factor) or by decreasing κ, without affecting the other parameters in an unwanted way. Assuming a constant Seebeck coefficient, the equation (1.1) implies that materials with a high electrical conductivity and a low thermal conductivity are desired, a design goal which, for metals, is somewhat contradicted by the Wiedemann-Franz law [4, 5]. This directly leads to semiconductors as the material class of choice for thermoelectrics. They have at least one order of magnitude higher Seebeck coefficients and further numerous advantages compared to metals can be named: The free carrier concentration can be adjusted by doping such that the electric conductivity is still fairly high, but the thermal conductivity is dominated by phonon transport. Simultaneously, the thermal conductivity can be reduced further by phonon blocking almost without affecting the free carrier transport [6]. This ansatz is known as the so called "phonon glass/electron crystal" (PGEC) introduced by Slack [7]. In the framework of this model a thermal conductivity comparable to the low thermal conductivity of amorphous materials such as glasses at a simultaneously high moblity of the charge carriers as in crystals are basically compatible. One approach for introducing local "glass-like" modes into a crystal are crystal structures like the skutterudites which contain cage-like units randomly occupied by heavy atoms which vibrate within these cages. These rattling atoms then cause a scattering of extended phonon states which drastically lowers the thermal conductivity of the lattice. One indication for such rattling atoms can be a strongly increased atomic displacement parameter [8, 9]. The PGEC concept encouraged numerous new research which ended up in a significant enhancement of ZT for some alloys, e.g. clathrates [10–14].

Theory predicts that the thermoelectric figure of merit could be significantly enhanced by reducing the dimensions of the used material down to a scale where confinement effects occur in one or more dimensions [15–17]. This idea came up in the 1990's, at a time when a lot of progress already had been made in the techniques of microfabrication in the Si-based computer chip industry. In this way a totally new playground for experimentalists was accessible. Various methods have been developed to manipulate the thermoelectric parameters on different length scales: One fairly simple and effective way of improving the

thermoelectric figure of merit is to take a thermoelectric bulk material, e.g. PbTe, and then try to improve it by ball milling and subsequent compacting. This method turned out to further improve the ZT-value of the bulk material due to a lowering of the thermal conductivity by introducing interfaces, while the electrical conductivity and the Seebeck coefficient remained high [6].

A more defined way of introducing interfaces in the thermoelectric material is to grow multilayers. The thermoelectric properties are then measured in cross-plane direction, i. e. perpendicular to the sample surface. High figures of merit could be achieved this way [18, 19], but the sample preparation is comparatively complex, and so is the thermoelectric characterization. In addition the reproducibility with the same degree of quality is crucial for a mass application in devices. Here the interfaces need to be controllable and tuneable in their shape, morphology, and transport properties. But a high degree of reproducability is not as trivial as it may sound, and in the cases ([18, 19]) cited above it could not be achieved yet [20, 21].

For some applications, an in-plane geometry is more desirable. An elegant way to introduce well defined interfaces in-plane by a relatively simple process is the lateral structuring of thin-films with alternating materials. Calculations show that for materials with incompatible phonon dispersion relations, the propagation of phonons of certain energies across the interfaces is suppressed [22–29]. This shows that interfaces may affect the electric as well as the phononic transport in a way that the thermal conductivity may be reduced by selective interface scattering, where phonons are blocked without disturbing the movement of the electrons. So the local structure of interfaces between two materials is very important for the transport on the mesoscopic to microscopic scale. Studying these effects yields a better understanding of the global behaviour of the macroscopic sample.

Motivated by this idea a sample preparation process was developed in the course of this work that uses photolithography and self-aligned pattern transfer for defining lateral interfaces in thin-film structures. This will be described in detail in chapter 4. This work shows the impact of interfaces on the thermoelectric transport properties. As indicated in figure 1.1 there are different length scales one has to take into account when discussing the observed effects. ZnO is an ideal model system for studying the effects of micro- and nanostructuring on the thermoelectric properties. As an oxide it is stable up to high temperatures. Furthermore ZnO is environmentally friendly, non toxic and available in abundance, all properties that are important for a possible use in long term industrial aplications. This topic is highlighted in chapter 2.

Depending on the demand of the quality, ZnO can be synthesized by various methods (sputter deposition, molecular beam epitaxy (MBE), chemical vapour deposition (CVD), etc.). This, of course has an impact on the thermoelectric behaviour. Parameters like doping concentration, carrier mobility, crystallinity, layer thickness, crystal axis orientation, purity, etc. can be tuned in a controlled way during the growth. A closer look at the impact of these parameters on the Seebeck coefficient is taken in chapter 6. Here it turns out that ZnO can be deposited with very high S up to -400 μVK^{-1} at room temperature. This is a very important property for a thermoelectric material, because the figure of merit Z is proportional to the square of the Seebeck coefficient (cf. equation (1.1)).

Unfortunately its bulk thermal conductivity (κ) with values around 100 $Wm^{-1}K^{-1}$ is very high for a thermoelectric material [30]. These high values can be reduced drastically by using compressed ZnO powder or sintered ZnO [31–34]. Furthermore dual doping with Al and Ga showed a reduction of the thermal conductivity down to a value of 13 $Wm^{-1}K^{-1}$ at room temperature altogether yielding quite high ZT-values of around

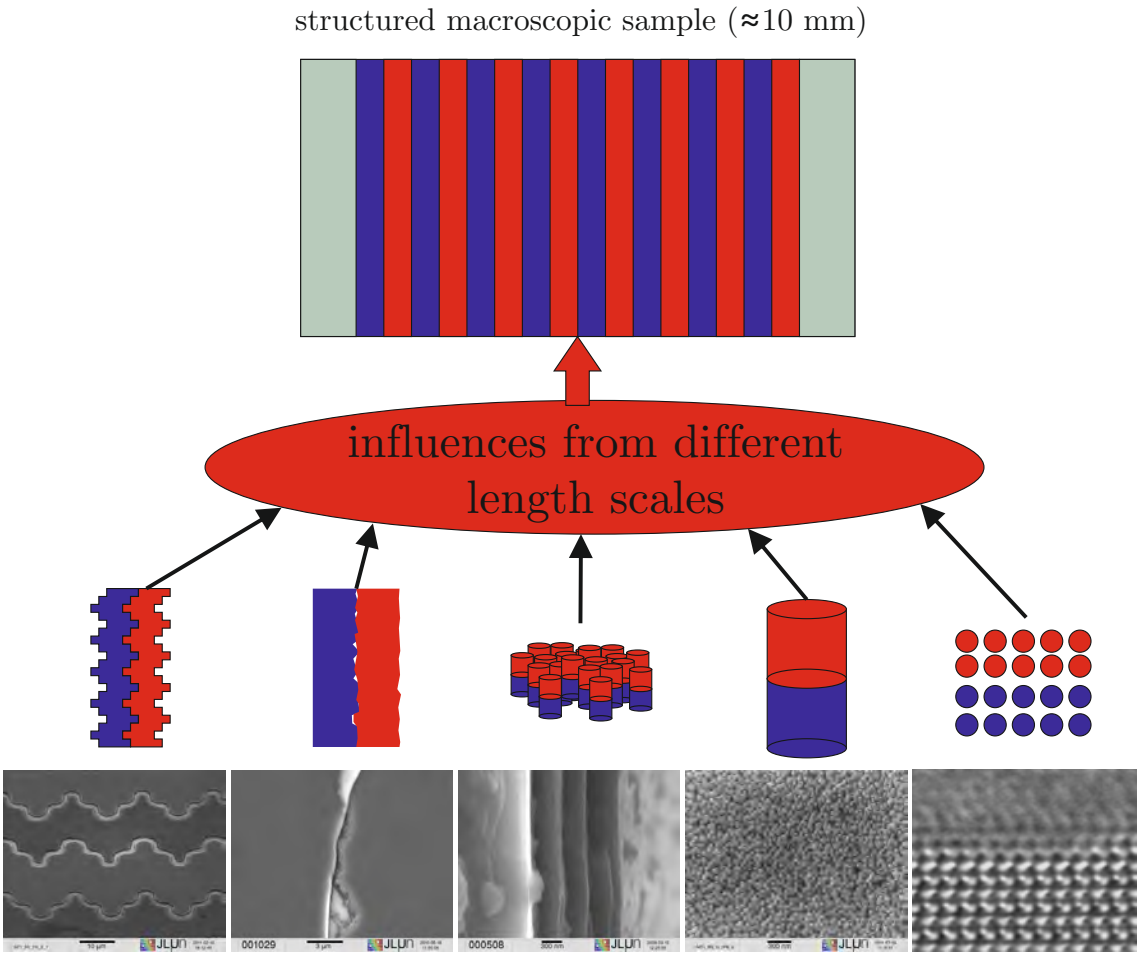

Figure 1.1: Interfaces with different length scales that affect the macroscopic transport behaviour of an artificially structured sample. The dimensions reach from a few micrometer (artificial roughness of the interface shown on the left) down to few Ångström (atomic interface between two materials shown on the right)

0.65 at 1247 K [35]. This means a further reduction of the thermal conductivity by a factor of two or more without reducing the powerfactor $S^2\sigma$ is necessary to raise the ZT-value above 1, making ZnO an attractive material for industrial applications.

For multilayer growth, investigations have already shown that a proper control of the quality of the interfaces between the stacked layers is of major importance for the device performance [36, 37]. For in-plane interfaces, however, a proper characterization is still missing. This gap could be closed a little further, when like in this work multilayers in in-plane geometry are studied. Our findings are discussed in section 6.4. To my knowledge, so far, only investigations of grain boundaries have been reported, in which the interfaces were arranged randomly [38–41]. This procedure has been applied to ZnO as well, with similar results, namely the reduction of the thermal conductivity by growing a highly disordered polycristalline material, i. e., by introducing additional interfaces [42–44]. Studies of sputtered ZnO layers exhibiting many grain boundaries have been performed during this work, as well. Their influence on the Seebeck coefficient and the electrical conductivity are discussed in section 6.2.

To characterize a material thermoelectrically, it is necessary to determine its transport coeffients S, σ and κ. In order to understand the effect of microstructuring not just macroscopically but also to analyse the local microscopic influences on the entire sample these coefficients need to be measured globally and locally. Further investigation methods like Raman-spectroscopy reveal information about electronic and vibrational modes of the lattice. An overview about the characterization methods used during this work can be found in chapter 3.

2 Thermoelectricity - a niche application or a real supplementation to regenerative energy production?

So far the world's energy production still mostly weighs on fossil fuels like coal, oil and gas. Almost 90 % of the energy worldwide still is generated from those greenhouse gas producing raw materials [45]. With a 'business as usual' trajectory [46] the amount of carbon dioxide will grow with the amount of produced energy from fossil fuels. This amount again depends on that fraction of the world's population having access to these energy resources. Since this part of the world's population is growing faster and faster the CO_2 amount is expected to increase considerably. To prevent dangerous and potentially irreversible alterations to the world's climate we have to keep the CO_2 content below 500 ± 50 parts per million (ppm), or in other words lower than twice the preindustrial concentration of 280 ppm [46]. Since the actual concentration lies at about 375 ppm [46] the critical concentration will be reached within a few years if no other strategies are developed. Thus, it is about time to think about alternative, carbon free and, in particular, renewable ways of energy production in addition to the fossil fuel consuming ones, to at least stop the rising of the atmosphere's carbon dioxide concentration and to satisfy the needs of the world's population.

Calculations show, that in order to keep this level of CO_2 concentration, a carbon-free power production of about 10 terawatts (TW) by the year 2050 will be necessary [47]. In the year 2008 the cumulative global solar energy production was about 14 GW (see figure 2.1). The predicted energy production from solar cells for the year 2012 worldwide is expected to be 20 GW [48]. This corresponds to a growth rate of 43 % over a time period of four years. Assuming this growth rate can be kept, the global solar energy production by the year 2050 will be about 600 GW. This is far below the required value of 10 TW. To achieve this amount of energy solely by photovoltaics (PV), a growth rate of about 87 % is necessary. This is more than twice the actual growth rate. Next to this considerable challenge there are more problems concerning the scarcity of materials used in many types of solar cells. In this framework work by Feltrin et al. [49] has been presented. Here it is shown, that depending on the technology and thus the materials used, only a few PV-module types are suitable for mass production, necessary to achieve the TW scale.

This makes clear that such a huge amount of energy cannot be provided by just one alternative resource but has to be achieved by a mixture of CO_2-free power production such as wind power, water power, nuclear power, and photovoltaics.

Concerning the nuclear power, the latest incidences in Japan have shown that this type of energy production includes another threat to the world's climate, namely the potential atomic fallout caused by a worst-case scenario of a nuclear power plant accident. This happened in Fukushima and initiated the German government to accelerate the abolition of nuclear power production. It is planned to shut down the last nuclear power plant in Germany and hence to be dissociated from nuclear energy production by the year 2022. It

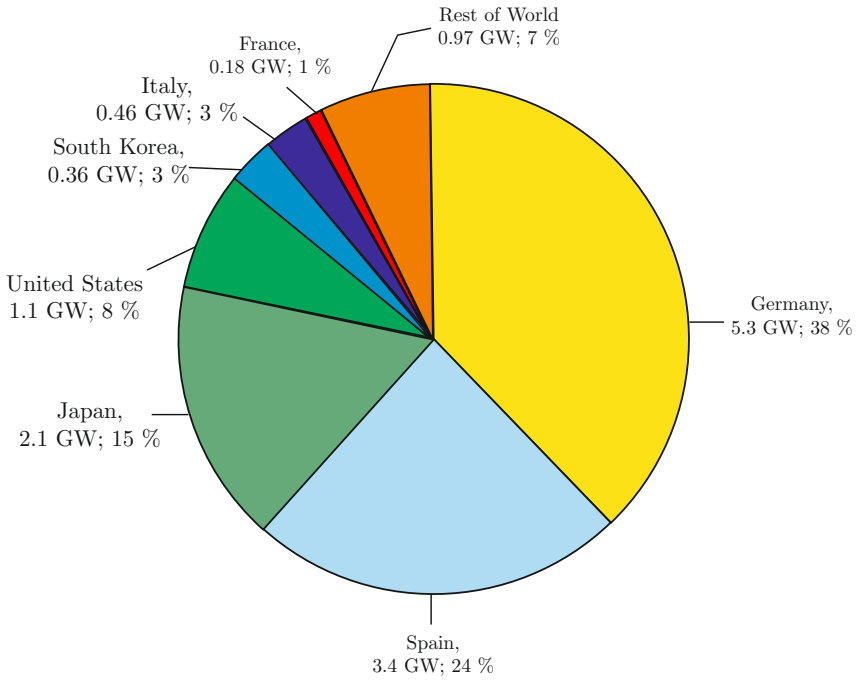

Figure 2.1: Global cumulative installed photovoltaic capacity in Gigawatt (GW) and percentage through 2008 (after [48]).

is obvious that this will cause a huge lack in energy supply since energy from nuclear power comprises about 20 % of Germany's total energy demand. The government assures people that this lack will be compensated totally by regenerative energy sources like photovoltaics, wind or water power and not by importing electricity from other countries, which may rise foreign nuclear power production to comply with this demand. In the first half of 2011, however, this plan seems to fail since Germany's imports of electric power for instance from France and the Czech Republic were increased by 51 % and 673 %, respectively, due to the shutdown of eight nuclear power plants [50]. Of course, most of the imported energy stems from nuclear energy. So the compensation of the energy demand in the meantime will be satisfied by either going back to a reinforced use of fossil fuels or a rise of nuclear power imports.

An alternative is to save energy by increasing the efficiency of devices and machines. This can generate at least as much benefit as the carbon-free energy production. In this context thermoelectricity may play an important role due to its ability to recycle at least a small fraction of otherwise wasted heat. Such wasted heat occurs intrinsicly in every industrial process because of friction and/or the combustion of fossil fuels. For example only one third of the energy of the gasoline burned in a car engine is effectively used to really move the car. The other two thirds are waste heat. So a tangible upcoming application of thermoelectric modules as mass products is an employment in cars for converting parts of the exhaust heat for cooling and heating of the passenger compartment. This will also allow one to replace conventional air conditioning in cars. The anticipated direct merits are more passenger comfort due to the possibility of zonal heating, a reduction of the fuel consumption by several percent, a reduction of weight, and less maintainance costs. Another positive side effect and driving force is the prevention of escaping of

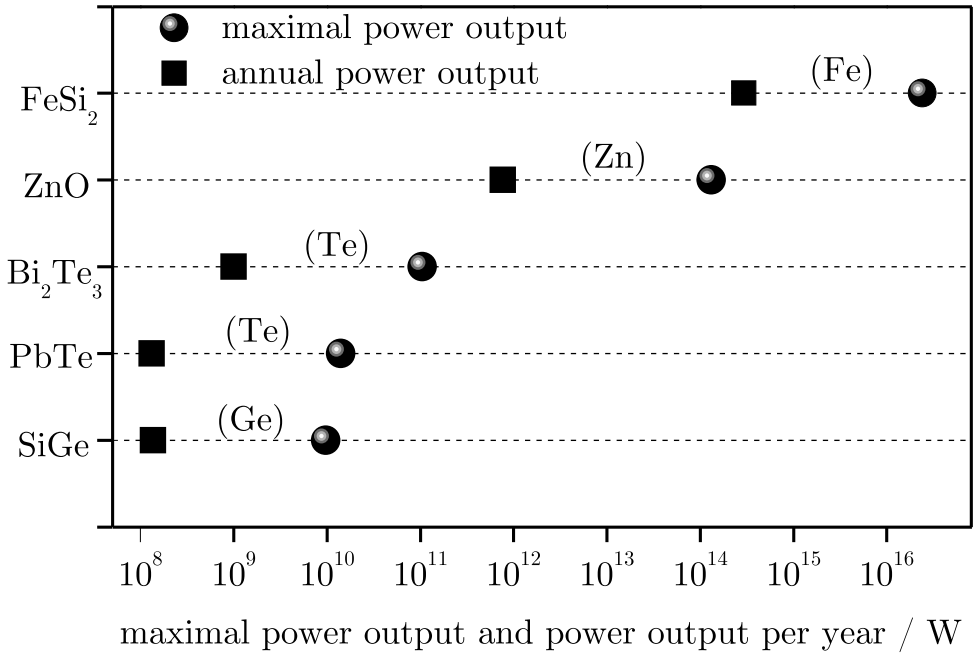

Figure 2.2: Overview of the maximal power output and annual power output based on the world's resources and annual production of the least abundant constituting elements for various thermoelectric material systems.

the refrigerant gas R134a ($C_2H_2F_4$), which is commonly employed in conventional air conditioning systems, into the atmosphere. This refrigerant gas has a 1430 times higher 'greenhouse gas effect' than CO_2. Car companies such as BMW, Chevrolet, Ford etc. pursue research of this topic actively.

The probably best understood and in terms of industrial application most used thermoelectric materials right now are Bi_2Te_3, PbTe, SiGe alloys. These materials have their optimum operation points in a different temperature range (Bi_2Te_3 up to about 250 °C, PbTe up to 550 °C and SiGe operates between 750 °C and 1000 °C [51]) and hence do not directly compete against each other. But looking at these materials in terms of sustainability, toxicity or other aspects concerning an industrial mass production, advantages or disadvantages need to be carefully considered. A very important point for a mass production of thermoelectric generators is the availability of each component that forms the compound of interest. Taking Bi_2Te_3 as an example, calculations show that devices based on this material would be able to produce approximately 105 GW of output power as maximum producable power based on material resources [52]. The maximum power output together with the annual power output based on the world's resources and annual production of the least abundant constituting element for various thermoelectric material systems is shown in figure 2.2. As can be seen tellurium is the limiting material in the two thermoeletric systems Bi_2Te_3 and PbTe. It is so scarce that Te-based active thermoelectric materials are only supposed to be a transitional technology until environmentally friendly and sustainable alternatives are found, as will be elaborated later in the section about ***mobile mass production***.

In general, the application of thermoelectric generators in systems can be divided in

three different types of usage: (i) energy harvesting based on the use of waste heat, i.e. the thermoelectric module does not interfere with the system or process causing the waste heat (ii) exergetic enhancement, i.e. incorporating thermoelectric devices into systems to utilize heat flows within the system in order to increase the electricity output and, thus, deliberately interfering with the system or process; and (iii) dedicated independent energy systems based on thermoeletric devices. Although the design target is always simply 'stable and sustainable performance', the actual design of a thermoeletric energy system is very complex. Many aspects need to be taken into account ranging from heat source properties via user requirements and system design aspects to the thermoelectric materials employed.

To find the most effective thermoelectric device is not always leading to the desired result to search for the material system with the highest ZT value in a given temperature range. A device with a maximum ZT of the material employed in the temperature interval ΔT between hot end at T_h and cold end at T_c of the working range possesses effectively a ZT value of about 70% of the maximum value averaged over the working range [53]. This is primarily because all thermoelectric material properties (S, κ, σ) depend on temperature and, furthermore, additional contact resistances and heat losses come into play in thermoelectric generator devices. Only in case of the usually unrealistic assumptions of temperature independent thermoelectric properties and of a perfect match between n-type and p-type legs, the average ZT of the device is given by the ZT of the material in equation (1.1). To estimate the efficiency of the thermoelectric generators of the different materials, for simplicity, T_h is fixed at the temperature where ZT is maximal which is somewhat similar to the maximum operating temperatures of corresponding thermoelectric devices. The idealized maximum power-generation efficiency for three different ΔT, i.e. different values of T_c is calculated. The idealized efficiency is then given by:

$$\eta = \frac{\Delta T}{T_\mathrm{h}} \cdot \frac{\sqrt{1 + ZT_\mathrm{h}} - 1}{\sqrt{1 + ZT_\mathrm{h}} + T_\mathrm{c}/T_\mathrm{h}}, \tag{2.1}$$

where ZT_h is defined by equation (1.1). $\Delta T/T_\mathrm{h}$ corresponds to the Carnot efficiency. A plot of η versus ZT for the five thermoelectric materials for three different temperature gradients ΔT is shown in figure 2.3. The corresponding values of η, ZT_h, and T_c are listed in table 2.1. Here for each of the five material systems the three different efficiencies η have been derived. For all materials the hotside temperature T_h has been fixed at a temperature where ZT peaks. Now the temperature at the cold side T_c has been varied for a maximum temperature gradient (max.), a minimum gradient (min.) and a moderate one in between (typ.). The ZT-values are taken from the literature [53–55].

Of course, one has to be cautious when comparing devices made of the five materials in terms of efficiencies. The reason is that the materials will no be competitors in most applications as the temperature ranges for which they are best suited differ considerably. Nevertheless, one finds that the maximum, realistically achievable efficiencies of thermoelectric generators based on PbTe, SiGe, and Bi_2Te_3 are somewhat comparable. Efficiencies of PbTe-based thermoelectric generators are anticipated to be higher than those of Bi_2Te_3-based thermoelectric generators despite the lower ZT_h of PbTe. The value of the power generation efficiency of Bi_2Te_3 is comparatively poor. This is due to the low temperature range in which this material can be employed. So other materials with lower material efficiencies may yield higher values of η due to the higher temperature values T_h and the resulting possibility of realizing higher ΔT. The efficiencies of $FeSi_2$-based thermoelectric generators and hypothetical ZnO-based thermoelectric generators may come

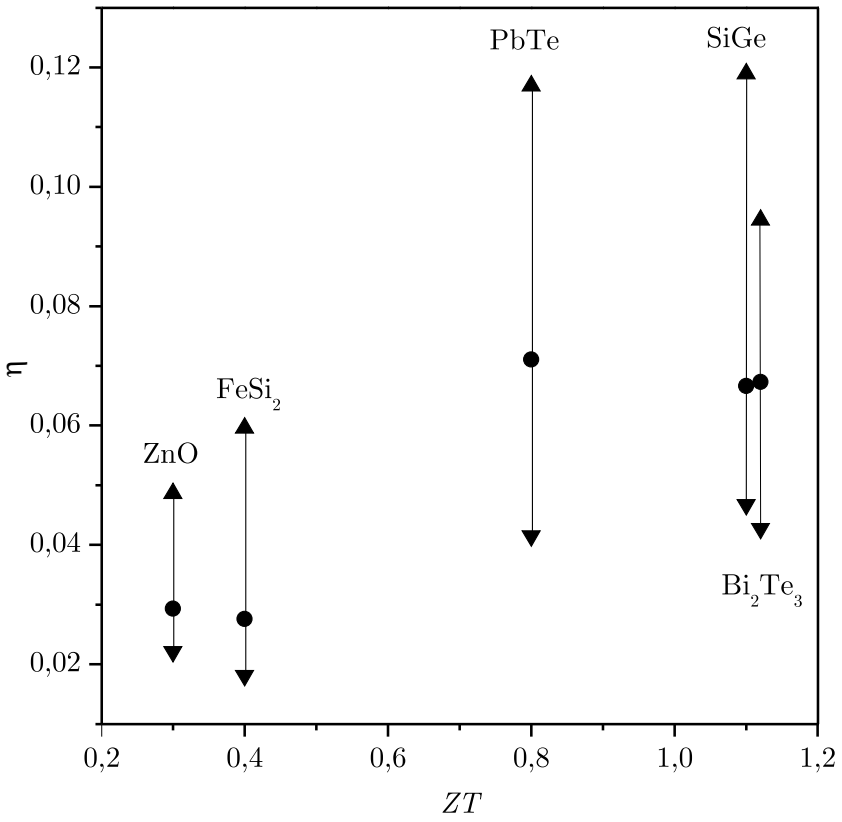

Figure 2.3: Plot of η versus ZT for the five thermoelectric materials (Data from [53–55]). A range of η values is given for each material where the circles represent typical values of ΔT and the triangles limit the range by assuming a minimum and a maximum ΔT. The temperature of the hot end T_h is fixed at the temperature where ZT is maximum.

within a factor of two of those of thermoelectric generators based on the other three materials. Again, the reason is the high temperature-stability of the materials which allows one to apply large temperature gradients. Obviously, for most applications the temperature range of T_c to T_h is given and fixed. This will have an additional impact on the choice of material.

For high-temperature thermoelectric materials it will be essential to maximize the device-ZT over a large temperature range. This is usually done by tuning the material properties to provide a high average ZT over the temperature range of interest. Such a tuning may be achieved in different ways, e.g. by segmenting with different materials that have ZT peaks at different temperatures as in the case of PbTe based materials [53], i.e. functionally graded materials. However, this approach may cause further problems over a large temperature range because the electrical current, required for a high efficiency operation of the device, changes as the material properties vary with temperature and segment. To keep a high performance of the device over the whole temperature range, the so called thermoelectric compability factor ($s = (\sqrt{1+ZT} \pm 1)/ZT$;− for power generation + for cooling) must be similar for all materials used. In order to keep a high efficiency over the temperature range of interest, this term needs to be within about a

Material	$\mathbf{ZT_h}$	$\mathbf{T_h}$ / K	$\mathbf{T_c}$ / K	η / %
Bi_2Te_3	1.1	typ.: 470	320	6.7
		max.: 470	270	9.5
		min.: 470	370	4.3
PbTe	0.8	typ.: 670	400	7.1
		max.: 670	270	11.7
		min.: 670	500	4.2
SiGe	1.1	typ.: 1170	800	6.7
		max.: 1170	570	11.9
		min.: 1170	900	4.7
$FeSi_2$	0.4	typ.: 1120	800	2.8
		max.: 1120	520	6.0
		min.: 1120	900	1.8
ZnO	0.3	typ.: 1270	800	2.9
		max.: 1270	570	4.9
		min.: 1270	900	2.2

Table 2.1: Temperature values taken for the calculation of η of the five materials for a maximum value of ZT at $T = T_h$ and three different values of T_c. Values of ZT are taken from [6, 53–55]. Values for η are derived using equation (2.1).

factor of 2 for all segments [53].

Next to these materials a lot of others are under investigation for a potential industrial production of thermoelectric devices. Very promising material classes are skutterudites, clathrates, half-Heusler-compounds, chalcogenides, and many more. A very nice and detailed overview about the materials of choice, currently of interest, is given by Kanatzidis et al. [6]. Nevertheless these compounds have in common that they are of a very complex structure, which makes it hard to fully analyze them theoretically. This is the reason why, at the moment, the search for the best thermoelectric compound within these material classes follows more or less a trial and error principle.

So far issues like material properties and design efficiencies, availabilty, sustainabilty and cost issues or the parallel use of the materials in other technologies have been discussed. This makes clear, that when designing a thermoelectric generator for a specific application, many aspects need to be taken into account. Some aspects may appear trivial at first sight. However, it is worthwhile going through the entire chain of ideas and setting up a decision matrix as it yields some surprising and rather illuminating conclusions. For a further analysis of this problem, the applications are characterized in terms of mobile vs. stationary and specialized vs. mass application. This basically yields four categories of applications. Fig. 2.4 shows the four categories with a priority ranking for four main criteria. These are high efficiency, costs, environmental friendliness and toxicity, and, finally, availability and sustainability. Depending on the type of application, these criteria have different priorities when it comes to planing and realizing a device. It will be shown in the following that, in particular, the criterion of high efficiency needs further specification.

An extreme example of a ***specialized application mounted in a moving vehicle*** are extraterrestrial space missions. Thermoelectric modules used in such missions need to generate as much power as possible. Furthermore, the mass of the thermoelectric device must be as low as possible as the costs of launching a satellite or other space craft scale

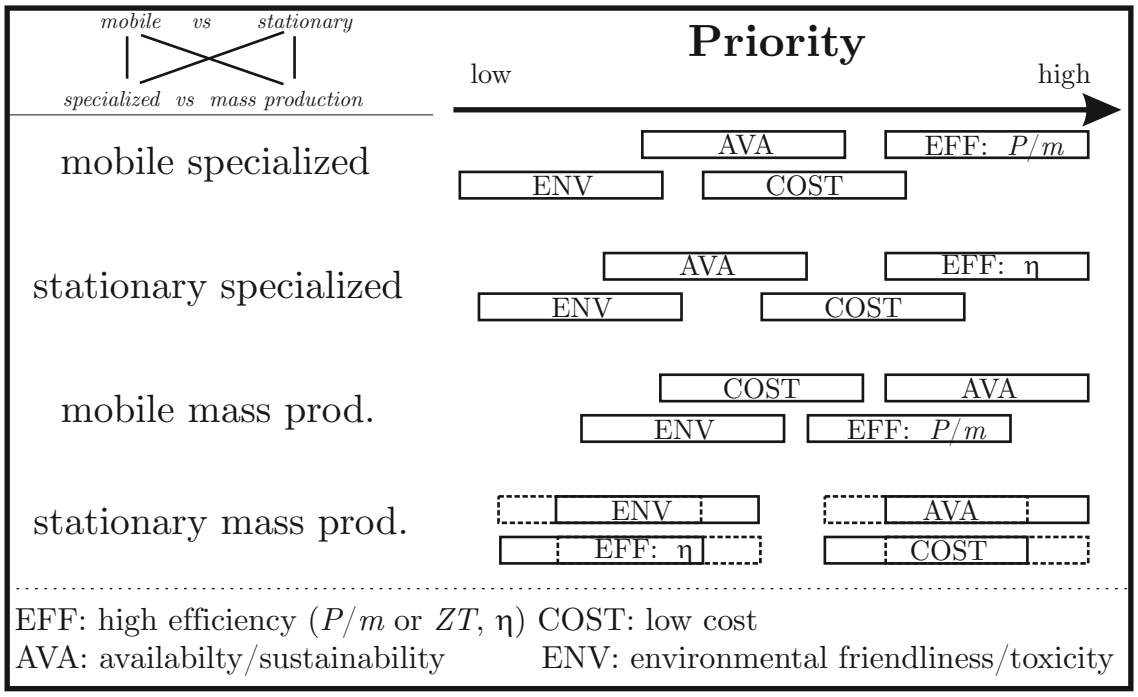

Figure 2.4: Sketch of the different types of applications of thermoelectric generators and the corresponding priority ratings of the selection criteria.

with mass. This means that a high efficiency in terms of watts per gram has the highest priority. A high efficiency includes in this context reliability and a long life time under optimal temperature conditions. Since it is a very specialized application, the production costs usually play a minor role. Availability of the thermoelectric active material and the environmental friendliness have a rather low priority. For extraterrestrial applications, the toxicity of the material has no impact on the environment on earth (problems with the launching excluded). Even for scarce materials, availability plays a minor role since for specialized applications only a very small amount of material is needed compared to mass applications. So the ordering of the priorities is efficiency in terms of power per mass, cost, availability, and, finally, environmental friendliness and toxicity. Of course there might be special applications where the priority ratings change. This is indicated by the overlapping of bars in regions representing the different criteria in figure 2.4.

For ***stationary specialized applications*** the criteria priorities are very similar to those of the mobile specialized ones, but there are some minor differences. High efficiency is again of the highest priority. However, as the thermoelectric generator is stationary the weight issue is of minor importance. So the efficiency has to be high in terms of ZT-values or high values of η given by equation (2.1). Because the stationary generators may become large in dimensions the priorities concerning low cost and materials availability might shift slightly depending on the specific application. Environmental friendliness is a minor criterion in a static application. Of course, it is very important to recycle or to depollute thermoelectric modules properly after completion of their life cycles, but this is done more easily with a stationary device, where the spatial distribution of pollutants is closely limited to the surroundings. Examples for special stationary applications may be the recycling of waste heat in power plants where the design of each thermoelectric

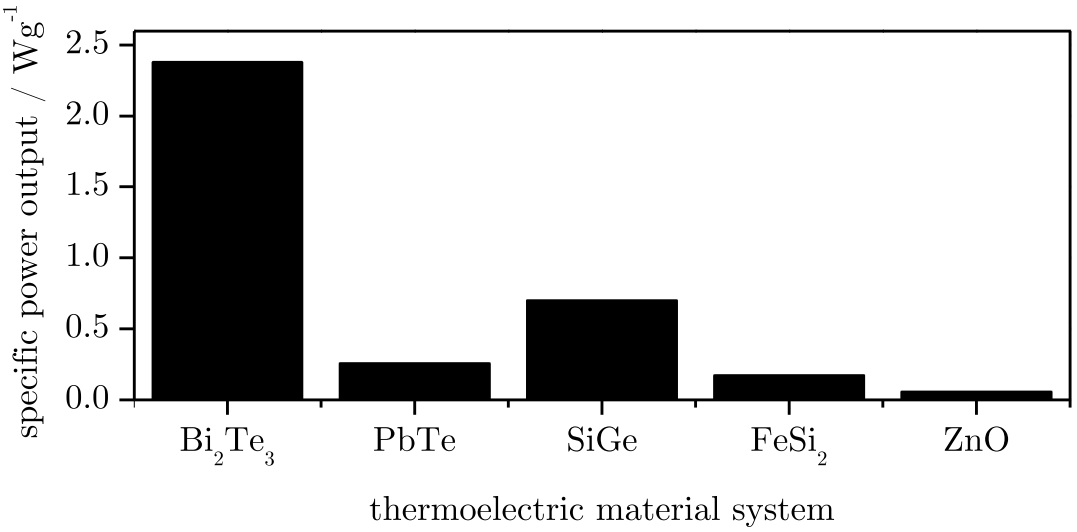

Figure 2.5: Specific power output for different thermoelectric material systems.

generator depends on the special local conditions. The priority ordering is very similar to the previous case, i.e. efficiency in terms of highest efficiency, costs, availability and environmental issues.

An example for a ***mobile mass production*** are thermoelectric generators in cars. The essential criteria for this mass production surely is the availabilty of the used materials. For Bi_2Te_3 generators for example, the tellurium resources would be entirely consumed by only 15 to 32 million cars, even assuming a reduced Te input per kW generation by an increase in efficiency [56]. In other words, the actual Te resources are sufficient to equip a quarter to half of the world car production in 2009 [57]. This is still no realistic estimate because it is assumed that all the tellurium reserves are instantly available. However, the production per year is very low (about 200 t in 2009 [58, 59]), so that the demand of the market cannot be fulfilled. For modules designed for mobile mass applications another important aspect is weight. Since the thermoelectric generator increases the total mass of the vehicle it needs to be as light as possible. So almost as important as the availability is the specific output power in watts per gram. This quantity is shown in figure 2.5 for the materials of interest. Of course, in this context not only the thermoelectric material itself, but the entire thermoelectric generator module needs to be optimized. Thus, figure 2.5 can serve as a rough indication of the problem only.

From an environmental point of view, the use of toxic elements in mass-produced thermoelectric generators should be avoided. Mass products, either stationary or mobile, always imply a distribution of the toxic materials in the environment at the end of the product's life cycle due to improper disposal. A toxic element in this sense is Pb. This is one of the reasons why research into alternatives to PbTe as a thermoelectric material for applications in the automotive sector is strongly pursued. For such mobile mass products, the following ordering of the priorities is found: availability, efficiency in terms of power per mass, cost and environmental aspects.

Criteria / Module	EFF			AVA	COST	ENV
	ZT	η	P/m			
Bi_2Te_3	+	-	+	-	-	-
PbTe	+	+	-	-	-	-
SiGe	+	+	+	-	-	+
$FeSi_2$	-	-	-	+	+	+
ZnO	-	-	-	+	+	+

Figure 2.6: Decision matrix for criteria that need to be considered when realizing a thermoelectric generator. The criteria are efficiency (EFF) in terms of high ZT-value, high power-generation efficiency (η) and high specific output power (P/m), availability (AVA), costs (COST) and environmental friendliness (ENV).

The situation for ***stationary mass products*** is very similar to mobile mass products. Again, if there is not enough material to satisfy the demand, no mass production is possible. Thus, the highest priority should have the availability followed by low costs. The ordering of the criteria as in all the other cases somewhat depends on the type of device. For example, in the case of micro-structured devices, the amount of thermoelectric material needed for a module is very low, but the production costs are fairly high. The low-cost issue might become more important than the availability issue. Another example, are large stationary thermoelectric generators where a higher output can be simply realized by using more material assuming that there is enough space available. In this case, the toxicity issue may become more important than the absolute efficiency η of the material. In other applications, e.g. in some autarkic sensor applications or in woodstoves where the space or the size of the thermoelectric generator device is limited, the priorities of these criteria again might change.

It is obvious from the discussion above that many different materials issues need to be considered when it comes to designing and realizing a thermoelectric device for a specific application. These criteria are summarized in a compact decision matrix in figure 2.6. The five thermoelectric materials are evaluated with respect to the criteria discussed using '+' and '-' to indicate fulfilling and not fulfilling a criterion, respectively. The decision matrix should not be considered a complete manual for designing a thermoelectric generator, in particular, as user requirements and system requirements are not discussed. However, it should offer some guidance in the decision process for choosing the appropriate material system for a specific thermoelectric application.

In summary, the main field of application of thermoelectric devices is energy harvesting from waste heat originating in the energy conversion processes of fossil fuels. Thus, thermoelectrics enhances the efficiency of these processes and potentially may contribute as a clean or green technology to the solution of the world's energy problem in the future, at least, as long as energy demand is satisfied by a mixture of CO_2 neutral and fossil energy sources. Green alternatives are the combined use with solar cells or geothermal approaches [60]. The possible applications of thermoelectric devices range from highly

specialized devices to mass products. The decision process of finding the best technological solution will strongly depend on the specific application. The selection of the suitable material for a thermoelectric device depends on a range of criteria, apart from the specified operational conditions. These criteria include efficiency, availability of the material, price, environmental aspects etc. In principle, production of thermoelectric generators on the terawatt scale is possible based on state-of-the art device performance and materials resources. However, it turns out that this is not necessarily possible with materials of the highest ZT. Thus, in particular, when considering mass products compromising between high efficiency and abundance of the materials required will be unavoidable.

3 Characterization methods

In the investigation of thermoelectric materials surely one of the most important quantities to measure is the Seebeck coefficient. In addition knowledge about the electrical and thermal conductivity completes the set of measurements for determining the figure of merit. For a correct interpretation of the global results across a microstructured sample, one needs local, spatially resolved measurements of these quantities, too. Further methods like Raman spectroscopy or various other microscopy techniques complete the set of measurements and give hint about structural issues. In the following the most frequently used characterization methods during this work are presented and the underlying measurement principles are shortly described.

3.1 Setup for measurements of the macroscopic Seebeck coefficient

For thermoelectric measurements it is very important to adjust temperatures very precisely and to keep them stable during the actual data recording, because temperature fluctuations cause fluctuations of the thermovoltage and hence uncertainties in the determination of the Seebeck coefficient. The experimental setup built for this purpose (see figure 3.1) has been designed to achieve temperature differences as fast as possible whilst at the same time keeping the average temperature constant. The basic idea to realize this, is a constant cooling of the sample holder while simultaneously counterheating it. Liquid nitrogen serves as a coolant down to temperatures of about 100 K. With liquid helium even sample temperatures of about 50 K can be reached. The coolant flux can be adjusted by a flow controller. For the precise temperature adjustment three ohmic heaters can be controlled independently. One controls the average temperature of the sample and the two additional heaters cause and control the temperature gradient across the sample by heating the sample's left and right end, respectively. For this the heaters are mounted onto copper blocks which can be individually moved to account for different sample sizes, but still are in good contact with the basic copper platform (compare inset of figure 3.1).

The entire sample holder is mounted upside down into a vacuum chamber which is evacuated during the measurements down to about $5{\cdot}10^{-5}$ mbar, to guarantee a good thermal shielding. The temperature at the contact points is determined via type E thermocouples (consisting of NiCr and CuNi) which are produced by knoting the respective wires together, which have a diameter of about 80 µm, each. The knots are then soldered into In contacts (points 1 and 2 in figure 3.2). Since thermoelements are not suitable for determining absolute temperatures, but temperature differences only, a reference junction is necessary, where the temperature is kept constant during the entire measurement. This, however, is difficult to achieve experimentally with the accuracy required and over the long period of time (several hours) for a complete measurement. Therefore, a different ansatz is used. The temperature of the reference junctions are held at a semi-constant but precisely known value. The junctions were embedded into a solid copper block whose

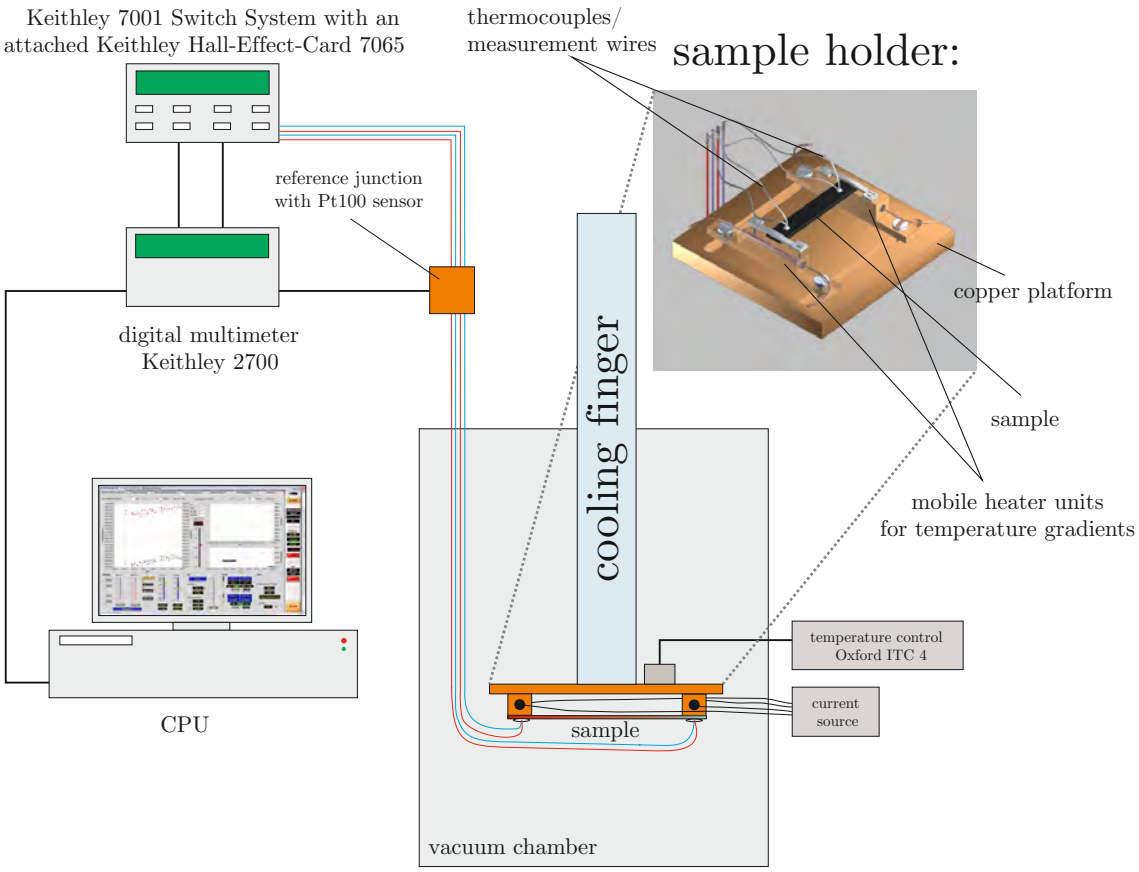

Figure 3.1: Scheme of the experimental setup for thermoelectric measurements with an inset of a 3D-plot of the sample holder.

cavity was filled with an electrically insulating but heat conducting paste. This arrangement was placed into a thermally insulating dewar. Due to the large heat capacity of the copper block and the insulation layer, this offers protection against sudden changes of the reference temperature. However, gradual changes are constantly determined with great accuracy in equal time intervals during the whole thermopower measurement. This is done by using a calibrated Pt100 temperature sensor that had been embedded in the copper block close to the reference junctions and that allows the measurement of the reference temperature with an accuracy of 0.01 K. This time dependent reference temperature is taken into account in the calculation of T_1 and T_2. With this technique the reference junction is not held at a constant value as usually done but is measured with great accuracy during the whole thermopower measurement.

The switching between the several measurement configurations is done using a Switch System (Keithley 7001) with an attached matrix card (Keithley Hall-Effect Card 7065) which provides an excellent state of the art signal-to-noise ratio. The voltages are determined using a Keithley Voltmeter 2700 with integrated multiplexer card that allows for measurements of additional parameters, as e.g. the heating power. All devices are controlled by a specially developed LabVIEW-based measurement software. The controlling can be done manually, for very special demands, or an automated measurement mode can be chosen. In the “auto” mode the measurement is completely contolled by the CPU, but

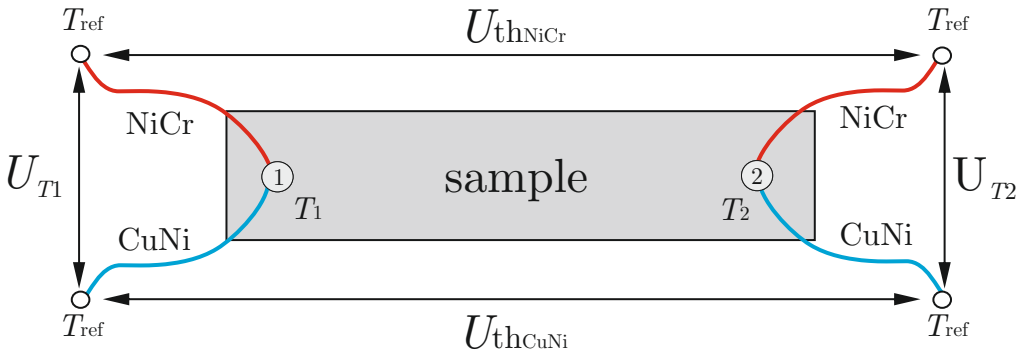

Figure 3.2: Top view on a sample with soldered thermocouples.

each point is measured in the same, from the user adjusted, way. If no special demands are made on the measurement, this mode is very time saving, e.g. measurements over night can be performed.

The measurements of the macroscopic Seebeck coefficient presented in this work are based directly on the Seebeck effect, namely that a temperature difference ΔT along a material causes a thermovoltage U_{th}, that is directly proportional to ΔT:

$$U_{\mathrm{th}} = S \cdot \Delta T. \tag{3.1}$$

The constant of proportionality is the Seebeck coefficient S. To cause a constant temperature gradient, the sample is mounted on two copper blocks as described above. At the points 1 and 2 the type E thermocouples are used (see figure 3.2) to determine the temperatures T_1 and T_2 and the thermovoltages along the sample. The voltages U_{T_1} and U_{T_2}, that fall between the two wires of a thermocouple, are used to determine the temperatures T_1 and T_2. These thermovoltages are proportional to the temperature gradient between the reference point and the temperatures T_1 and T_2 at the sample's ends. Since the used thermocouples are standardized, tables are available [61], which allow a direct translation into a temperature difference. Together with the reference temperature, one can extract the absolute values of the temperatures T_1 and T_2 from the measurement of the thermovoltages U_{T_1} and U_{T_2}.

Along the channel of one type of wire, here exemplarily NiCr, all contributions to the themovoltage $U_{\mathrm{th_{NiCr}}}$ (according to equation (3.1)) can be written as:

$$U_{\mathrm{th_{NiCr}}} = S_{\mathrm{NiCr}}(T_{\mathrm{ref}} - T_1) + S_{\mathrm{sample}}(T_1 - T_2) + S_{\mathrm{NiCr}}(T_2 - T_{\mathrm{ref}}). \tag{3.2}$$

With a few simple transformations one obtains:

$$S_{\mathrm{sample}} = S_{\mathrm{measured}} + S_{\mathrm{NiCr}}. \tag{3.3}$$

The calculataion for $U_{\mathrm{th_{CuNi}}}$ is done analogously.

It is obvious that the measured Seebeck coefficient includes a part that comes from the wires of the thermocouples and one part from the sample itself. So in the following the correction of the ***contribution of the respective wire material to the measured Seebeck coefficient*** will be discussed. To illustrate how important a careful analysis of the wire contribution is, figure 3.3 shows exemplarily the measured thermovoltage of a sample for different temperature gradients. Although the sample is n-type, it can happen

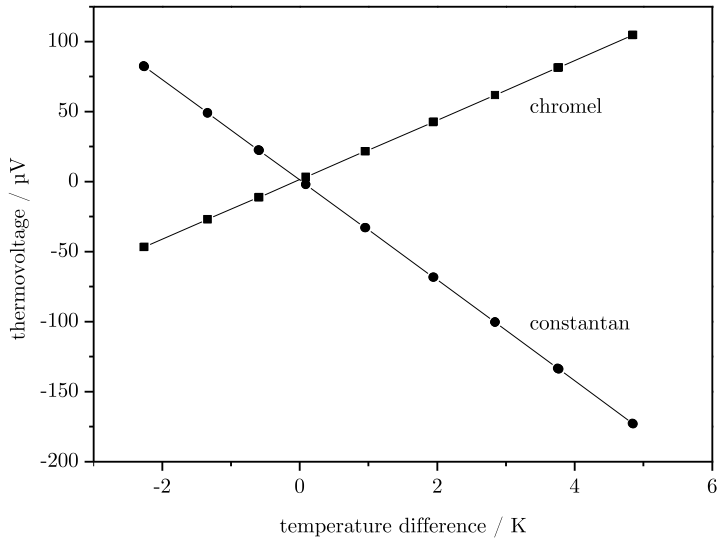

Figure 3.3: Linear relation between thermovoltage and temperature difference at a constant average temperature of 260 K of an Al-doped n-type ZnO sample. The measurements are performed along a constantan (CuNi) and a chromel (NiCr) path, respectively. Before correction the two different slopes (corresponding to two different Seebeck coefficents) can be clearly distinguished.

that, without the correction, one channel has negative Seebeck coefficients (circles) and the other one positive ones (squares).

For the materials used here (NiCr and CuNi) only a few data points, concerning the Seebeck coefficient in the temperature range from 50 - 100 K, are available in the literature. One can circumvent this problem by exploiting the relation

$$S_{\mathrm{CuNi}} = S_{\mathrm{Cu}} - S_{\mathrm{Cu/CuNi}}. \tag{3.4}$$

Here S_{Cu} denotes the absolute Seebeck coefficient of copper, whereas $S_{\mathrm{Cu/CuNi}}$ is the Seebeck coefficient of a standardized type T thermocouple consisting of a Cu/CuNi junction. For this type, standard data after ITS-90 can be taken from [61] in a wide temperature range. The data for S_{Cu} were extraced from Josef Nyström's work [62] and graphically from [63] and were approximated by a polynomial least squares fit. Knowing the Seebeck coefficient of CuNi, one can use this information and the relation

$$S_{\mathrm{NiCr/CuNi}} = S_{\mathrm{NiCr}} - S_{\mathrm{CuNi}} \tag{3.5}$$

to determine the Seebeck coefficient of the second wire material NiCr. Being the Seebeck coefficient of a standard type E thermocouple, data about the unknown $S_{\mathrm{NiCr/CuNi}}$ from equation (3.5) again can be taken from [61]. Now an analytical expression for both S_{NiCr} and S_{CuNi} can be found by polynomial functions using least-squares fits:

$$S_{\mathrm{CuNi}}(T) = \sum_{i=0}^{5} a_i (T/\mathrm{K} - 273.15)^i \frac{\mu\mathrm{V}}{\mathrm{K}} \tag{3.6}$$

with:

$$\begin{aligned} a_0 &= -37.01801 \\ a_1 &= -0.08233 \\ a_2 &= +1.18051 \cdot 10^{-4} \\ a_3 &= -1.55014 \cdot 10^{-7} \\ a_4 &= +2.11826 \cdot 10^{-9} \\ a_5 &= +9.03261 \cdot 10^{-12} \end{aligned}$$

and

$$S_{\mathrm{NiCr}}(T) = \sum_{i=0}^{5} b_i (T/\mathrm{K} - 273.15)^i \frac{\mu\mathrm{V}}{\mathrm{K}} \tag{3.7}$$

with:

$$\begin{aligned} b_0 &= +21.42199 \\ b_1 &= -0.02468 \\ b_2 &= -7.51875 \cdot 10^{-5} \\ b_3 &= +2.4623 \cdot 10^{-7} \\ b_4 &= +1.32233 \cdot 10^{-9} \\ b_5 &= +9.03261 \cdot 10^{-12}. \end{aligned}$$

It should be mentioned that S_{sample} includes a contribution from the substrate as well. This contribution, however, is negligible for semi-insulating substrates, since the following relation holds [64]:

$$S_{\mathrm{sample}} = \frac{\sigma_{\mathrm{substrate}}}{\sigma_{\mathrm{substrate}} + \sigma_{\mathrm{layer}}} S_{\mathrm{substrate}} + \frac{\sigma_{\mathrm{layer}}}{\sigma_{\mathrm{substrate}} + \sigma_{\mathrm{layer}}} S_{\mathrm{layer}}. \tag{3.8}$$

Here $S_{\mathrm{substrate}}$, $\sigma_{\mathrm{substrate}}$ and S_{layer}, σ_{layer} denote the Seebeck coefficient and electrical conductivity of the substrate and the layer, respectively. This guarantees that the overall Seebeck voltage is completely determined by the sample's layer, though it may be orders of magnitude thinner than its substrate, and one can write the following approximation $S_{\mathrm{sample}} \approx S_{\mathrm{layer}}$.

3.2 Setup for local measurements of the Seebeck coefficient

The local Seebeck coefficient measurements have been performed at the *Institut für Werkstoff-Forschung, DLR* in Cologne. With the so called ***Scanning Seebeck Microprobe*** it is possible to measure the local Seebeck coefficient with a spatial resolution down to 10 µm, depending on the thermal conductivity of the sample [65]. In this fashion it is possible to map the thermopower of the sample surface, to obtain information about its state of inhomogeneity, the distribution of its components or the diffusion of one component into another.

The principle setup is shown in figure 3.4 and is based on a heated probe tip that is positioned on the sample surface. With a type T thermocouple (Cu/CuNi), that is connected to the probe, temperature T_1 can be measured. At some distance from the tip

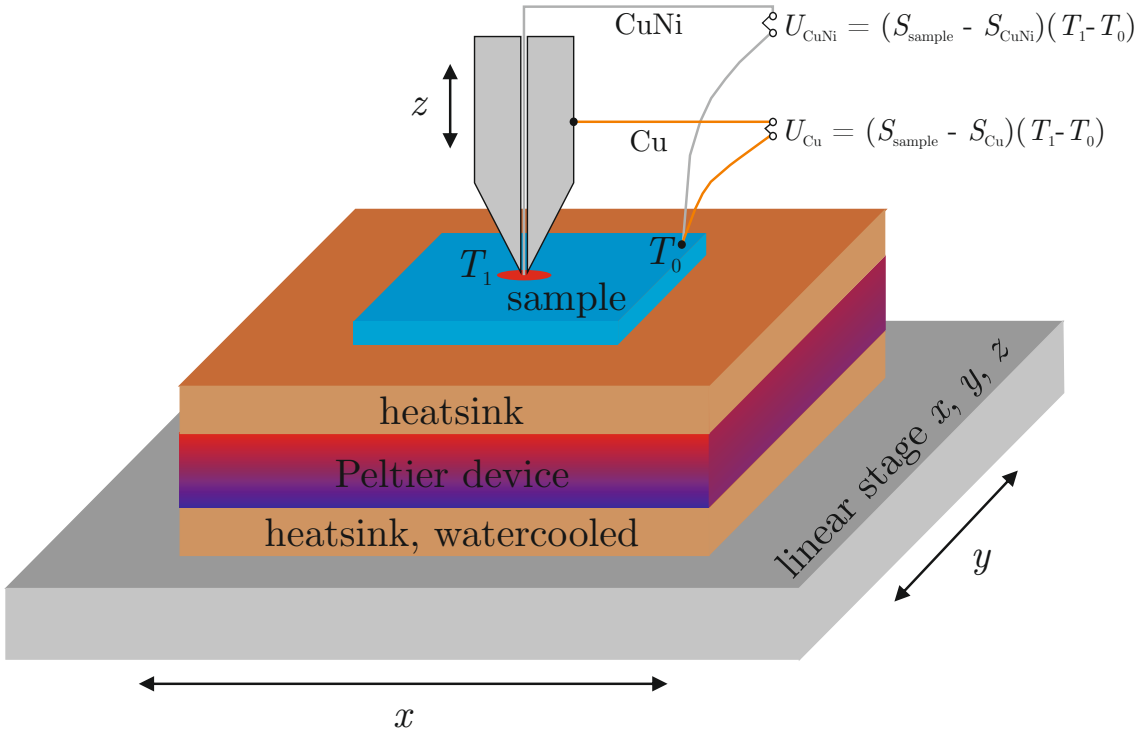

Figure 3.4: Scheme of the experimental setup for local thermoelectric measurements with the Scanning Seebeck microprobe (after [65]).

the temperature of the sample T_0 is determined with another thermocouple. In addition the sample is in good contact with a heatsink to guarantee a good dissipation of the heat introduced by the tip. With the two thermocouples not just the temperatures but also the two thermovoltages U_{Cu} and U_{CuNi} between the two Cu wires and the two CuNi wires of each thermocouple can be measured, respectively:

$$U_{Cu} = (S_{sample} - S_{Cu}) \cdot (T_1 - T_0) \tag{3.9}$$

and

$$U_{CuNi} = (S_{sample} - S_{CuNi}) \cdot (T_1 - T_0). \tag{3.10}$$

Eliminating the temperature gradient, the two equations (3.9) and (3.10) can be combined to

$$S_{sample} = \frac{U_{Cu}}{U_{CuNi} - U_{Cu}}(S_{Cu} - S_{CuNi}) + S_{Cu}. \tag{3.11}$$

In this way the Seebeck coefficient of the sample S_{sample} at the position of the tip can be determined by knowing the Seebeck coefficients of copper and constantan and by measuring the thermovoltages U_{Cu} and U_{CuNi}. If now the sample is mounted on a three-dimensional micro-positioning system a Seebeck-mapping of a certain area of the sample surface becomes possible. The accuracy of each data point depends on the measurement time. To achieve a high accuracy each point is measured about 4-5 seconds. So for one average temperature the scanning takes a couple of hours. Due to a Peltier heating/cooling device, it is possible to choose any average sample temperature between -15 and 60 °C.

Because it is very crucial for the measurements to reproducibly adjust the temperature difference between probe and sample within a few Kelvin, further Peltier elements are integrated into the probe setup. In this way the gradient can be controlled by controlling the temperature of both probe and sample separately but simultaneously over the whole temperature range. To further protect the sample and the probe from ambient influences the recipient is evacuated.

3.3 Setup for measurements of the macroscopic electrical conductivity

For the measurement of transport quantities like the electrical conductivity σ the carrier concentration n or the carrier mobility μ an Oxford Instruments magnet system was used. The schematic setup of this system is shown in figure 3.5. The sample is mounted on a sample holder which is then positioned inside the cryostat, consisting of a helium reservoir and a sample chamber. A superconducting coil, which is cooled with liquid helium, surrounds the sample chamber and generates a magnetic field up to 10 T. A needle valve connects the sample chamber with the helium reservoir. In this way the sample can be cooled down to 1.5 K. A controlable heater (with an *Oxford ITC 4*) is placed under the sample chamber, to adjust the temperature in the sample space in the range from 1.5 K to 290 K. Because the sample is not in direct contact with the heater, the actual sample temperature is monitored by an accurately calibrated temperature sensor which is placed on the sample holder close to the sample. This is done by measuring the resistance of the sensor with a multimeter *Keithley DMM 2000* and then converting it into a temperature by using the corresponding calibration data. The current running through the superconducting coils is provided by a magnet power source (*Oxford PS 120-10*).

To prevent leackage currents and to guarantee a high signal to noise ratio Keithley triaxial cables are used in the so-called guarded circuit technique [66] for the measurements. The *Keithley Hall-Effect Card 7065* with excellent signal-to-noise properties is used as a switching unit. The current for the measurements is provided by a stabilized DC current source (*Keithley 220*). For measuring the current and the voltage the picoammeter *Keithley 6485* and the nanovoltmeter *Keithley 2182* are used, respectively.

All devices can be controlled and monitored by a specially designed software written in LabVIEW. The program allows an extensive automation of the whole measurement procedure, which, especially in the case of magnetic field dependent measurements, is very useful. Here the duration of one standard field-dependent measurement is about 3 hours. Over the whole measurement the temperature needs to be controlled very precisely, since the van der Pauw geometry [67, 68] makes it necessary to average between ρ, $R_\mathrm{H}(-B)$ and ρ, $R_\mathrm{H}(+B)$. Because the magnetic field is usually varied from $-B$ to $+B$, some of these values are measured with a time difference of several hours. Even over such a long time the software is able to achieve a precise control of the measurement temperature with fluctuations of only ± 0.1 K, even at low temperatures.

3.4 Setup for local measurements of the electrical conductivity

The idea for the atomic force microscopy already came up in 1928 by *Synge* [69]. Four years later he extended his idea to the piezo-electric microscopy [70]. However, the technical implementation could only be realized in 1982 by *Binnig* with the first scanning tunneling

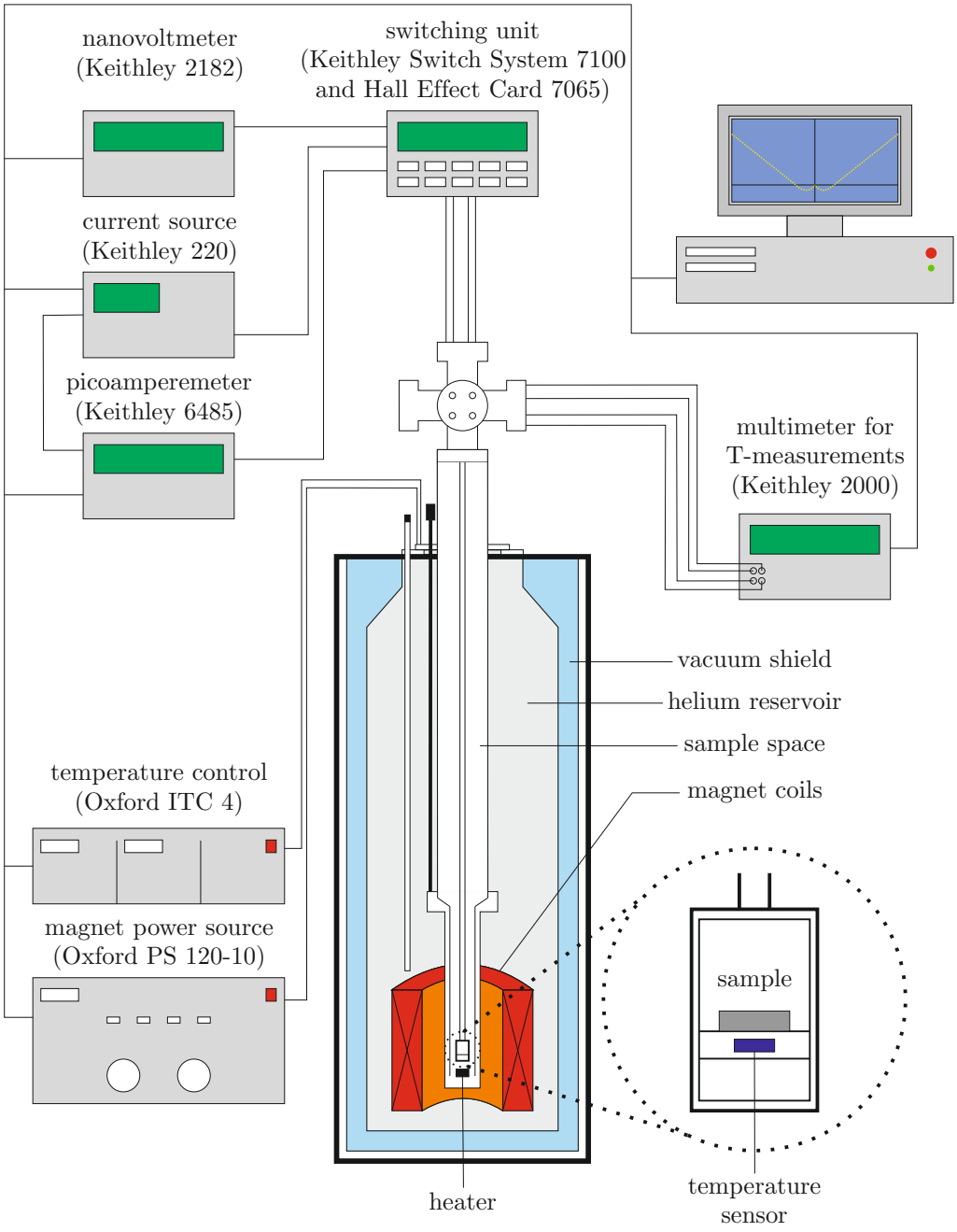

Figure 3.5: Scheme of the experimental setup for magnetotransport measurements.

microscope (STM) [71, 72]. He also was the first person to realize a scanning probe microscope for non electrically conducting samples - the so called atomic force microscope (AFM) [73]. All different types of scanning probe microscopes have in common that next to the information in-plane additional height information is gained. This mapping of the surface roughness is a major advantage of the AFM over the scanning electron microscope (SEM).

The functional principle of all scanning probe microscopes is basically the same: Precondition is a very sharp tip (at the peak ideally only one atom wide) that needs to be

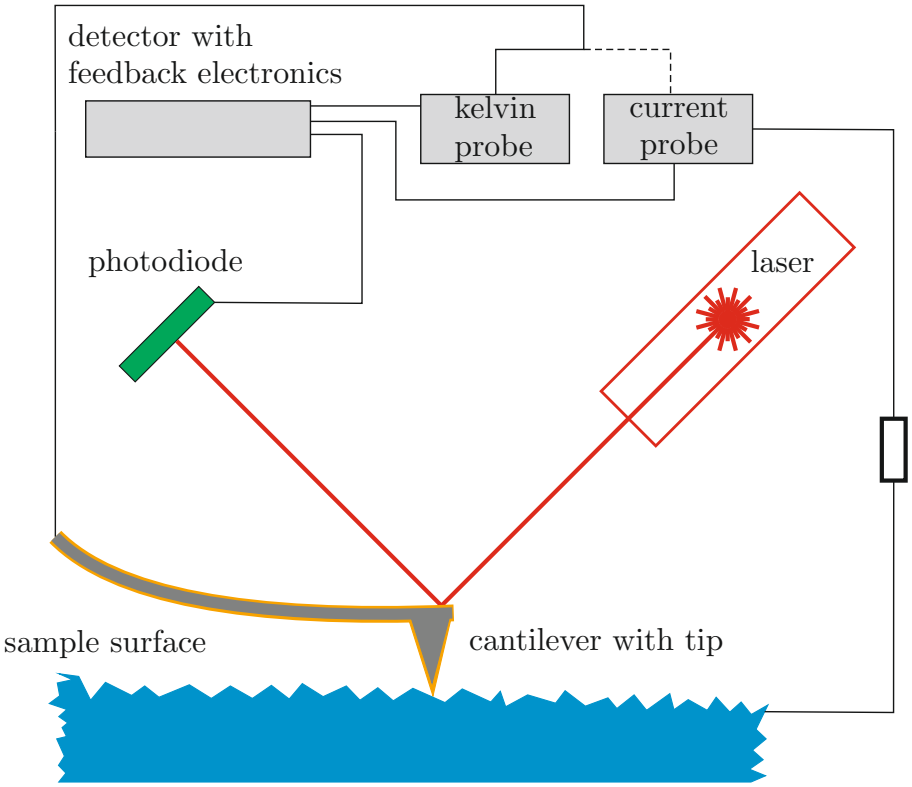

Figure 3.6: Scheme of the measurement principle of atomic force microscopy. In addition to a standard AFM image, this microscope has the possiblity of sensing either the Kelvin force (KFM) or the current force (CS-AFM).

positioned very close to the sample surface. For the AFM usually this tip is at the end of a cantilever that consists typically of silicon or silicon nitride. At a certain distance from the surface forces between the tip and the surface bend the cantilever. This deflection can be measured using a laser beam that is reflected from the top of the cantilever into an array of photodiodes, as shown in figure 3.6. The AFM can be run in many different operating modes. For imaging applications one can distinguish between contact mode, non-contact mode and tapping mode: In the **contact mode** the tip is in direct contact with the sample surface. Here strong repulsive forces between the atom's shells and the tip are acting. In the so called *constant height mode* the tip scans over the surface remaining at a constant height. The roughness of the surface determines the deflection of the tip which is used as a feedback of the topography. Since no adjustments of the tip perpendicular to the sample surface are carried out, very high scan rates can be achieved in this mode. On the other hand it is only applicable for very plane and hard surfaces. In the *constant force mode* the deflection of the cantilever and hence the force between tip and surface is kept at a constant level. A feedback control system assures a steady deflection of the cantilever which makes this imaging mode about two to three times slower than the constant height mode. The advantage here is that the strain of the sample surface is reduced whilst a still very high resolution of the topography can be realized.

The name of the **non-contact mode** already implies that in this mode the tip does not contact the surface of the sample. Here neither the tip nor the sample surface suffer

from degradation. This makes it preferable for imaging soft samples. In a special resonant circuit the cantilever is forced to oscillate with its resonant frequency. If now a force acts between the tip of the cantilever and the sample surface the resonant frequency of the oscillator circuit changes. The shift in frequency serves as a measure for the interacting forces and is used as a control signal for the scanning. This dynamic frequency modulation mode can be used with very stiff cantilevers since shifts in frequency can be measured very sensitively. With this AFM technique atomic resolution under ultra-high vacuum conditions was achieved for the first time [74]. The imaging of different types of materials becomes possible using changes in phase or amplitude of the oscillation as a feedback signal. This amplitude modulation is another dynamic mode that can reach atomic resolution imaging under ultra-high vacuum conditions.

Another dynamic imaging mode is the **tapping mode**. Here the cantilever is forced to oscillate with a frequency near its resonance. This is done with a small piezoelectric element that is mounted in the AFM tip holder. The amplitude of this oscillation is typically 100 to 200 nm (about ten times larger than in the non-contact mode). When the tip comes close enough to the surface, interaction forces start to decrease the amplitude of this oscillation. The height of the cantilever is now controlled in a way, that the cantilever oscillation amplitude remains constant while scanning the surface. The image is produced by measuring the force of the intermittent contacts of the tip with the sample surface. The tapping mode was developed to combine the advantages of measuring samples in a quasi non-contact mode but under ambient conditions. Furthermore this mode can as well be used under liquid medium.

Next to these imaging modes the here used AFM from the company AIST-NT is able to measure two other quantities: In the so called **Kelvin force microscopy** (KFM) mode a conventional tip is coated with a thin layer (20 to 30 nm) of platinum or gold to make it electrically conducting. Now it is possible to gain information about the electrostatic characteristics of the surface and hence to make assumptions about the electron affinity as a function of the topography.

The same kind of tip is used to perform the **current sensing atomic force microscopy** (CS-AFM) also. As indicated in figure 3.6, an additional expansion add-on allows one to apply a voltage between the sample and the tip. The resulting current can then be measured simultaneously with the topography. To prevent the thin gold layer from melting only small currents below 100 nA are allowed. This is guaranteed by a series resistance in the MΩ to GΩ range, depending on the conductivity of the sample. Of course this probing needs to be carried out in the contact mode.

3.5 Setup for local measurements of the thermal conductivity

The measurements of the local thermal condcuctivity have been performed by *Nanonics* in Israel with the scanning probe thermal microscopy (SThM) method. In the following the principal mode of operation is described. Further information, especially concerning the theoretical modeling and computer simulation, can be found in [75–77].

The probe used is based on the platinum/10% rhodium resistance probe developed by Dinwiddie et al. [78]. It can be used as a highly localized and accurately positioned heat source as well as a detector. This probe, commercially available from the TopoMetrix Corporation, enables thermal microscopy using a resistive thermal element incorporated at the end of a cantilever that enables AFM feedback. The arms of the cantilever are

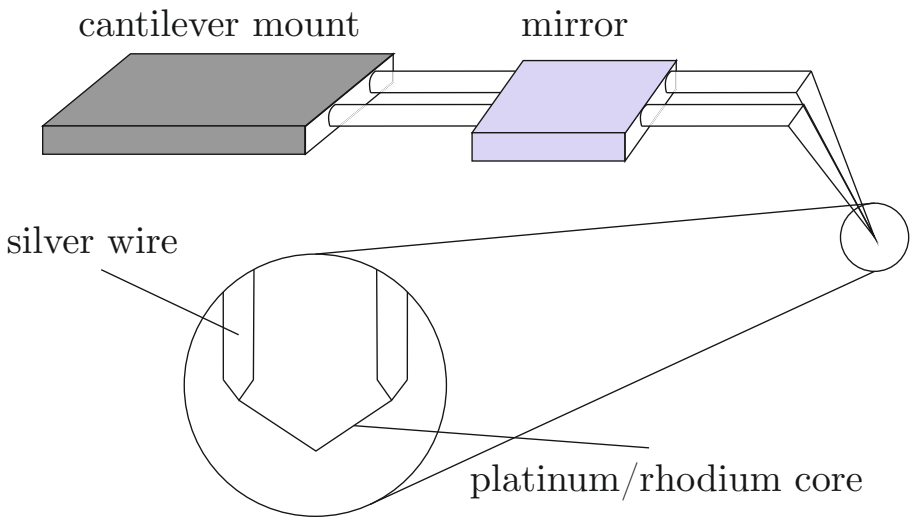

Figure 3.7: Scheme of the resistive probe (after [77]).

made of Wollaston process wire, consisting of 75 µm diameter silver wire containing a platinum/10% rhodium core about 5 µm in diameter. Where the loop is formed, the silver is etched away and the platinum wire is revealed over a length of about 150 µm. The probe, schematically depicted in figure 3.7, is usually attached to a scanning force microscope. A mirror is cemented to the cantilever arms to reflect a laser beam onto a photodiode, so that the cantilever deflection may be sensed.

In addition to the force feedback, the thermal probe can be used with temperature feedback ("active" operation), or without ("passive", i.e. open loop operation). Accordingly there are two principal ways of obtaining a thermal image:

- *constant temperature mode*, requiring temperature feedback, with self-heating;
- *constant current mode*, in which a small current is passed through the probe which then acts as a thermometer.

With active self-heating (*constant temperature mode*), the thermal element is used as a resistive heater, where the probe then forms one of the legs of a Wheatstone bridge. The Wheatstone circuit uses a feedback loop to adjust the bridge voltage as necessary to keep the bridge balanced, thus keeping the temperature of the probe constant. As the probe contacts the sample surface, heat flows from the probe to the sample. Without a feedback, this heat flow will reduce the probe temperature, decreasing its resistance and causing a shift in the bridge balance. The feedback now senses this shift and increases the voltage applied to the bridge. This in turn increases the resistive heating of the probe, returning its resistance to the set point. The contrast in the thermal image is created by monitoring variations of the bridge voltage due to variations of the heat flow out of the probe while it is scanned at constant force. The flow of heat is affected by several factors including the contact area of the probe, the temperature difference between probe and sample, and the local thermal conductivity of the sample.

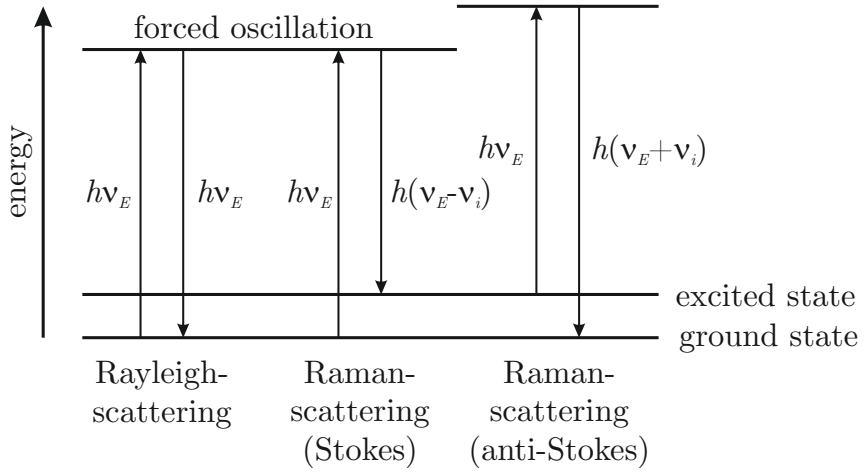

Figure 3.8: Schematic plot of the energy states for light scattering. ν_E denotes the frequency of the incident light, ν_i is the frequency of the lattice (phonon). In the case of resonant-Raman-scattering the enforced oscillations have to be replaced by an excited electronic state.

3.6 Setup for Raman microscopy measurements

If light impinges onto a material, a small part of it is scattered towards all directions sidewards to the incident light beam, even if the material is transparent. This can be explained by an enforced vibration of the electrons caused by the light. The electrons lose the so absorbed energy by emitting radiation in all spatial directions. The biggest part of this scattered light has the same frequency as the impinging irradiation. This elastic scattering process is the so called Rayleigh-scattering. It can also happen, although with a much smaller probability, that inelastic scattering occurs and a part of the absorbed energy is used to excite lattice vibrations (phonons). The remaining scattered light now has a lower frequency than the incident one. This is the so called Raman-Stokes-scattering.

If excited phonons already are available in a material, they can lose energy by transferring a part of it to the incoming light. Then of course the scattered light has a higher energy (frequency) than the irradiated one. Because these spectral lines do not follow Stokes' rules they are known as anti-Stokes-Raman-scattering:

$$h\nu' = h\nu_E \quad \text{Rayleigh-scattering} \tag{3.12}$$

$$h\nu' = h(\nu_E - \nu_i) \quad \text{Raman-Stokes-scattering} \tag{3.13}$$

$$h\nu' = h(\nu_E + \nu_i) \quad \text{Raman-anti-Stokes-scattering.} \tag{3.14}$$

Here ν_E is the frequency of the incident light, ν' the frequency of the scattered light, ν_i the phonon frequency and h Planck's quantum of action. Figure 3.8 gives a comprehensive overview of the three types of scattering mechanisms and their energy transitions.

The polarizability α is a parameter describing the ability to polarize a material. Together with the field intensity E of an external electrical field it determines the induced electric dipole moment μ:

$$\mu = \alpha \cdot E. \tag{3.15}$$

It is oscillating in an external field following the relation [79]

$$\begin{aligned} \mu &= \alpha_0 E_0 \cos 2\pi\nu_E t + \frac{E_0 Q_i}{2}\frac{\partial\alpha}{\partial q_i}\left[\cos 2\pi(\nu_E - \nu_i)t + \cos 2\pi(\nu_E + \nu_i)t\right], \quad (3.16) \\ \alpha_0 &= \text{polarizability in the position of equilibrium} \\ \nu_E &= \text{frequency of the exciting light} \\ \nu_i &= \text{phonon frequency} \\ q_i &= \text{normal coordinate that changes according to: } q_i = Q_i \cos 2\pi\nu_i t \end{aligned}$$

consisting of three superposed frequencies ν_E, $\nu_E - \nu_i$ and $\nu_E + \nu_i$, corresponding to the Rayleigh-scattering and both types of Raman-scattering. Equation (3.16) shows that the intensity of the Raman-scattering depends on the fraction $\frac{\partial\alpha}{\partial q_i}$. That means Raman-scattering only occurs if this ratio is non-zero, or, in other words, if the polarizability changes periodically during the lattice oscillation. Those oscillations that do not fulfil this condition are Raman-inactive.

The assumptions made above hold for transparent materials only where absorption is not taken into account. In this case most of the incident light passes through the material while only a small fraction is scattered, most of it due to Rayleigh-scattering. If now the material absorbs light it consumes a lot more energy because electrons are excited into higher energy levels. The energy transitions are the same as shown in figure 3.8, but with the big difference that now the absorption of a photon with the energy $h\nu_E$ is not used to enforce an oscillation of a virtual state but to lift the electrons into an excited real state. The spectrum of the emitted light is the same as a usual Raman-spectrum, but because the process of energy-absorption and -emission is due to electron-excitation, different selection rules may be valid in the case of the resonant-Raman-spectrum. The theoretical treatment of resonant-Raman-scattering is very complicated and definitely goes beyond the scope of this work. One should mention that the biggest differences to the normal Raman-spectrum is the much higher intensity of the resonant-Raman-spectrum (a few orders of magnitude).

Typically only about $10^{-6}\%$ of the photons are Raman scattered. This is the reason why Chandrasekhara Venkata *Raman* only discovered the effect five years after Adolf *Smekal* predicted it in 1923 [80]. The difference in energy of incident and scattered photon results in a difference in frequency. This can be measured in a so called Raman microscope. Traditionally a Raman-spectrum is given in wavenumbers related to those of the incoming light, i.e. as a difference between the actual wavenumber of the Raman-scattered light and that of the incident light. As a result one automatically obtains the quantity of interest, namely the oscillation frequency of the lattice in wavenumbers. They can be gained as a result from the ratio between the frequency ν and the speed of light c:

$$\tilde{\nu} = \frac{\nu}{c} = \frac{1}{\lambda}. \quad (3.17)$$

Here λ denotes the wavelength. In general the unit of the wavenumber $\tilde{\nu}$ is chosen to be cm^{-1}.

Figure 3.9 shows a schematic plot of the *inVia Raman Microscope* from the company *Renishaw* used here. The shift in frequency (Raman-shift) is measured in wavenumbers relative to the laser-frequency (the wavenumber of the laser is set to zero). To guarantee this for each of the three available lasers (633 nm, 532 nm and 325 nm) special filters are employed that absorb almost the entire incoming light in a range of about $100\,\mathrm{cm}^{-1}$

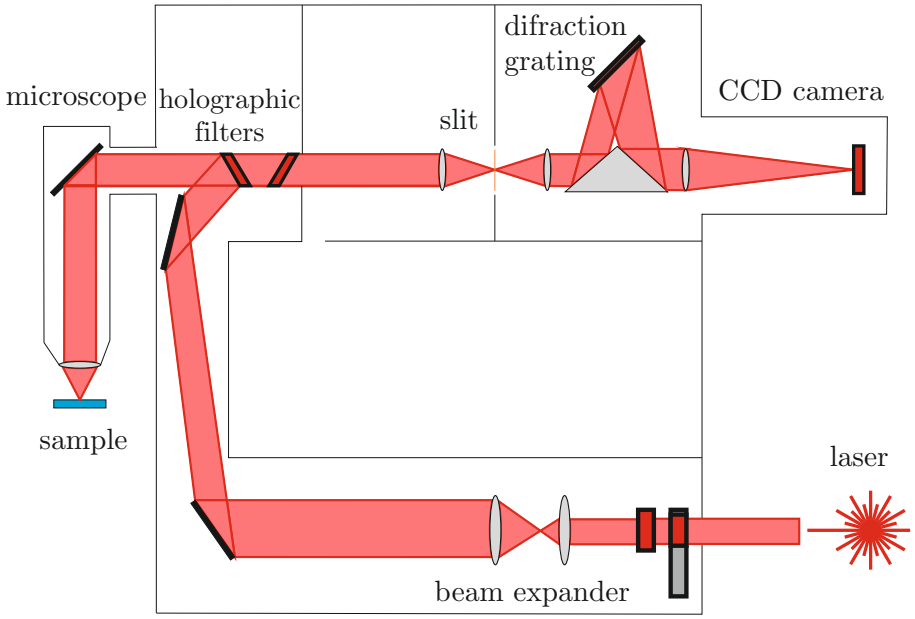

Figure 3.9: Scheme of the experimental setup for raman microscopy measurements (provided by *Renishaw* plc.).

around its frequency. Furthermore, laser specific tilted mirrors, slit calibrations, collimators and diffraction gratings are automatically selected and controlled by the software. With manual settings and the so called NExT filter set however, it is possible to detect a Raman-shift of approximately $10\,\mathrm{cm}^{-1}$. All the filters used transmit Stokes scattered light only, which is of longer wavelength than the laser light. After the diffraction grating the light is focused on a CCD camera for digital analysis. In addition, the system can be also used to acquire photoluminescence spectra. In combination with a x-y-z stage a mapping across the sample surface of the Raman- or PL-intensity can be performed with a very high spatial resolution of about $5\,\mu\mathrm{m}$[1].

[1]The limiting factor of the spatial resolution is the spot size of the laser and not the driving accuracy of the x-y-z stage, which is about 100 nm.

4 Sample preparation

In the following sections, first the sample preparation procedure, namely the self-aligned pattern transfer, will be described. Then it will be shown, how the properties of the interface depend on variation of the process parameters, and which degrees of freedom one has when using this preparation method. Finally, possible variations and extensions of the technique will be pointed out. It should be noted that the process has been tailored to conductive oxide thin films, but is in principle transferable to other thin film materials.

4.1 Self-aligned pattern transfer process

Figure 4.1 shows a somewhat idealized process flow. It starts with the blanket deposition of material A by virtually any thin film deposition method onto a substrate (a). The sample is then coated with photoresist, which is exposed (b) and developed (c). The photoresist masking layer is then used for subtractive patterning of material A, e. g. by wet chemical etching or by ion beam etching (d). Additionally, the photoresist masking serves as a lift-off mask in the subsequent additive patterning of material B, consisting of the two steps of thin film deposition (e) and the final lift-off of superfluous material B by dissolving the photoresist masking (f).

In panels (b) and (c) of figure 4.1, the assumption has been made that a positive photoresist is used, i. e. a photoresist whose exposed portions are removed during development.

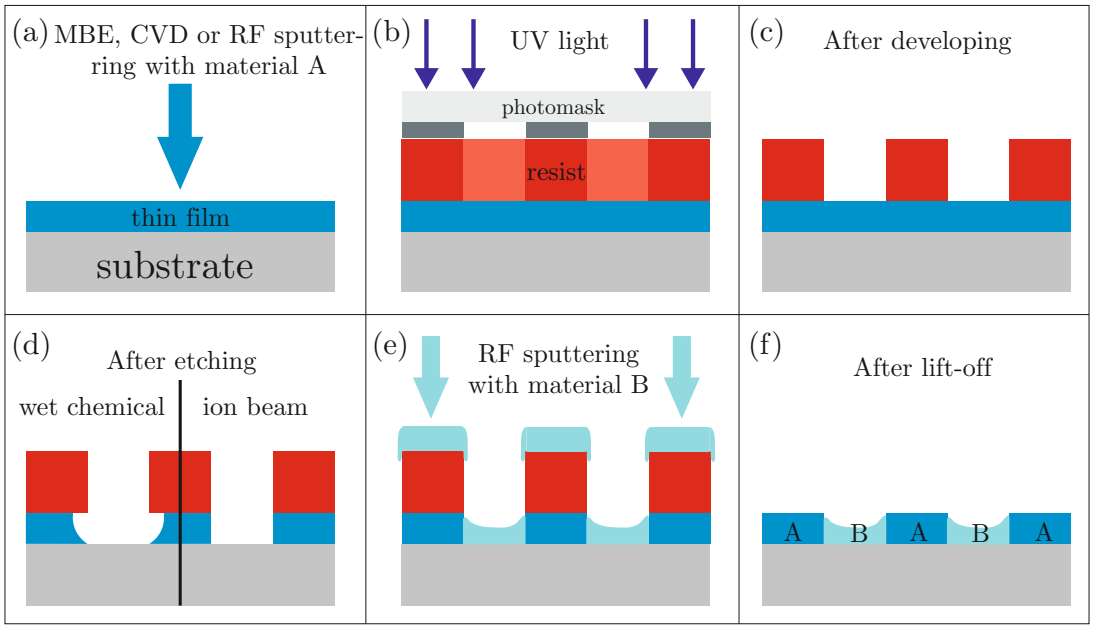

Figure 4.1: Lateral patterning of alternating films of two materials by self-aligned pattern transfer.

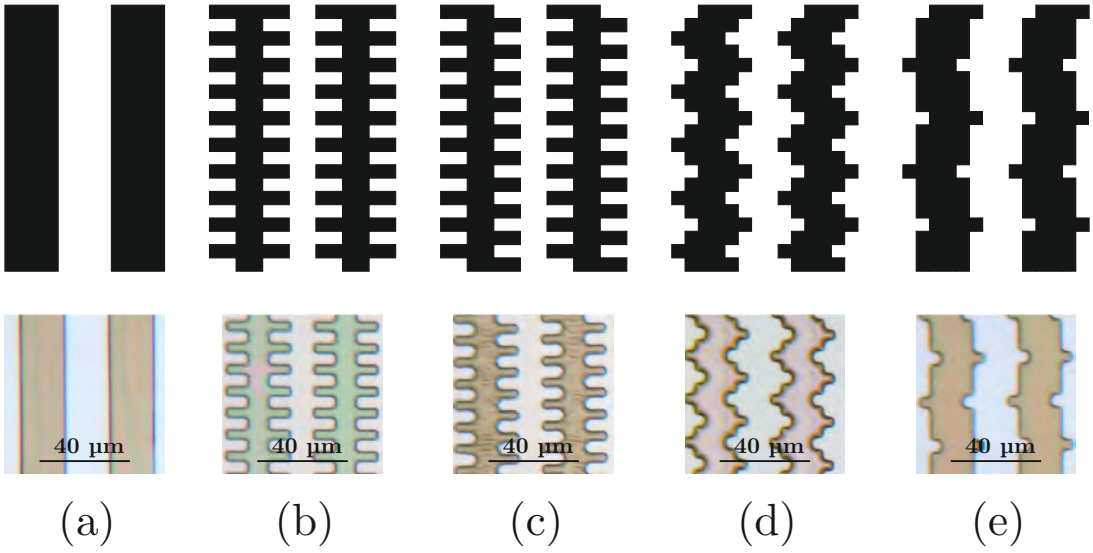

Figure 4.2: Schematic drawing of the five different interface shapes designed for this work: (a) straight interfaces, (b) teeth in-phase, (c) teeth in counter-phase, (d) wavy and (e) toothed interfaces with constant distance. The length of a tooth is typically in the order of 5 µm, the pitch (center-to-center-distance of the conducting bars of the same material) in the order of 40 µm. The lower images are optical micrographs of the pattern transferred into the photoresist after the development step (step (c) of figure 4.1).

As we will see, negative resists can be used as well. In this case, the transparent and opaque structures on the photomask have to be reversed.

The parts of the thin film of material A that are not covered by the patterned photoresist masking are now removed by etching. The etching method may be either wet chemical etching or any of the wide variety of dry etching methods, such as ion beam etching or reactive ion etching. In the selection of the etching method, especially two properties have to be considered. Firstly, the different etching methods differ in their selectivity, that is the ratio of the etching rate of the thin film (that is to be etched) and of the resist masking (which, ideally, should not be etched at all). Secondly, the different etching methods will deliver differing degrees of anisotropy. In the case of wet chemical etching, and assuming that the thin film will be polycrystalline or at best oligocrystalline, etching will be isotropic, i. e., the rate at which the thin film is being removed in horizontal direction will be equal to the etching rate in vertical direction [81]. Ion-beam etching, on the other hand, can deliver a certain degree of anisotropy, resulting in steep sidewalls of the etched film and a low degree of underetching (removal of material covered by the resist masking). The different idealized shapes of the etched thin film are shown in panel (d) of figure 4.1.

The selectivity of the resist masking can be improved by a hardbake procedure, in which the developed sample is heated up to a temperature slightly below the glass point of the resist. Temperature control must be precise, because at a temperature even slightly too high, the resist masking may lose its shape, resulting in a failure of the remaining processing steps.

While the deposition method for material A can be practically any of the multitude of methods available for thin films, including the vast class of chemical vapor deposition

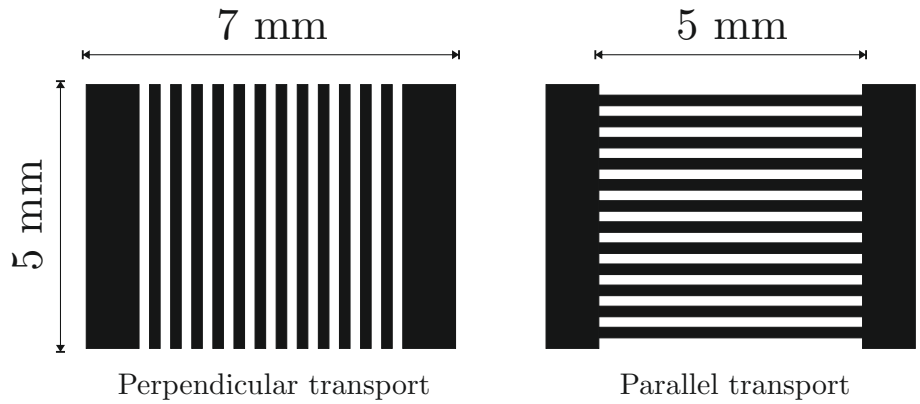

Figure 4.3: Schematic drawing of the positioning and orientation of alternating conductor bar structures between the electrical contact bars (to the left and right, respectively).

(CVD) methods or molecular beam epitaxy (MBE), the deposition method for material B has to be compatible with the resist masking still present at this step in the process flow (panel (e) of figure 4.1). Namely, the temperature at the sample surface has to remain below the glass point temperature of the photoresist, which usually means a maximum temperature in the range between 120 °C and about 200 °C, depending on the precise type of resist used. This excludes all CVD and MBE methods and leaves only physical vapor deposition methods (PVD) available. These may be evaporation coating, pulsed laser deposition, or a variety of sputter coating methods. In the experimental work presented here, material B was always deposited by sputter coating. The advantages of sputter coating compared to evaporation coating are that the resulting films will have a higher degree of crystallinity and that it tends to give a better coverage of sidewalls (conformal coating) than does evaporation coating. This is important since it is usually desirable that the vertical sidewalls of material A are in contact to material B. The coverage of the sidewalls may, however, not be too high, since that would result in a covering of the sidewalls of the resist masking as well, and that would prevent the solvent in the lift-off step (panel (f) of figure 4.1) from reaching and hence dissolving the photoresist. The solvent has to be chosen for good selectivity to the thin film materials and can be either a general purpose solvent as acetone, or, especially in the case of hardbaked photoresist, a special organic solvent known as “remover”.

4.2 Freedom of pattern choice and limitations

The interface shape on a length scale larger than the wavelength of light may be chosen rather arbitrarily. This is demonstrated by the five different interface shapes which were realized and which are shown schematically in figure 4.2. The lower images show optical micrographs of the interface structures transferred into photoresist after the development step. It can be seen that defining these interface shapes on the length scale of a few micrometers can be easily done. Many of the results discussed in the following are based on samples where pattern (d), a wavy interface shape, was used. The alternating bars of the two conductors were designed to cover an area of $5 \times 5\,\mathrm{mm}^2$ between two contact bars each 1 mm wide and extending over the 5 mm perpendicular to the direction of elec-

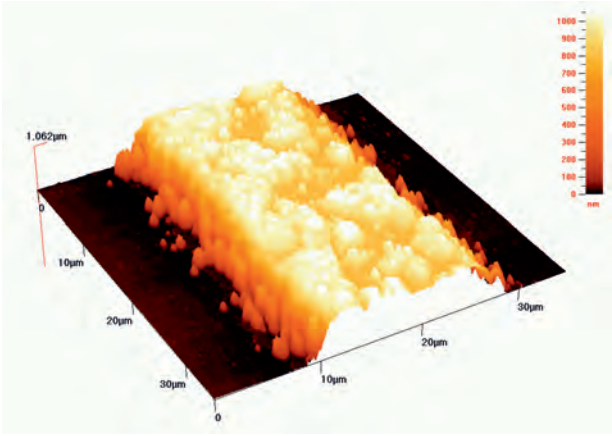

(a) Atomic force micrograph.

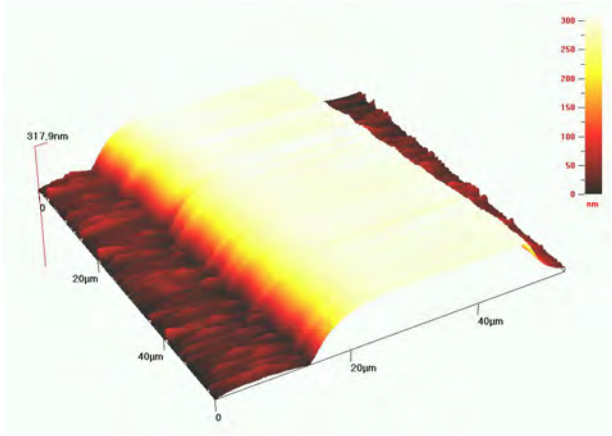

(b) Atomic force micrograph.

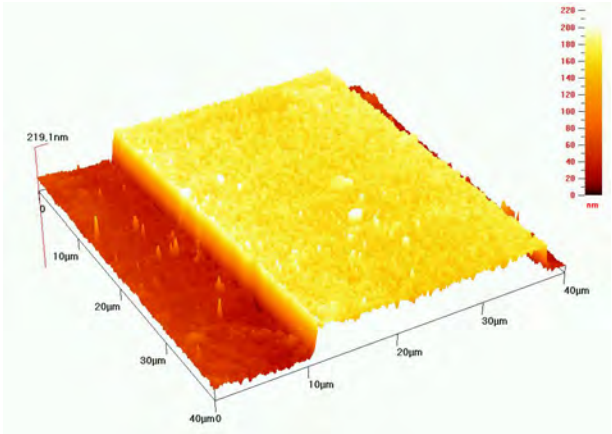

(c) Atomic force micrograph.

Figure 4.4: Atomic force microscopy (AFM) images of etched edges of three ZnO thin films. The images (a) and (b) show a sputtered (a) and an MBE grown (b) film after pattern transfer and wet chemical etching. Image c) shows an AFM image of a sputtered ZnO film after pattern transfer by ion beam etching: The different edge morphologies can be clearly distinguished (images from [82]).

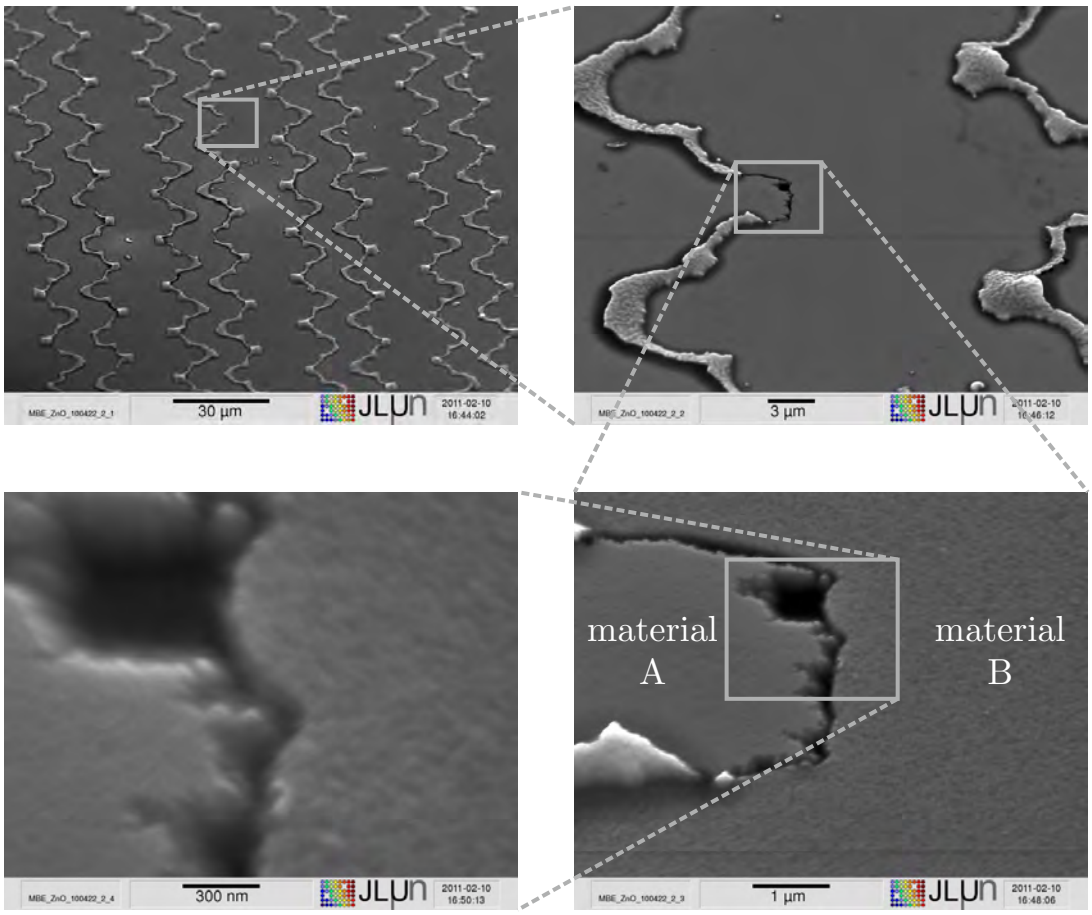

Figure 4.5: Scanning electron micrographs (zoom-in series) of a sample with MBE-grown ZnO (material A) and Ga-doped ZnO (material B), processed using positive photoresist and wet chemical etching. The wavy structures extending over the sample surface are remnants of the sputter coated ZnO layer that had been deposited on the resist sidewalls and hence were not removed in the lift-off step.

trical transport. Two orientations of the interfaces to the direction of current flow were implemented, as shown in figure 4.3.

The pitch of the conducting bars, or, in other words, their packing density are limited (among others) by the thickness of the thin film of material A. Since, as mentioned above, wet chemical etching is in many cases nearly perfectly isotropic, the resulting distance between two conductor bar edges at the end of the process flow has to be at least more than twice the thickness of the thin film. If the structures were too close together, they would either not be separated in the depth of the film (on the surface of the substrate), or they would be damaged at the film surface once etching has been performed long enough to separate the conducting parts. It should be kept in mind that in order to ensure process safety, given a slight uncertainty in actual etching rates, etching always has to be carried out for slightly more than the minimum time required theoretically (so-called "overetching").

The etching rate will, among others, depend on the crystallinity of the material being

etched. This means that the etching rate of material A will depend on whether it has been deposited with a method like MBE, which gives a high degree of crystallinity and usually lower etching rates, or sputter deposition, which leads to polycrystalline material of smaller crystals and a higher etching rate, because etching along the grain boundaries is faster than etching of individual grains. As a second-order effect, the morphology of the etched edge will depend on the deposition method as well. In the case of polycrystalline samples grown predominantly in vertical direction, the conductor edge will be lined with vertical isolated columns, whereas the etched edge of an oligocrystalline film will tend to be rather smooth. Figure 4.4 depicts AFM images of etched edges of three ZnO thin films. The images (a) and (c) are of sputtered ZnO films etched by wet chemical and ion beam etching, respectively. Image (b) shows an AFM image of a MBE grown ZnO film after wet chemical etching: The different edge morphologies can be clearly distinguished. The combination of wet chemical etching and granular sputtered material yields a nanostructured interface region with columns of original material protruding the closed interface. In contrast ion beam etching of sputtered material yields comparatively sharp interfaces with rather steep edges. Wet-chemical etching of epitaxial MBE-grown ZnO shows a closed surface of the edges, but with a smoother slope than for ion beam etching.

For material B, an upper limit of the film thickness is given by a certain fraction of the thickness of material A. If this fraction exceeds a value of around $\frac{3}{4}$, the conformal coating of the resist sidewalls will prevent a succesful lift-off of material B. While the upper limit of the film thickness is governed by the pattern transfer process as described above, the lower limit of the film thickness is given by the requirement that the film has to be continuous. The limit at which a film becomes continuous varies with the deposition method, and in general, higher deposition temperatures require a larger film thickness to pass the threshold to continuity. Evaporation coating can result in continuous films for thicknesses as low as 10 nm [83], while for sputter deposition of conducting oxides, the limit is in the order of 50 nm. In addition, a certain minimal film thickness is desirable since the conductivity, which, in first order, is inversely proportional to the film thickness, should not be too low for transport properties to be reliably measurable.

4.3 Control over the interface properties

In this section different combinations of process parameters, namely of the resist and the etching method used will be discussed, the resulting interface morphologies will be presented and the properties will be correlated to the preparation process in order to demonstrate the range over which the interface properties can be controlled and tuned.

Very often ***interfaces with point-wise contacts*** are obtained. Two examples are shown in figures 4.5 and 4.6 which were obtained using different photoresists and wet chemical etching. In the first case material A consists of a ZnO layer with a thickness of 200 nm, grown by molecular beam epitaxy on top of a 300 µm thick sapphire substrate. Photolithography was first performed with a 1.5 µm thick layer of positive photoresist (ma-P 1215 from micro resist technology, Berlin). Exposure was done with a UV broad-band source in a Suss MA 56 mask aligner at doses of 67.2 mJ cm^{-2} at 365 nm wavelength and 122.4 mJ cm^{-2} at 405 nm wavelength. The resist was developed in ma-D 331 developer (also from micro resist technology, Berlin) for 15 s and hardbaked for 90 minutes in a convection oven. The zinc oxide was wet chemically etched in a mixture of 84 % orthophosphoric acid (H_3PO_4), 100 % acetic acid ($C_2H_4O_2$), and water (H_2O) in a ratio

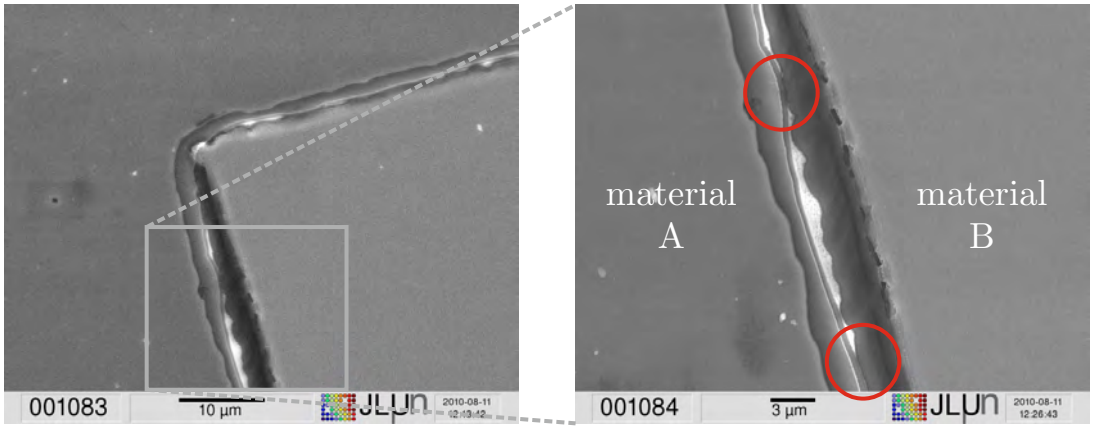

Figure 4.6: Scanning electron micrographs (zoom-in) of a sample with sputter deposited ZnO (material A) and sputter deposited Cu_2O (material B), processed using negative photoresist and wet chemical etching. The point-wise contacts (circled in the right image) had a density of approximately one per 10 µm of interface length.

of 1:1:100 parts by volume [84]. Etch end detection could be performed by monitoring the electrical resistance in situ, since ZnO is intrinsically electrically conducting. As material B, a 150 nm thick layer of Ga-doped ZnO was deposited by radio frequency (RF) sputter coating. This thickness is very close to the limit imposed by the requirement that lift-off still has to be possible. For a successful lift-off, the solvent bath had to be heated to 50 °C, and ultrasonic excitation had to be applied to the bath.

Figure 4.5 shows a series of scanning electron micrographs of a sample processed in the way described. At high magnification, the point-wise nature of the contact along the interface is clearly visible. The remnants of the Ga-doped ZnO due to incomplete lift-off (so-called "garden fences", resulting from material deposited on the resist sidewalls) had no influence on the electrical transport properties.

A point-wise contact along the interface similar to that in figure 4.5 can also be achieved using negative instead of positive photoresist. The substrate in this experiment was glass, and material A was a thin layer of sputter deposited ZnO. The negative resist ma-N 1420 (again from micro resist technology, Berlin) was spincoated to a thickness of approximately 2 µm and exposed using the same UV broadband source mentioned above with doses of 560 mJ cm^{-2} at 365 nm wavelength and 1002 mJ cm^{-2} at 405 nm wavelength. The most important parameter is the development time, since this time determines the width of the undercut profile in the developed resist. A development time of 65 s in the developer ma-D 533S (from the same supplier) resulted in an undercut of approximately 0.6 µm [85]. Again, hardbake has to be subject to tight temperature control in order to preserve the undercut profile. The ZnO was wet chemically etched as in the experiments with positive photoresist detailed above. Copper-I-oxide (Cu_2O) was sputter coated on the surface. The hardbaked negative resist could not be removed with acetone, so the lift-off was carried out using the specially formulated remover mR-rem 660 (from the same supplier) under ultrasonic excitation. The scanning electron microscopic characterization of the resulting interface, cf. figure 4.6, shows the point-wise nature of the contact, with a contact density of about one per 10 µm of interface length. Using extreme undercut profiles allows one

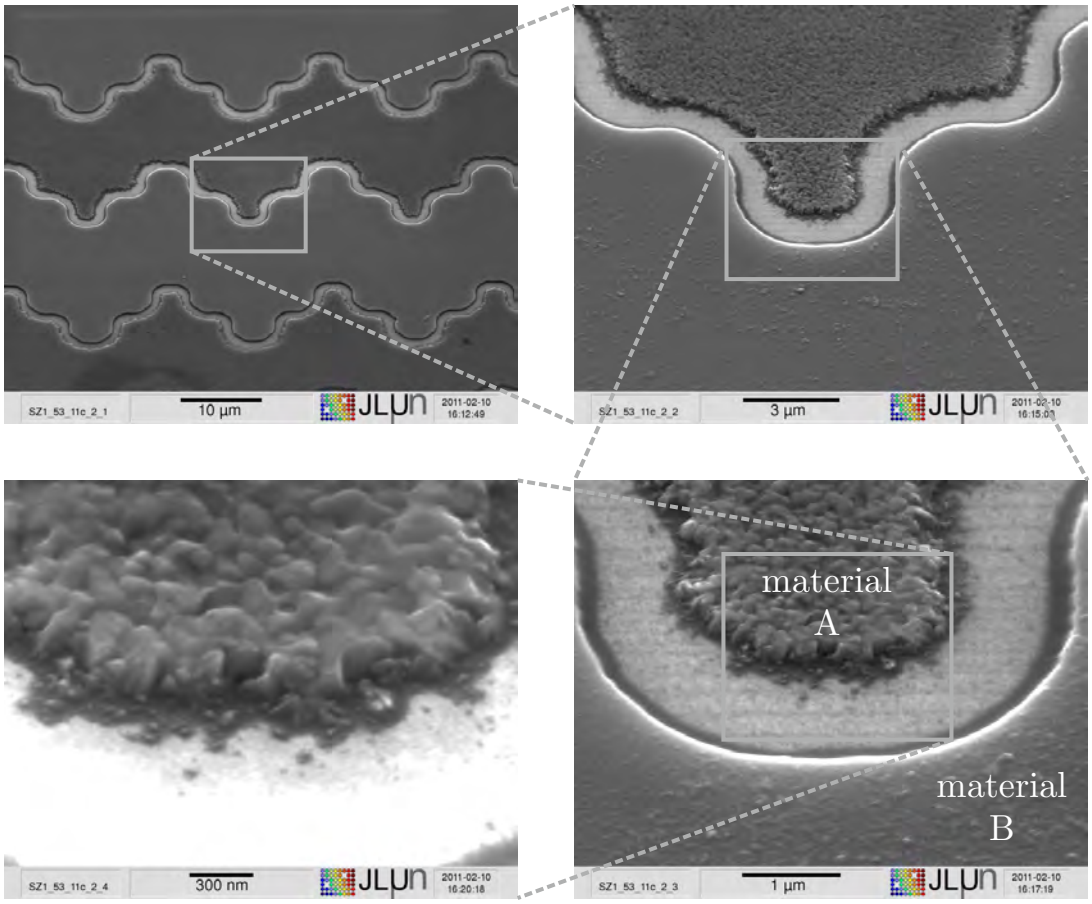

Figure 4.7: Scanning electron micrographs (zoom-in series) of a sample with CVD-grown ZnO (material A) and Ga-doped ZnO (material B), processed using negative photoresist and wet chemical etching. The undercut of the negative resist was tuned to around 2 µm by extending the development time to 120 s, resulting in a well-defined gap along the entire length of the interface.

to separate materials A and B by a gap. Such ***interfaces with a gap*** can be obtained using the same preparation of material A as described in figure 4.6, but extending the development time to 120 s. This creates a rather extreme undercut of approximately 2.1 µm [85]. Exposure doses in this case were 504 mJ cm^{-2} (365 nm) and 918 mJ cm^{-2} (405 nm). Material B again was a 150 nm thick layer of Ga-doped ZnO deposited by RF sputter coating. Lift-off was easily achieved for such a large undercut, and figure 4.7 shows the resulting interface in a series of scanning electron micrographs. The isotropic character of the wet chemical etching process in combination with the undercut profile of the resist sidewalls prevents the creation of interfaces with continuous contact.

Continuous almost ideal interfaces can be obtained by using ion beam etching (IBE) instead of wet chemical etching as the dry etching avoids an undercut profile. In IBE, chemically inert ions (Ar^+ in our case) are accelerated by a voltage of several hundred volts (in our case 700 V in a Kaufman source at a current density of 190 µA cm^{-2}) and directed onto the sample, resulting in a material removal caused by physical effects ("bombardment") with a certain degree of anisotropy. The etching rate of ZnO under

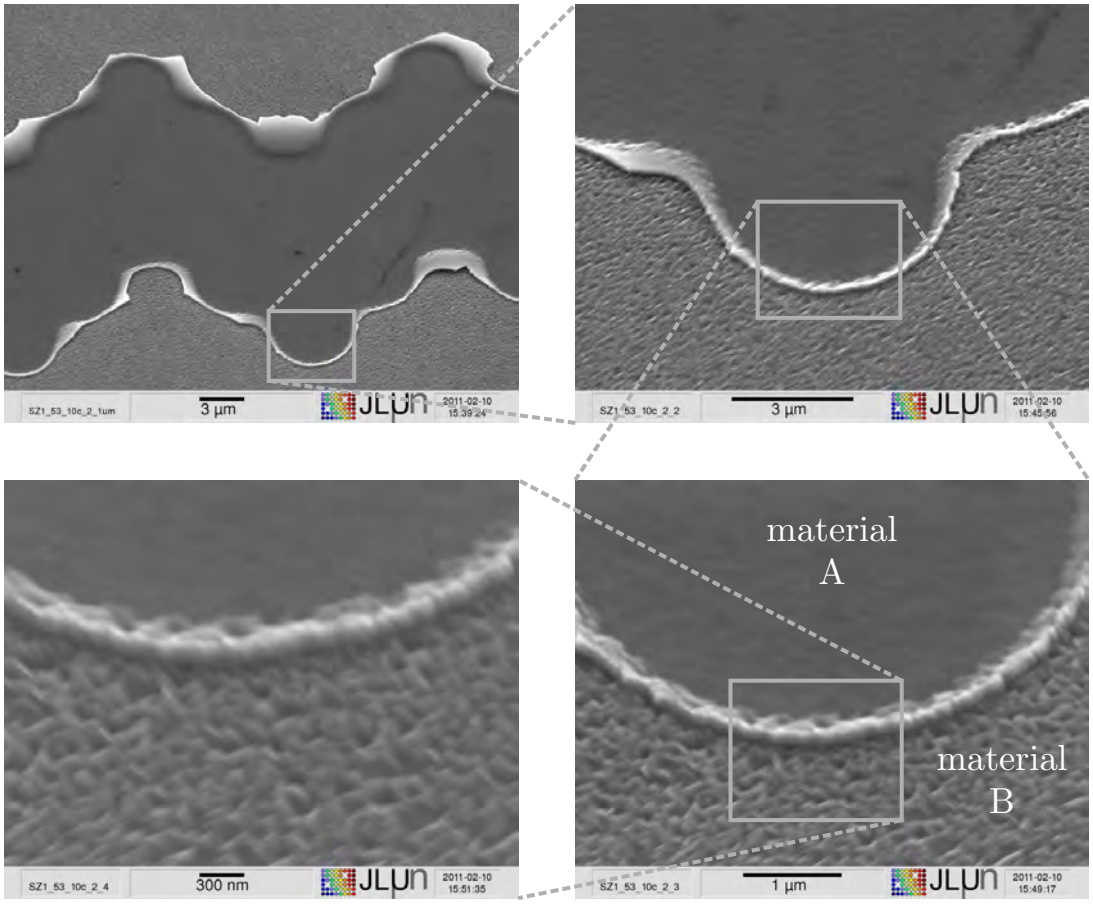

Figure 4.8: Scanning electron micrographs (zoom-in series) of a sample with CVD-grown ZnO (material A) and Ga-doped ZnO (material B), processed using positive photoresist and ion beam etching. Some remnants of material B are visible, indicating imperfect lift-off. The two materials are in electrical contact along the entire length of the interface.

these conditions is approximately $30\,\mathrm{nm\,min^{-1}}$. Alternating etching cycles of no more than 3 minutes and cooling cycles had to be employed to avoid excessive heating of the sample by the ion beam.

The result of a process flow with CVD-grown ZnO (material A), positive photoresist, ion beam etching, and sputter deposited ZnO (material B) is shown in figure 4.8. Positive photoresist was used here since in general it provides less undercut than negative resist, which obviously is advantageous for a continuous interface. Lift-off could be achieved with heated acetone under strong ultrasonic excitation. As can be seen in figure 4.8, the two materials are in contact along the entire interface, i. e., the combination of photoresist processing and thin film etching-method approaches a nearly perfect interface.

In combination with the self-aligned patterning process it is even possible to achieve controlled structure ***definition of interface regions on the sub-micrometer scale***. Here, the possibilities are manifold and one example will be discussed briefly.

For example, this may be achieved by making use of the properties of wet etching in sputter deposited oxide layers. The grain structure of the oxide thin films is columnar

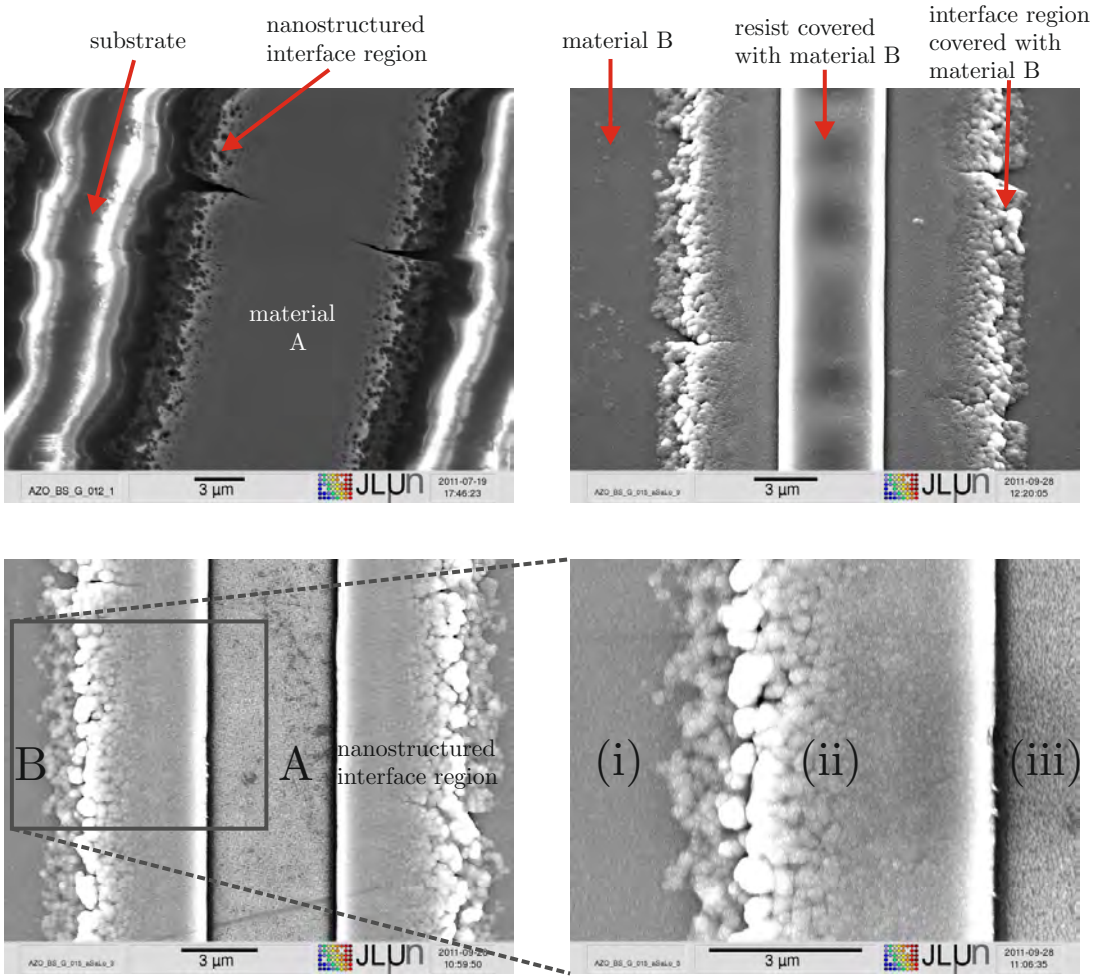

Figure 4.9: Scanning electron micrographs of a wet chemically etched layer of ZnO:Al. The four images show samples after different steps of the processing: After wet chemical etching (upper left), after second lithography and sputter deposition (upper right), after lift-off (lower left), and a magnification of the resulting interface (lower right). The roughness of the edge is predominantly caused by the crystallinity of the material and is on the order of a few tens to about one hundred nanometers.

with characteristic diameters of grain columns in the range of 50 to 100 nm. Wet chemical etching proceeds faster along the grain boundaries than through the nanocrystalline grains, resulting in an irregular array of freestanding nanocrystallites, often columnar in shape, along the edge of the etched thin film, as shown in the SEM image of figure 4.9 (upper left) and the AFM image in figure 4.4 (a). The width of this region is determined by the characteristic radius of the columnar grains and the ratio of the etch rates along the grain boundaries and through the bulk of the grains. The region can be created in a single photolithography step. If the interfaces of a sputter deposited thin film of material A are nanostructured this way, then using the structured film as a starting point of a second lithography step followed by the self-aligned deposition of material B, allows one to embed the nanostructures of material A in the interface region between A and B,

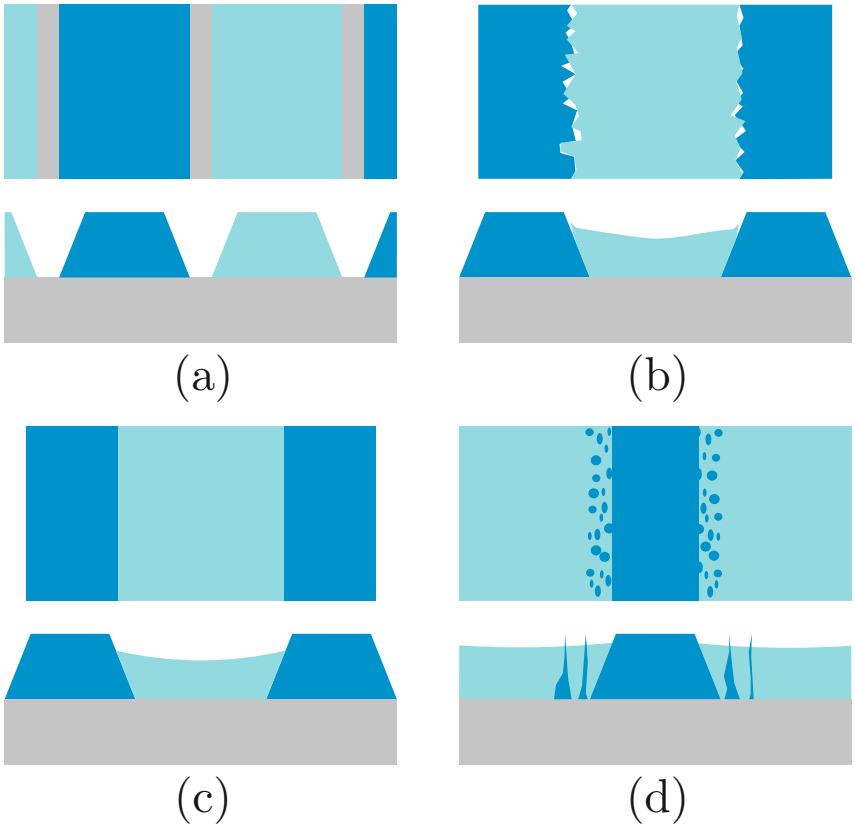

Figure 4.10: Interface morphologies realized by photolithography and self-aligned additive pattern transfer by sputtering: Insulating gap along the length of the interface (a), point-wise contacts along the length of the interface (b), continuous electrical contact over the entire length of the interface (c), and controlled interface structuring on the nanometer scale (d).

yielding a defined interface region. The other SEM images of figure 4.9 depict different steps of the processing. The magnification of the interface shows three distinct regions: Region (i) is material B coming from the second sputter deposition. Region (ii) is the nanostructured interface, where both materials are on top of each other. In region (iii) material A can be seen. This is the region which was protected by the resist (compare upper right image of figure 4.9) and is now uncovered after the lift-off.

Figure 4.10 summarizes schematically the four types of interface morphologies realized by photolithography and self-aligned additive pattern transfer by sputtering. The self-aligned pattern transfer method has the potential to be integrated into extended and more complex process schemes, to even achieve controlled interface structuring on the nanometer scale. Furthermore it could be shown how a variety of morphologies of the interface between two conducting oxides can be created by a single photolithography process and subsequent self-aligned pattern transfer. The choice of the process parameters allows one to adjust the morphology of the interfaces ranging from almost ideal interfaces via interfaces with point-wise contacts to interfaces with a gap of controlled width, even below the resolution limit of the photolithographic process step. This is one of the characteristic features of self-aligned pattern transfer.

5 Theoretical background

As indicated above in the introduction, the transport results presented here are affected by the sum of many different contributions arising from the microscopic, the mesoscopic, and macroscopic structure, respectively. It is obvious that a single theory is not able to describe all the phenomena completely. Therefore an interplay of different theoretical approaches is required, to peoperly describe the ongoing physics on the different length scales. As will be seen in the following, the transport coefficients of interest, namely the Seebeck coefficient S, the electrical conductivity σ as well as the thermal conductivity κ, are measured for different materials (ZnO, ZnS) which were grown by various methods (MBE, CVD, sputter deposition) and structured with different patterns and on various length scales. At an atomistic level surely ab initio calculations using density functional theory are an adequate tool to start with. At this length scale the transport across an interface, e.g. between two ZnO grains of a sputtered ZnO layer can be considered as coherent in the vicinity of the interface between clusters. Of course, the transport at a mesoscopic length scale, e.g. within such a ZnO grain is to be treated diffusively. For a macroscopic description of the sample the findings on the microscopic level can serve as input parameters for a network model approach.

5.1 Thermoelectric transport parameters within the Boltzmann regime

There are several effects that contribute to the thermal conductivity in a solid i.e. an electronic contribution due to the free carriers and a lattice contribution due to phonons, $\kappa = \kappa_{\mathrm{lat}} + \kappa_{\mathrm{el}}$. Let us consider the phonon contribution first. With increasing temperature T the vibrations of the crystal atoms, i.e. the occupation of the vibrational states with phonons, also increase. If a temperature gradient is applied across the sample, phonons from the hot side cause a transport of heat to the cold side. If the temperature is very low, only acoustic phonons with a long wavelength, i.e. a low energy and k-vectors at the center of the Brillouin-zone, are excited. In this regime the thermal conductivity is proportional to the specific heat C_{V}. Together with the Debye approximation [86] one obtains a T^3 dependence:

$$\kappa_{\mathrm{lat}} \propto C_{\mathrm{V}} = 9Nk_{\mathrm{B}} \left(\frac{T}{\theta_{\mathrm{D}}}\right)^3 f_{\mathrm{D}} \left(\frac{\theta_{\mathrm{D}}}{T}\right). \tag{5.1}$$

N is the number of atoms and k_{B} is the Boltzmann-constant. The function $f_{\mathrm{D}}\left(\frac{\theta_{\mathrm{D}}}{T}\right)$ is defined as:

$$f_{\mathrm{D}} \left(\frac{\theta_{\mathrm{D}}}{T}\right) = \int_0^{\theta_{\mathrm{D}}/T} \frac{x^4 \cdot e^x}{(e^x - 1)^2} dx. \tag{5.2}$$

In real lattices the temperatures where one can find a pure T^3-dependence are often below $T = \theta_{\mathrm{D}}/50$, with θ_{D} as the Debye-temperature [87].

At high temperatures ($T > \theta_D$) phonons at higher frequencies and higher k-vectors $|\vec{k}| \lessapprox \pi/a$ are excited. Here due to phonon-phonon interaction three-phonon processes, the so called Umklapp-processes [88] occur, which reduce the thermal conductivity of the lattice as the phonon resulting in the scatter process has a momentum vector k pointing towards the hot side, i.e. is effectively back scattered. An Umklapp-process occurs if the momenta of two interacting phonons are so large, that the resulting total momentum is outside the first Brillouin-zone. Due to symmetry considerations the momentum reduced by a reciprocal lattice vector of the resulting phonon lies within the first Brillouin-zone and possesses opposite direction than the sum of the momenta of the two interacting phonons. The more Umklapp-processes take place, the more the heat transport is hindered. The collision frequency of a given phonon on the other hand is proportional to the number of phonons, it can collide with. From this it follows that the mean free path of phonons is proportional to $1/T$, which was firstly discovered by Eucken in 1911 [89]. For lower temperatures the number of phonons with high energies $1/2k_B\theta_D$ suitable to cause Umklapp-processes decreases. So, in this regime, the thermal conductivity decreases according to the Boltzmann factor $e^{\frac{\theta_D}{2T}}$.

The second contribution is the heat transport via charge carriers. The Wiedemann-Franz law [4] correlates thermal conductivity and electrical conductivity of the charge carriers

$$\frac{\kappa_{el}}{\sigma} = LT, \tag{5.3}$$

where the Lorenz number L can be generally defined via Fermi-Dirac integrals [90]:

$$L = \left(\frac{k_B}{e}\right)^2 \left(\frac{(r+\frac{7}{2})F_{r+5/2}(\eta)}{(r+\frac{3}{2})F_{r+1/2}(\eta)} - \left[\frac{(r+\frac{5}{2})F_{r+3/2}(\eta)}{(r+\frac{3}{2})F_{r+1/2}(\eta)}\right]^2\right) \tag{5.4}$$

with

$$F_i(\eta) = \int_0^\infty E^i f_0(E) dE. \tag{5.5}$$

Here f_0 is the Fermi-distribution function, η is the reduced Fermi energy and r is the scattering parameter. For many metals and highly degenerate semiconductors the Lorenz number has the value $L = 2.45 \cdot 10^{-8}\,\mathrm{W\Omega K^{-2}}$. In non-degenerately doped semiconductors the thermal conductivity via phonons is much larger than via charge carriers because their number is too low. For metals the situation is reversed. Because of the numerous free charge carriers the thermal conductivity of metals is very high.

For a thermoelectric application a good electrical and a small thermal conductivity is desired. Depending on the considered temperature range, both types of heat transfer have a different fraction of the resulting thermal conductivity. In semiconductors the lattice thermal conductivity κ_{lat} is dominant in the low temperature regime, while with increasing carrier concentration the electrical part of the heat transfer κ_{el} becomes more important.

In the following the derivation of the Seebeck coefficient S, the electrical part of the thermal conductivity κ_{el}, and the specific electrical conductivity σ is briefly described. The theory is well known and the interested reader can find it in more detail in the thermoelectric literature [91, 92].

To determine the thermoelectric transport coefficients, one assumes a perturbation of the charge carrier distribution $f(E)$ through an electric field and a temperature gradient. For simplicity we consider a crystal with a parabolic energy band having only one type of charge carriers of energy E. The charge carrier distribution can then be described with

the Boltzmann equation. The equation assumes an equilibrium between effects caused by the electric field and scattering processes between the charge carriers:

$$\frac{f(E) - f_0(E)}{\tau_e} = -\vec{k}' \frac{\partial f(E)}{\partial \vec{k}} - \vec{r}' \frac{\partial f(E)}{\partial \vec{r}}. \tag{5.6}$$

In equation (5.6) f is the disturbed and f_0 the undisturbed distribution function. τ_e is the relaxation time of the charge carriers between the scattering processes. The relation between the energy dependence of the relaxation time and the scattering coefficient r is $\tau_e = \tau_0 E^r$. $\vec{k}$ and $\vec{r}$ are the wave vector and the position vector of the charge carriers, respectively. Now one can calculate the Boltzmann equation for a temperature gradient and an electric field, assuming an isotropic solid and that the field and the temperature gradient follow one direction. Furthermore the perturbation is considered to be very small:

$$|f - f_0| \ll f_0. \tag{5.7}$$

The result of this calculation serves as an input for the equations of the electric current density j and the heat current density q. The electric current density j is defined as

$$j = \mp \int_0^\infty ev f(E) g(E) dE. \tag{5.8}$$

In the following, if two signs are present, the upper one holds for electrons and the lower one for holes. $g(E)$ is the density of states, e the elementary charge and v the velocity of the charge carriers. The equation for the heat current density q is

$$q = \int_0^\infty v(E - E_\mathrm{F}) f(E) g(E) dE, \tag{5.9}$$

where E_F is the Fermi energy. The expression $E - E_\mathrm{F}$ describes the energy that is tranported by the charge carriers. After the implementation of the Boltzmann equation with perturbation ansatz the resulting expressions for the electric current density and heat current density are indicated with $j = j^*$ and $q = q^*$, respectively.

To get an expression for the specific electrical conductivity one can use the relation

$$\sigma = \mp \frac{j^* \cdot e}{\partial E_\mathrm{F} / \partial x} \tag{5.10}$$

where, in the resulting equation, the temperature gradient is set to zero.
For the calculation of the Seebeck coefficients and the electronic part of the thermal conductivity one can use the expressions

$$S = \frac{\partial E_\mathrm{F} / \partial x}{e(\partial T / \partial x)} \tag{5.11}$$

and

$$\kappa_{el} = -q^* \left(\frac{\partial T}{\partial x} \right). \tag{5.12}$$

The Seebeck coefficient and the thermal conductivity are determined with the restriction that no current is applied. Hence the expression for the electric current density j^* is set to zero.

The most elegant way to describe the three thermoelectric transport coefficients S, σ and κ_{el} is via the so called general transport coefficients K_x. Depending on the value of x the value of K_x changes according to the fomula

$$K_x = \frac{8\pi}{3}\left(\frac{2}{h^2}\right)^{3/2}(m^*)^{1/2}T\tau_0(x+r+3/2)(k_\mathrm{B}T)^{x+r+3/2}F_{x+r+1/2}. \tag{5.13}$$

The Fermi integral is defined as follows:

$$F_n(\xi) = \int_0^\infty \xi^n f_0(\xi)d\xi, \tag{5.14}$$

with $\xi = E/(k_\mathrm{B}T)$ as the reduced energy. m^* is the effective mass of the charge carriers. The thermoelectric transport coefficients can now be expressed via the general coefficients as follows:

$$\sigma = \frac{e^2}{T}K_0, \tag{5.15}$$

$$S = \pm\frac{1}{eT}\left(E_\mathrm{F} - \frac{K_1}{K_0}\right), \tag{5.16}$$

and

$$\kappa_{el} = \frac{1}{T^2}\left(K_2 - \frac{K_1^2}{K_0}\right). \tag{5.17}$$

To determine S for non-degenerate semiconductors, $E_\mathrm{F} \ll k_\mathrm{B}T$ is assumed, i. e. the Fermi energy is far away from the conduction band edge. With the corresponding Fermi integral it is then possible to determine the general transport coefficients and hence the Seebeck coefficient. One obtains

$$S = \pm\frac{k_\mathrm{B}}{e}\left[\eta - \left(r + \frac{5}{2}\right)\right], \tag{5.18}$$

with $\eta = E_\mathrm{F}/(k_\mathrm{B}T)$ being the reduced Fermi energy.

5.2 Transport across an interface

To calculate the transport across interfaces that occur e.g. between grains of sputtered ZnO an effective model is described which was developed by Heiliger et. al. [22, 93]. The input parameters of this model can be obtained by *ab initio* calculations. For the potential profile across a grain boundary a so called back-to-back Schottky barrier is often used in the literature [94]. Basically this model assumes that there are additional electronic interface states in the bandgap available. In the case of n-type ZnO (or any other n-type semiconductor) these states can be filled with electrons from donor levels. As a consequence the space-charge region directly at the interface will be negatively charged, whilst the vicinity on both sides of the interface will be charged positively. The resulting profile of the potential at the grain boundary is shown on top of figure 5.1. As indicated in the figure the structure can be divided into three different regions: The small (yellow) region of the interface has a high negative space-charge, the larger (blue) region has a low positive space-charge, and a large (green) undisturbed region of the grains. The total net charge of the system is zero. Because of the space charges $n(x)$ a potential barrier builds up that can be determined by solving the Poisson equation

$$\nabla(\epsilon_r(x)\nabla V(x)) = \frac{e\cdot n(x)}{\epsilon_0}. \tag{5.19}$$

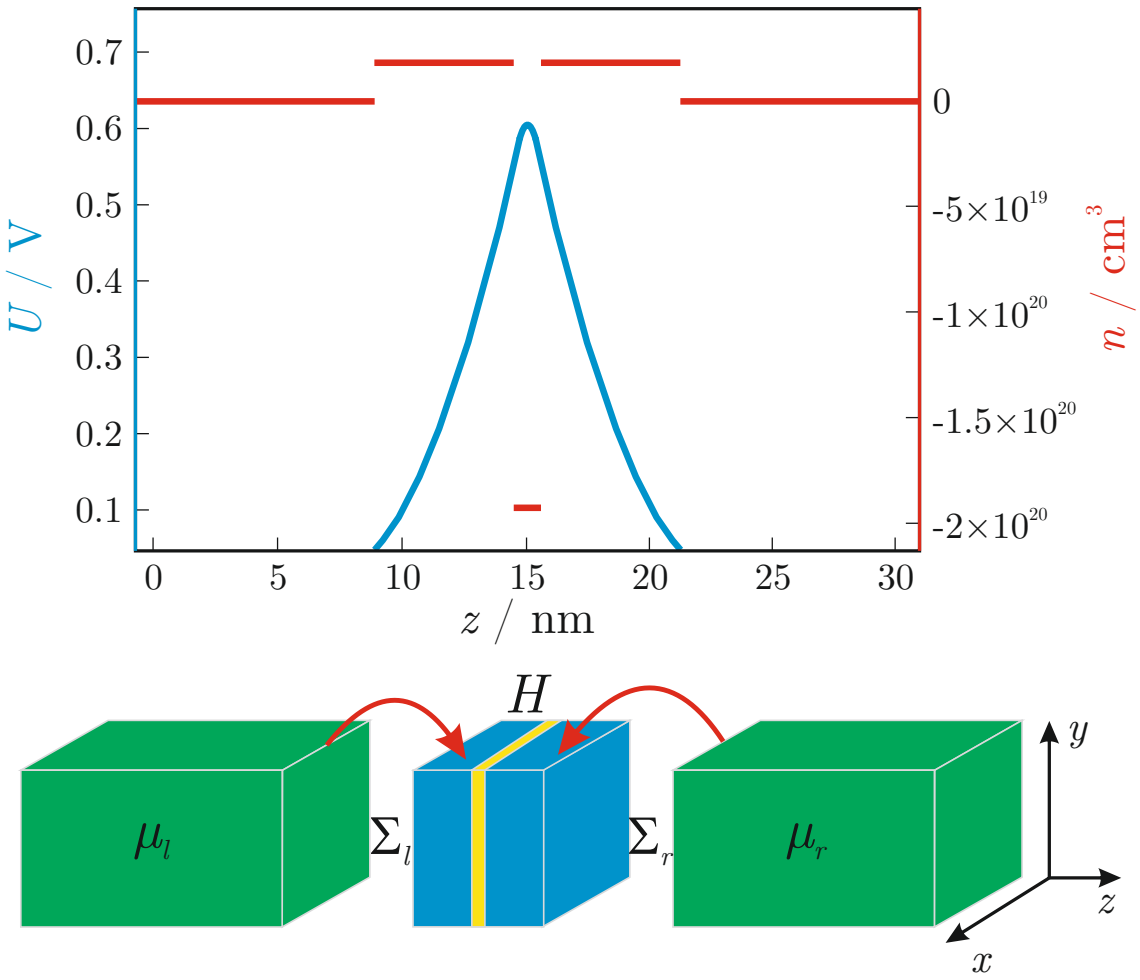

Figure 5.1: Visualisation of the geometry of the considered structure (bottom). The actual interface with its space-charge region is marked yellow. The blue region surrounding it corresponds to the positive space-charge of the grains. The undisturbed parts of the grains are marked green. (image after [93]). The corresponding potential profile (top) in the vicinity of such an interface is represented by the blue curve. The underlying space-charge distribution is indicated by the red curve.

Here $\epsilon_r(x)$ is the dielectric constant, which depends on the space coordinate if different materials are involved. The lower scheme shows the basic idea of the model: For the two directions parallel to the interface a quasi-one-dimensional model is used to describe a layered structure with periodic boundary conditions. In the direction perpendicular to the interface a scattering region is assumed (the grain boundary) that is connected to the semi-infinite grain. The spatial variation caused by the interface needs to be considered in the band structure calculations where an effective mass model is assumed. For the other two directions corresponding parabolic bands are chosen. To calculate ballistic transport through the interface the nonequilibrium Green's function (NEGF) method is applied [95–97]. For the calculation of the current it is necessary to take the coupling of the scattering region to the semi-infinite leads into account. This is done by adding two self-energies,

Σ_l and Σ_r, to the one-band effective mass Hamiltonian H. The Green's function is then calculated by

$$G(E) = (E - H - \Sigma_l - \Sigma_r)^{-1}, \tag{5.20}$$

where E is the transport energy. For the one dimensional transmission probability one obtains

$$T(E) = \mathrm{Tr}\left(\Gamma_l(E)G(E)\Gamma_r(E)G(E)^\dagger\right), \tag{5.21}$$

where Γ_l and Γ_r are the imaginary parts of the left and the right self-energies, respectively. In three dimensions only a fraction of the total energy is available to pass the barrier. This causes a change in the transmission function which has to be considered during the calculation [98]. The current is now given using the well known Landauer formula [95, 96]

$$I = \frac{e}{h}\int T(E)(f_l(E,\mu_l,T_l) - f_r(E,\mu_r,T_r)), \tag{5.22}$$

if the transmission probabilty and the occupation functions of the left $f_l(E,\mu_l,T_l)$ and right $f_r(E,\mu_r,T_r)$ leads are used. The correlation between the thermoelectric coefficients electrical conductivity σ, Seebeck coefficient S and thermal conductivity κ_{el} (for zero electric current) and the transmission function in the linear response regime is given as follows [98–100]:

$$\sigma = (2q^2/h)F_0, \tag{5.23}$$

$$S = [k_\mathrm{B}/(-q)]\frac{F_1}{F_0}, \tag{5.24}$$

$$\kappa_{el} = (T_L 2k_\mathrm{B}^2/h)F_2 - F_1^2/F_0, \tag{5.25}$$

where

$$F_j = \int_{-\infty}^{+\infty}\left(\frac{E-E_F}{k_\mathrm{B}T_L}\right)^j T(E)\left(-\frac{\partial f_0}{\partial E}\right)dE \tag{5.26}$$

with $T(E)$ being the transmission.

Phonon transport across the interface of two materials To calculate the ballistic phonon transport it is necessary to know the equilibrium positions of the atoms and the interatomic force constants (ifcs) between them. These may be derived using the ABINIT program package [101], that is based on density functional theory (DFT). The results of the DFT calculation can be used in an atomistic Green's function (AGF) to obtain the density of states as well as the transmission function. The thermal conductance is obtained within the linear response regime. The AGF approach is a suitable method to calculate ballistic phonon transport since the results in literature [102–105] show good agreement with experiment. Next to this other models are used to calculate phonon transport but they give only an approximative description of it because they do not take into account the structure of the interface. These are the acoustic mismatch model (AMM), which is only valid for long wavelength phonons and the diffusive mismatch model (DMM), that assumes diffuse scattering at the interface [106].

The first part of the calculation, as mentioned above, is to find the equilibrium positions of the atoms and to determine the interatomic force constants. This approach is just shortly outlined here. More details can be found in references [107] and [108].

In order to calculate the ifcs the package ABINIT [101] can be used. This code is based on DFT and can be used with a pseudopotential method and a plane-wave expansion.

For the exchange correlation potential, the local density approximation (LDA) is applied. The pseudopotentials are represented in the Troullier-Martins scheme [109]. The code uses a perturbation method to calculate the dynamical matrix on a discrete grid in the Brillouin zone. The use of a perturbation method avoids the use of super cells. Then the ifcs can be obtained by a discrete inverse Fourier transformation of the discrete dynamical matrix. Knowing the ifcs the dynamical matrix can be calculated for the entire Brillouin zone. Furthermore, also based on the same perturbation method, the code can be used to calculate the dielectric permittivity tensor and the Born effective charges. Knowing the dielectric permittivity and the Born effective charges the ifcs can be decomposed in a long range part which describes the dipole-dipole interaction and a short range part which describes the electronic contribution to the interaction.

The following part is supposed to outline the calculation of the transmission function and the thermal conductance using the atomistic Green's function, whereas the ifcs from the first part are used to describe the interatomic potential. Here only the harmonic part of the potential is considered. Basically the anharmonic effects can be considered by introducing additional self-energies in the AGF method.

At the beginning the interactions of the atoms in the system need to be defined and the harmonic matrix H needs to be set up. To describe the interactions the ifcs obtained from *ab initio* calculations are used. So the interaction between atom μ and atom η is represented by a 3×3 matrix. The corresponding elements are:

$$H_{\mu_i \eta_j} = \frac{1}{\sqrt{M_\mu M_\eta}} k_{\mu_i \eta_j}, \tag{5.27}$$

where M_μ and M_η are the masses of the atoms. $k_{\mu_i \eta_j}$ is the force constant that describes the impact on atom μ in direction i if atom η is dislocated in direction j and vice versa. If there is periodicity in all three dimensions one can built the dynamical matrix which is the Fourier transform of the harmonic matrix

$$D(\vec{q}) = \sum_{\vec{R}} H(\vec{R}) e^{-i\vec{q}\vec{R}}. \tag{5.28}$$

$\vec{R}$ is a lattice vector in real space and $H(\vec{R})$ contains all interactions between cells that are connected by $\vec{R}$. The phonon dispersion relation can be obtained by the square root of the eigenvalues of the dynamical matrix. The density of states can be calculated using the Greens function of the system

$$G(\omega) = (\omega^2 I - H - \Sigma_L - \Sigma_R)^{-1}, \tag{5.29}$$

where Σ_L and Σ_R are the self energies for the left and right contact, respectively [110]. The self energies can be calculated using

$$\begin{aligned} \Sigma_L &= T_L g_l T_L^\dagger \\ \Sigma_R &= T_R g_r T_R^\dagger. \end{aligned} \tag{5.30}$$

Knowing the average transmission one can calculate the total energy flux per unit area J in the linear response

$$J = \frac{1}{2\pi} \int_0^\infty \hbar t(\omega) \frac{\partial f(\omega, T)}{\partial T} d\omega \Delta T, \tag{5.31}$$

where $f(\omega, T)$ is the occupation function for the phonons.

The thermal conductance per unit area is defined as

$$\kappa = \frac{J}{\Delta T} = \frac{1}{2\pi} \int_0^\infty \hbar t(\omega) \frac{\partial f(\omega, T)}{\partial T} d\omega. \tag{5.32}$$

If the exact structure of the interface is unknown one can estimate the interface conductance between material a and material b within the diffuse mismatch model [106]. For the transmission function it is assumed that at the interfaces of the phonons lose memory of their original state and are either scattered in material a or material b. The corresponding probability is proportional to the transmission function of the bulk materials. The transmission function is normalized such that for an interface between the same material the overall transmission is 1/2 of the bulk transmission:

$$t(\omega) = \frac{t_a(\omega) t_b(\omega)}{t_a(\omega) + t_b(\omega)}. \tag{5.33}$$

$t_a(\omega)$ and $t_b(\omega)$ are the bulk transmission functions.

These considerations can now be used to estimate the influence of interfaces between two different materials on the thermoelectric transport parameters on a microscopic level. These calculations may then serve as empirical input parameters for a network model that can simulate the macroscopic behaviour of a nanostructured sample.

5.3 The network model NeMo

As indicated above, the *ab initio* approaches are in principle restricted to microscopic length scales. For a macroscopic treatment of a nanostructured material, a phenomenological resistor network model seems to be the right tool. Here the microscopic parameters are treated as empirical parameters, meaning that they can be either implemented from fitted experimental data or by using *ab initio* calculations.

To connect the locally varying thermal and electrical transport paramaters and hence to describe the transport in the network, the model uses Kirchhoff's laws. For this the nanostrucuture to be investigated firstly needs to be mapped onto a resistance and Seebeck network. This is indicated in the figures 5.2 and 5.3. As can be seen, the superlattice structure with interface roughness is only described in two dimensions, to keep the computational effort low. If the third dimension is assumed to be a periodic crystal, this is justified. Of course, the network model can be extended to the third dimension. In this case the number of nearest neighbours of a given node has to be increased from four (in 2D) to six (in 3D). This becomes relevant e.g. in the case of percolation paths through the sample, which have different critical thresholds in two- and three dimensions. Nevertheless all formulas that are dicussed below are unaffected by the dimensionality. The real macroscopic structure is translated into a pixel grid where microscopic features such as grains or irregularities at the interfaces may occupy several pixels. Here the size of one pixel has to be larger than the mean free paths of electrons and phonons, since the model is based on diffusive transport. Depending on the particular situation, one has to compromise between the edge length L of one pixel and still guaranteeing that L is larger than the mean free paths of electrons and phonons to have the best resolution. Since no exact formula exists, the optimum value of L cannot be simply derived. With the resulting pixel grid three different networks can be set up: a thermal, an electric (both in

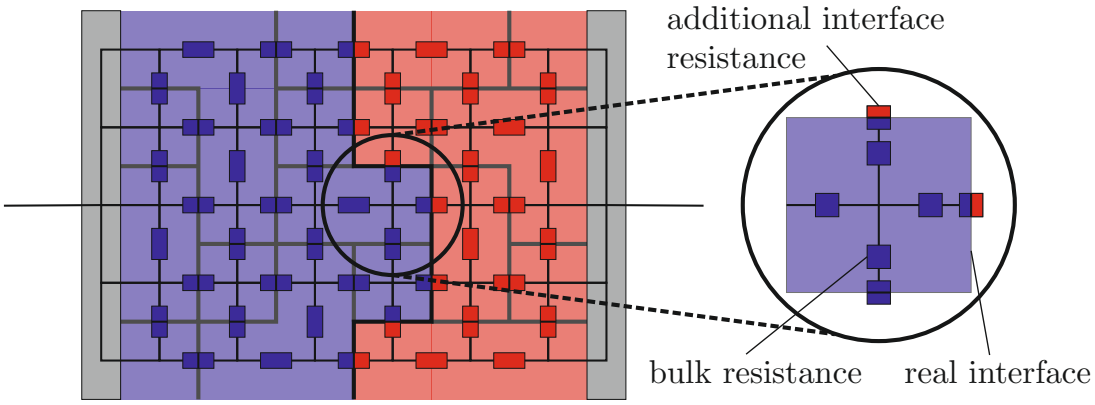

Figure 5.2: Scheme of the two dimensional network model for the electrical and thermal transport simulation. One can see two different materials, consisting of red and blue pixels of the same size, and the interface between them (big black line). The gray lines are interfaces between grains. If an interface is present between two nodes of the network the resulting resistance consists of two bulk resistances and an additional interface resistance in series. This is indicated in the magnification of a pixel centered around a node with the corresponding four bulk resistances. If a real interface is located between two nodes of the network, additional interface resistances are connected in series.

figure 5.2), and a Seebeck network (figure 5.3). To calculate the macroscopic transport properties across the sample each network has two macroscopic contacts where electrical voltages or external temperature differences can be applied.

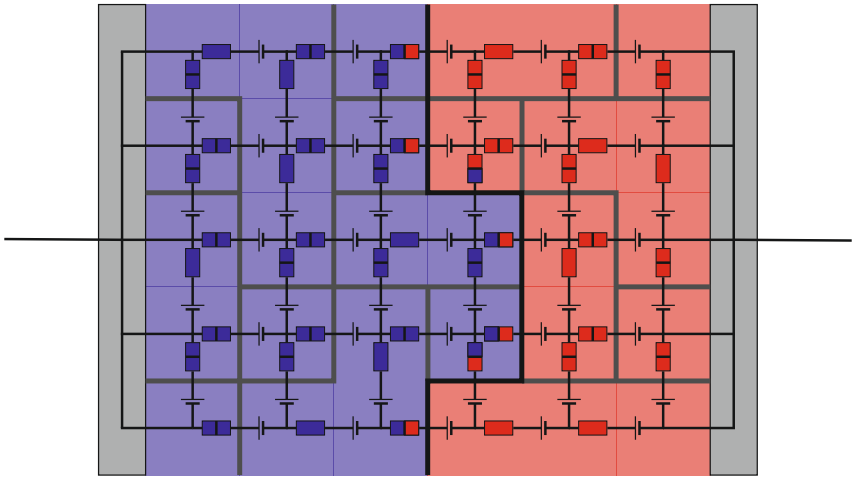

Figure 5.3: Scheme of the two dimensional network model for the Seebeck simulation. Again one can see two different materials. At interfaces there are two bulk voltage sources and one interface voltage source each with an electric resistance in series.

Now each pixel is centered around one node. For the thermal and electric network the nodes are connected to the nearest neighbours via a resistance. This resistance can be

varied by a sum of resistances accounting for a material dependent bulk-like resistance and, if there is a microscopic interface present between two cells, also for an additional interface resistance (cf. magnification in figure 5.2). The latter are introduced to account for microscopic effects of the transport at interfaces such as phonon scattering, electron tunneling, etc. and are incorporated into the network model by single numbers representing the findings from quantum physics calculations. This, at the first glance crude approximation, however enables one to study the impact of these microscopic interface effects on the macroscopic transport coefficients S, σ, and κ of the underlying thermoelectric composite material.

For the actual calculation of the total resistance and the local temperature or electric potential differences of the thermal or electric network a nodal analysis is used employing Kirchhoff's current law. The following equations are valid for the electric network only. Those for the thermal network are basically the same, but instead of the electric potentials φ_k, which can arbitrarily standardized, the absolute temperatures T_k are used. Furthermore the electrical conductivities G are replaced by the thermal conductivities κ. According to Kirchhoff's law one obtains an expression for node k:

$$\begin{aligned} 0 &= \sum_{l\neq k} I_{k,l} = \sum_{l\neq k} [\Delta\varphi_{k,l} \cdot G_{k,l} + i_{k,l}] \\ &= \sum_{l\neq k} [(\varphi_k - \varphi_l) \cdot G_{k,l} + i_{k,l}] \\ &= \sum_{l\neq k} \varphi_k \cdot G_{k,l} - \sum_{l\neq k} \varphi_l \cdot G_{k,l} + \sum_{l\neq k} i_{k,l} \end{aligned} \tag{5.34}$$

Here $\Delta\varphi_{k,l}$ is the voltage between the node k and l and $I_{k,l}$ is the current from node k to node l. $G_{k,l}$ is the conductivity between node k and node l and is non-zero only when k and l are nearest neighbours. $\varphi_{k(l)}$ is the potential at the node $k(l)$. The current from node k to node l is induced by a current source between the nodes and is labelled with $i_{k,l}$. The current sources are necessary to simulate a current between the two macroscopic contacts and hence to calculate the macroscopic resistance of the structure. Furthermore they are used to implement the Seebeck voltage sources as current sources. To combine the equations for all nodes one can write down a matrix equation:

$$\Lambda \cdot \vec{\varphi} = \vec{i}, \tag{5.35}$$

where the elements of $\vec{\varphi}$ are the electric potentials φ_l and the conductivity matrix is given by

$$\Lambda_{k,l} = \begin{cases} \sum\limits_{h=1;h\neq k}^{n} G_{k,h} & l = k \\ -G_{k,l} & l \neq k. \end{cases} \tag{5.36}$$

The current vector $\vec{i}$ is determined by

$$i_k = \sum_{h\neq k} i_{h,k}. \tag{5.37}$$

In order to really carry out the nodal analysis one has to set up the conductivity matrix Λ and the current vector $\vec{i}$ and then solve the system of linear equations that is given by equation (5.35). The corresponding solution vector $\vec{\varphi}$ contains the electrostatic potential

at each node and hence the potential difference between the two macroscopic contacts can be derived. In addition it contains information about the potential differences between neighbouring nodes, which can be used to calculate local electric and thermal currents to illustrate the influence of the geometry on the thermoelectric properties of the structure.

For the calculation of the Seebeck coefficient of a given structure, a different network needs to be set up. Here, similar to the electric network, each node is connected to its nearest neighbours via a bulk resistance and, if necessary, by an additional interface resistance in series. In order to represent the local Seebeck voltage $U_{i,j}$ an additional voltage source is connected in series. $U_{i,j}$ is the voltage between the nodes i and j and is calculated from the local bulk Seebeck coefficients S_i and S_j, the interface Seebeck coefficient $S_{\text{interface}}$ and the local thermal potenial difference $\Delta T_{i,j}$ which is determined by the absolute temperature distribution T_i obtained from the nodal analysis of the thermal network:

$$U_{i,j} = \left(S_i \cdot \frac{\kappa_{i,j}}{\kappa_i} + S_j \cdot \frac{\kappa_{i,j}}{\kappa_j} + S_{\text{interface}} \cdot \frac{\kappa_{i,j}}{\kappa_{\text{interface}}} \right) \cdot \Delta T_{i,j}. \tag{5.38}$$

In this equation κ_i and κ_j denote the thermal conductivities of node i and j. $\kappa_{\text{interface}}$ is the thermal conductivity of the interface between node i and node j and $\kappa_{i,j}$ is the conductivity of the serial connection of the three thermal resistances:

$$\frac{1}{\kappa_{i,j}} = \frac{1}{\kappa_i} + \frac{1}{\kappa_j} + \frac{1}{\kappa_{\text{interface}}}. \tag{5.39}$$

The local voltage sources are implemented as their Norton equivalents, consisting out of a resistance and a current source. This has the consequence that in equation (5.35) $i_{k,l}$ becomes

$$i_{k,l} = G_{k,l} U_{k,l}. \tag{5.40}$$

With the nodal analysis it is possible to determine the Seebeck voltage between the two macroscopic contacts. It is equal to the Seebeck voltage across the entire sample structure. Having this, the total Seeebeck coefficient is given by the ratio of the Seebeck voltage and the applied temperature difference $\Delta T = T_{\text{h}} - T_{\text{c}}$ between hot and cold electrode.

All transport parameters like thermal, electric conductivities and Seebeck coefficients in the bulk and at interface, that have been discussed until now, are considered to be temperature independent. These parameters can be chosen either from experiment, from theory or just as best guesses. Basically it is easy to implement a temperature dependence into the Seebeck and the electrical network. Generally the equations [111] for the electrical current density j_c

$$j_c = \sigma \cdot \Delta U - \sigma \cdot S \cdot \Delta T \tag{5.41}$$

and thermal current density j_q

$$j_q = \sigma \cdot \Pi \cdot \Delta U - \kappa_0 \cdot \Delta T \tag{5.42}$$

with their respective conditions

$$\Delta j_c = 0 \tag{5.43}$$

and

$$\Delta j_q = \frac{j_c^2}{\sigma} + j_c \cdot S \cdot \Delta T \tag{5.44}$$

need to be solved self consistently.

6 Results

The effects that may influence the Seebeck coefficient S are manifold. First S as a function of the carrier concentration n is discussed. By annealing thin sputtered ZnO:Al films n is varied by several orders of magnitude which causes drastic changes in the behaviour of S ranging from degenerately doped via metallic to semiconducting characteristics. In addition these sputtered thin films are investigated with respect to the magnitude of energy filtering effects at grain boundaries as a function of carrier concentration. By generating additional surface states by microstructuring the carrier concentration and sample morphology was manipulated. The measured Seebeck coefficients of this sample series were also qualitatively compared to $NeMo$ simulations.

Concerning the impact of interfaces on the Seebeck coefficient and the electrical conductivity σ multilayer ZnO/ZnS samples as well as laterally structured ZnO thin films grown by various methods and with different dopants and doping concentrations were investigated. The thermoelectric parameters of the multilayers were measured in in-plane geometry whereas the lateral bar structures were aligned parallel as well as perpendicular to the main direction of the transport path. Here S and σ were not just probed across the entire sample but also locally to obtain a deeper understanding of the microscopic behaviour of these quantities. Again $NeMo$ calculations were employed to complete the analysis.

6.1 Influence of the carrier concentration and manipulation of the free carriers

A $Zn_{0.98}Al_{0.02}O$ film with a thickness of about 700 nm was grown by RF sputtering on a glass substrate. The free carrier concentration, determined by Hall measurements at room temperature, was $8.0 \times 10^{20}\,\mathrm{cm}^{-3}$. By annealing pieces of the same specimen in air at 400 °C for different intervals of time, the free carrier concentration can be varied within the series of sample pieces by several orders of magnitude keeping the structural integrity [112]. The mobility values are about $5.5\,\mathrm{cm}^2/\mathrm{Vs}$ independent of annealing.
For the thermoelectric measurements, indium was applied to the ends of the samples to create Ohmic contacts. CuNi/NiCr thermocouples were soldered into the In contacts. The experimental setup used is described in section 3.1.

Fig. 6.1 depicts the temperature-dependent measurements of the Seebeck coefficient S for the series of (Zn,Al)O samples in the range from 50 K to 300 K. The sample with the lowest carrier concentration n of $1.5 \times 10^{18}\,\mathrm{cm}^{-3}$ exhibits the behaviour expected for a typical n-type semiconductor. S is negative and its absolute value decreases slightly in the range from 300 K down to about 80 K, on decreasing the temperature further the absolute value increases again due to the phonon drag effect. An explenation for the phonon drag effect was given by Frederikse [113] and Herring [114] independent of each other: If a temperature gradient is present the phonons are not longer isotropic but tend to flow from the hot to the cold side. Hence the scattering of the phonons with charge carriers

occurs preferably towards the cold side. This results in an enhancement of the diffusion of the charge carriers, they are dragged by the phonons. The thermovoltage characterizes the stationary state where the diffusion is just compensated by a field which is induced by the thermovoltage. At a given temperature difference the phonon drag leads to an increase of the thermovoltage and hence to an increase of the Seebeck coefficient. The effect occurs preferably at low temperatures, because with increasing temperature the phonons lose their directed nature, e.g. due to scattering processes with each other, in particular, Umklapp-processes. The strong increase of the absolute value of $|S|$ due to phonon drag is independent of its sign and thus independent of the type of semiconductor. A detailed theoretical description of the phonon drag effect can be found elsewhere [114].

The value of about $S = -350\,\mu\mathrm{V/K}$ at 300 K is typical for ZnO with such a carrier concentration [54]. The value of the Seebeck coefficient of the sample with the second lowest carrier concentration ($1.6 \times 10^{19}\,\mathrm{cm}^{-3}$) is about $S = -190\,\mu\mathrm{V/K}$ at 300 K. The decrease of the absolute value of S with decreasing temperature below 300 K becomes more pronounced and the phonon drag effect is weaker, i.e. is suppressed with increasing carrier concentration [114]. The temperature behaviour of the Seebeck coefficient of the sample with $n = 1.0 \times 10^{20}\,\mathrm{cm}^{-3}$ follows the expected trends. $|S|$ is further decreased (-30 μV/K at 300 K), but still found to increase with increasing temperature, and the phonon drag effect is no longer observed. The Seebeck coefficient of the sample with the highest carrier concentration ($8.0 \times 10^{20}\,\mathrm{cm}^{-3}$) is, as expected, smaller again, but exhibits temperature characteristics which are entirely different from these considered typical for semiconductors. The Seebeck coefficient, though the material is clearly n-type, is positive at room temperature ($S = 1\,\mu\mathrm{V/K}$). It changes sign with decreasing temperature at about 250 K and remains negative down to the temperature of 50 K with a minimum value of -1 μV/K at about 120 K.

The reason of the sign reversal of S needs to be sought in the metal character of this sample. In solid solutions of metals containing transition metals, S changes sign with composition x at $T = 0\,\mathrm{K}$ [115]. Theoretical studies relate this sign reversal in solid solutions of metals to bandstructure effects, i.e. to changes of the density of states at the Fermi energy E_F. The temperature dependence for fixed x can be discussed along the same line, i.e. E_F shifts with temperature and the Fermi distribution broadens, thus, the parts of the bandstructure contributing to the Seebeck effect will vary with temperature. In the solid solutions of metals the anomalies in the density of states are caused by the d-electron band of the transition metal constituent and its position with respect to E_F.

The situation in the metal solid solutions resembles that in degenerately doped semiconductors [116] (see Fig. 6.2). Far below the Mott critical value, the density of states of the s-like conduction band of the semiconductor is quasi-parabolic and the δ-like localized donor levels are separated from the conduction band by a gap. The extended conduction band states carry the entire transport whereas the localized donor states only serve as a carrier reservoir. Above the critical Mott value, the situation has changed, the donor states have merged into an impurity band which overlaps energetically with the s-like conduction band states. The clear distinction between localized donor states and extended band states is lost, and the Fermi-level is shifted into the resulting band. The Mott equation gives an expression for the Seebeck coefficient within the Boltzmann transport-theory at low temperatures [117]:

$$S = \frac{\pi^2}{3}\frac{k_\mathrm{B}^2 T}{e}\,\frac{1}{\sigma(E)}\frac{\partial\sigma(E)}{\partial E}\bigg|_{E=E_\mathrm{F}}, \tag{6.1}$$

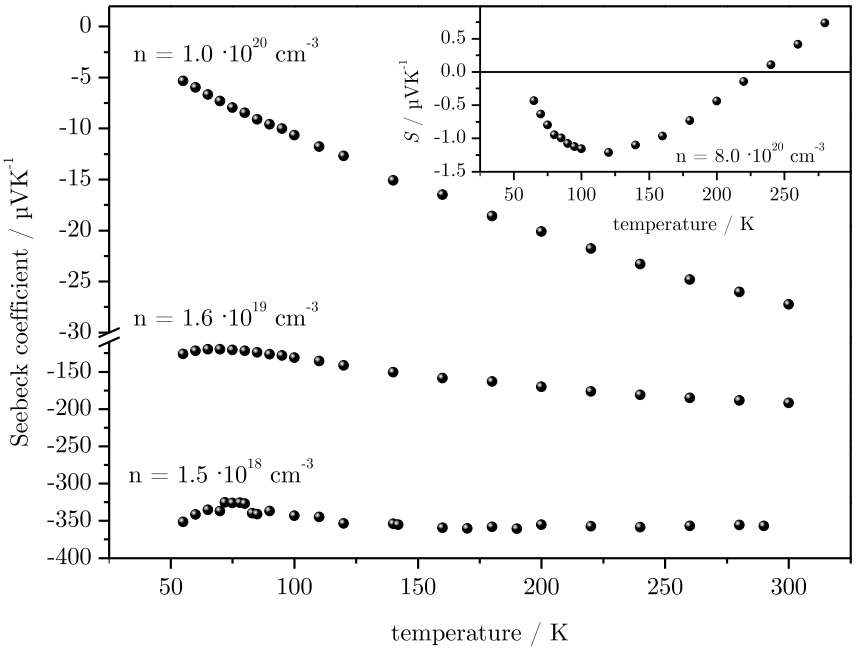

Figure 6.1: Temperature-dependent Seebeck coefficients of n-type $Zn_{0.98}Al_{0.02}O$ with different free carrier concentrations n.

where T is the absolute temperature, k_B is the Boltzmann constant, e is the electron charge, and $\sigma(E)$ denotes the energy-dependent electric conductivity. One may write $\sigma(E_F) = 1/3\rho(E_F)(ev_F)^2\tau$ where v_F and τ are the Fermi velocity and the relaxation time, respectively. $\rho(E)$ is the density of states. Assuming v_F and τ are constant for simplicity, Eq. (6.1) yields immediately that $S \propto [\partial\rho/\partial E]_{E=E_F}$. Thus the sign of S may be affected by the sign of $[\partial\rho/\partial E]_{E=E_F}$ which changes depending on the position of the Fermi energy within the conduction band as can be seen in Fig. 6.2 (bottom). In addition, of course, the Fermi distribution broadens and the dominant scattering mechanisms will vary with temperature T and energy E.

6.2 Influence of grain boundaries - energy filtering?

A thin film that is deposited by sputter deposition, always consists of grains of different sizes. These can vary depending on the growth conditions between 10 and 100 nm (cf. figure 6.3). This again determines the density of grain boundaries which act as a barrier for electrons. In figure 6.4 such a barrier is schematically illustrated. At the grain boundaries the Fermi energy E_F is pinned to the localised boundary states [119]. In the case of Al doped ZnO these states are negatively charged causing a bending of the conduction band. This bending acts as potential barrier of height E_b. If now the charge carriers with a certain energy distribution are to pass this barrier, it comes to a strong backscattering of those carriers which have energies smaller than E_b. This causes a change in energy

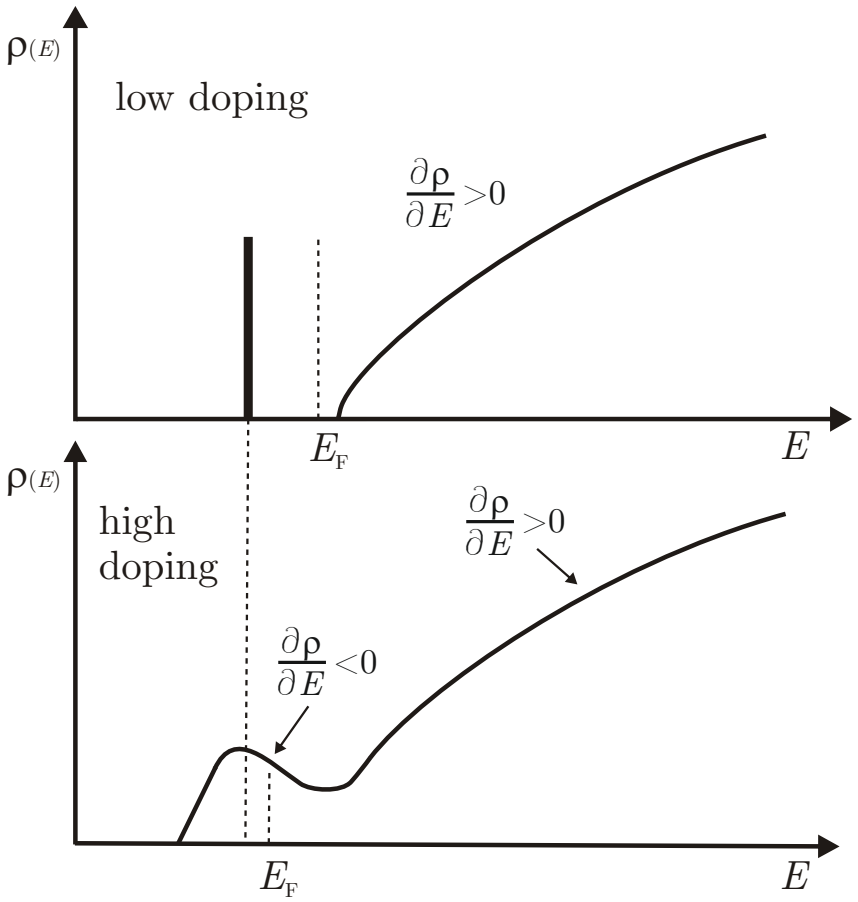

Figure 6.2: Density of states $\rho(E)$ in a non-degenerate (top) and a degenerate (bottom) n-type semiconductor.

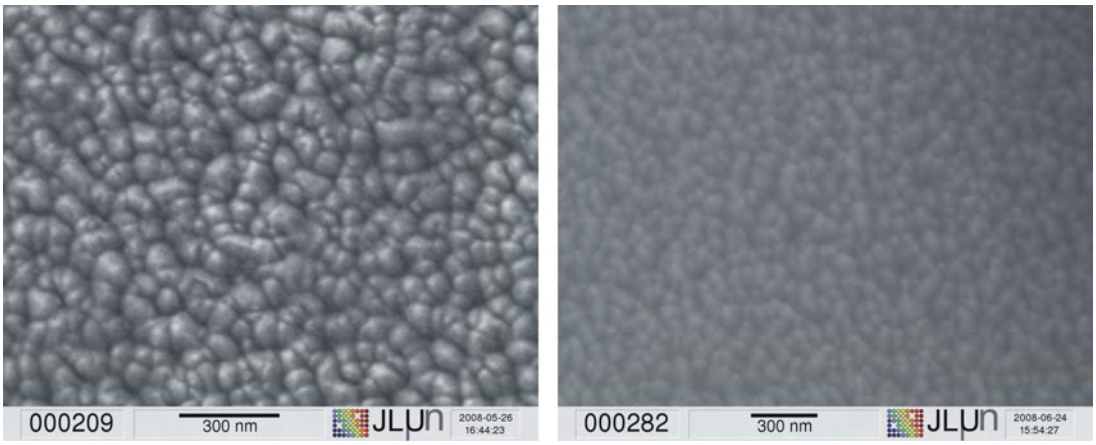

Figure 6.3: SEM images of a sputtered $Zn_{0.98}Al_{0.02}O$ layer before (left) and after (right) annealing. One can see that the grain boundaries are less pronounced after the annealing process causing a lowering of the potential barrier. This again has a direct impact on the electrical properties of the sample and hence on the Seebeck coefficient.

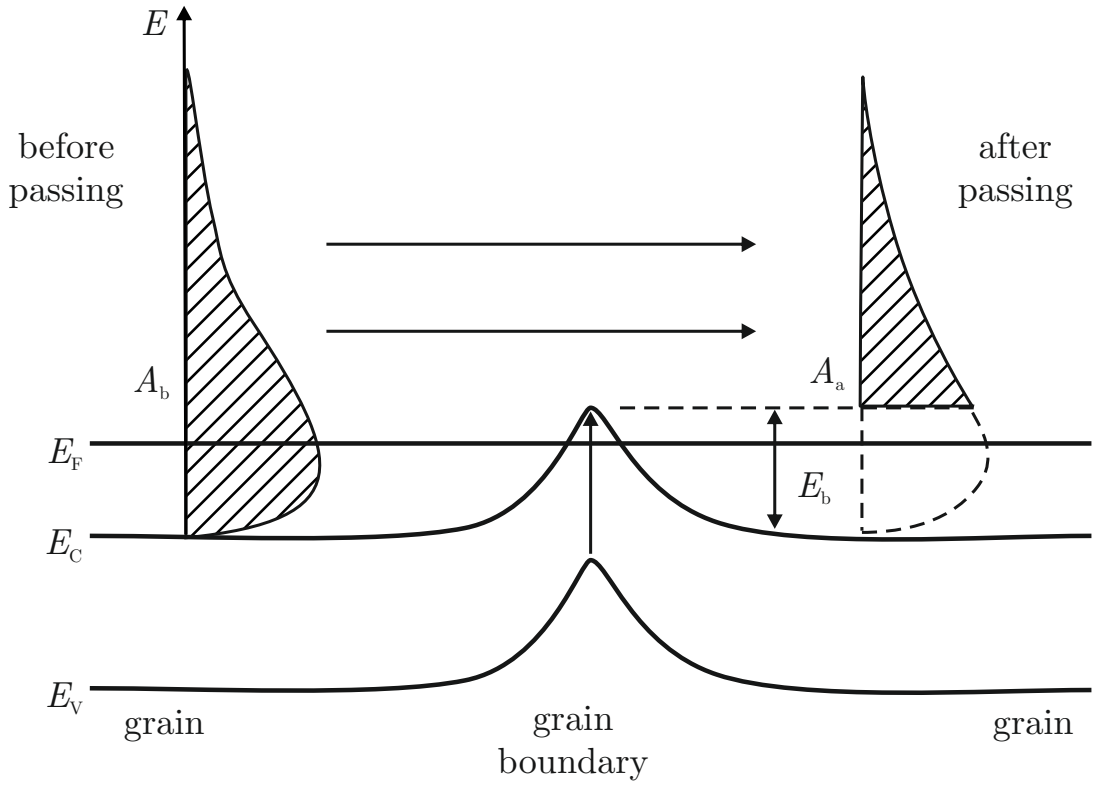

Figure 6.4: Schematical depiction of the energy filtering through a potential barrier, so called double Schottky barrier, at grain boundaries (sketch after [118]).

distribution before (area A_b) and after (area A_a) passing the barrier. This energy filtering influences the electrical conductivity and hence the Seebeck coefficient of the material.

Energy filtering effects due to grain boundaries have been studied theoretically by Bachmann et al.. The main findings of these investigations shall be given here:

The model used for the calculations is based on that established by Seto et al. [94]. The basic idea is, that the grains offer additional surface states at their boundaries which can trap electrons from the donor states (see figure 6.5). This results in a negative charge accumulation at the grain boundaries and a corresponding excess of positive charge carriers in the vicinity of the grain boundaries. The consequence is a bending of the energy bands on both sides of the grain boundary forming a so called double Schottky barrier. For the case that the donor concentration N_D within the grain of a length l_g is higher than the number of surface states N_T of the interface with a dimension l_i, i.e. $l_g \cdot N_D > l_i \cdot N_T$, the calculated potential profile $V(x)$ (equation (5.19)) has the shape shown in the top graph of figure 5.1. Calculations show that with increasing doping concentration the height and the width of this potential barrier decrease strongly. To determine the transmission function as well as the thermoelectric coefficients one can use the formalisms presented in section 5.2.

In a first simple model the highest enhancement due to energy filtering across a barrier is investigated assuming a step-like one-dimensional transmission function $T_\mathrm{1D}(E)$ of the

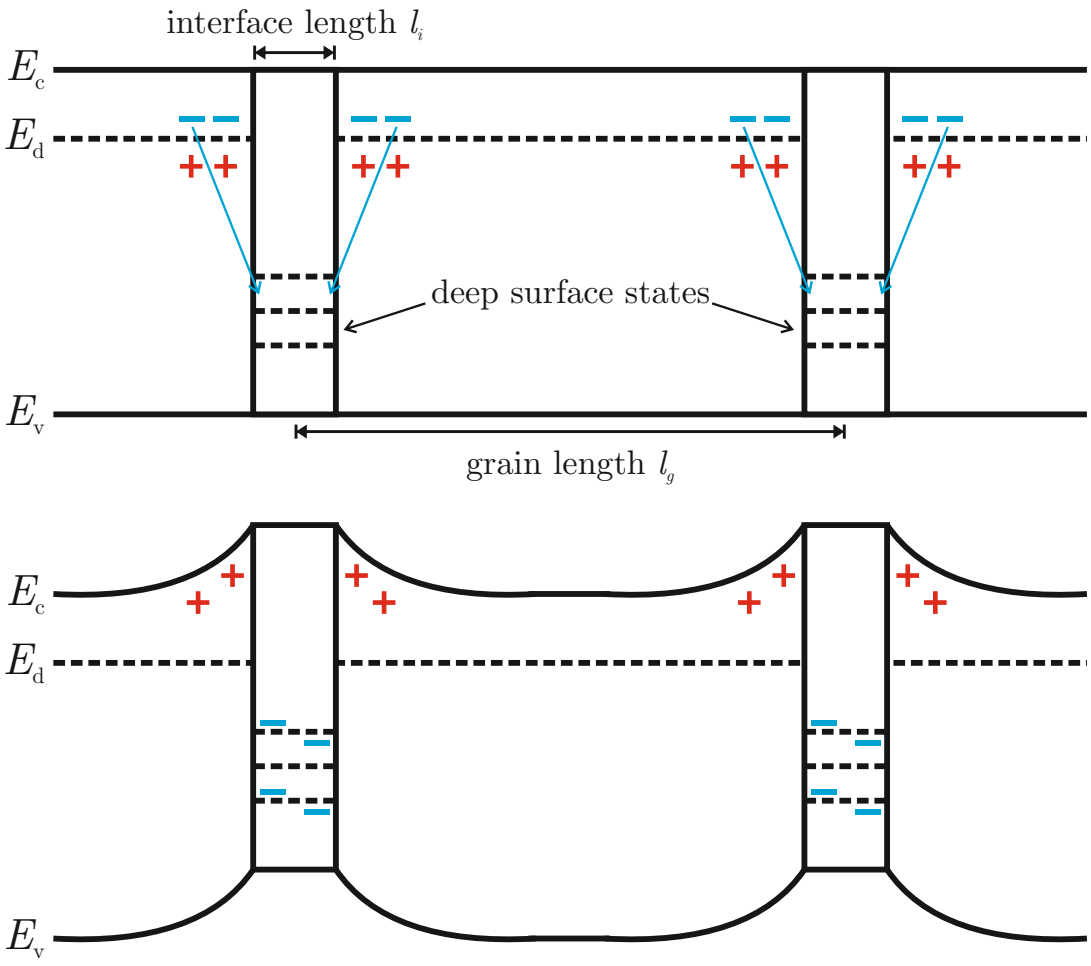

Figure 6.5: Scheme of the band diagram in real space before (top) and after (bottom) the formation of a double Schottky barrier. E_c denotes the energy at the bottom of the conduction band, E_v the top of the valence band, and E_d shows the energetic position of the donor states.

form:

$$T_{1D}(E) = \begin{cases} 1 & E > E_b \\ 0 & E \leq E_b. \end{cases} \tag{6.2}$$

Here E_b is the barrier potential height. For the investigations typical semiconductor parameters were chosen, to allow as general statements as possible ($m_{eff} = 0.25$, $\lambda = 20\,\text{nm}$, and $T = 300\,\text{K}$).

To estimate if barriers can have an additional positive influence on the thermoelectric parameters, the dependence of the chemical potential μ and the barrier height E_b on the electrical conductivity σ the Seebeck coefficient S and the resulting powerfactor $S^2\sigma$ were calculated for three different grain sizes ($l_g = 50\,\text{nm}$, $100\,\text{nm}$, and $200\,\text{nm}$). The results show a few general trends [120]: The conductivity increases with increasing chemical potential and decreases with increasing barrier height. As a consequence of the $S \propto 1/\sigma$-law the Seebeck coefficient shows the opposite behaviour. From this it follows that the power factor for a given chemical potential is maximal when the barrier height and the

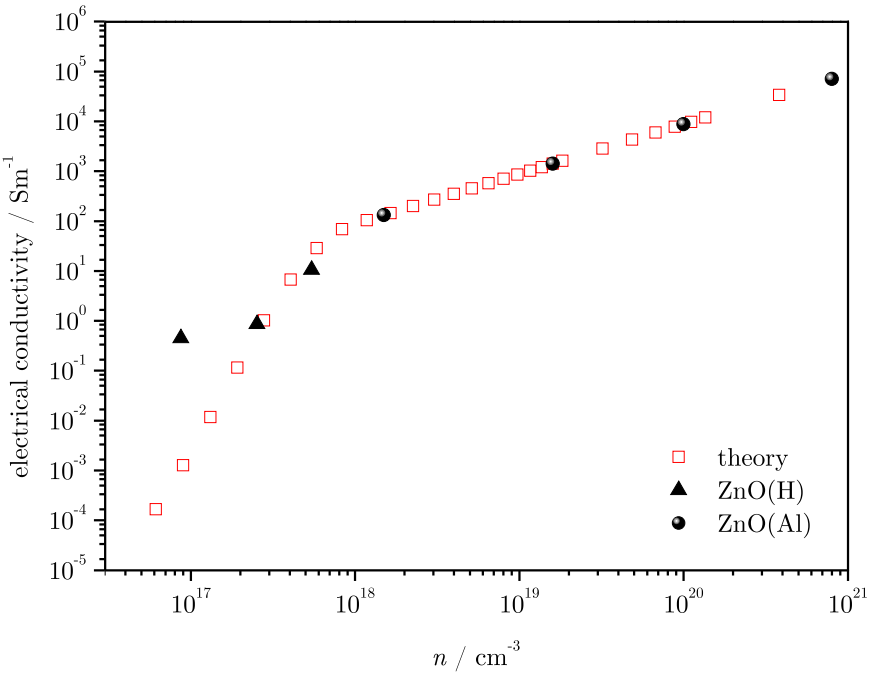

Figure 6.6: Electrical conductivity as a function of the charge carrier concentration n. The experimental data points (filled) served as modeling parameters for a one band effective mass theory (empty squares).

chemical potential have approximately the same order of magnitude. So the power factor can be increased by increasing the chemical potential and finding the optimal barrier height. A global maximum of the power factor, as for the bulk material, cannot be observed in this case.

At first sight, these findings may encourage the idea that a very high chemical potential combined with a suitable barrier height leads to a high thermoelectric figure of merit. This is somewhat misleading since one has to keep in mind, that the electronic contribution to the thermal conductivity increases as well and at some point is of the same order of magnitude as the phonon lattice conductivity. This leads to a significant contribution to the overall thermal conductivity and hence to a decrease of the thermoelectric figure of merit. For the range of the chemical potential investigated here, κ_{el} is small compared to typical phonon conductivities.

In a more sophisticated model the assumption of a step-like transmission function needs to be discarded, as tunneling effects allow charge carriers to pass through the barrier although their energies are smaller than the barrier height. Furthermore the condition of a high chemical potential and a corresponding barrier height causes some difficulties: A high chemical potential requires a high donor density, which leads to an effective screening of the Coulomb potential. This again reduces height and width of the double Schottky barrier and hence reduces the effect of energy filtering.

Quantitatively the general trends observed for a step-like transmission are in agreement with the more advanced model only in the case of low chemical potentials. Looking at

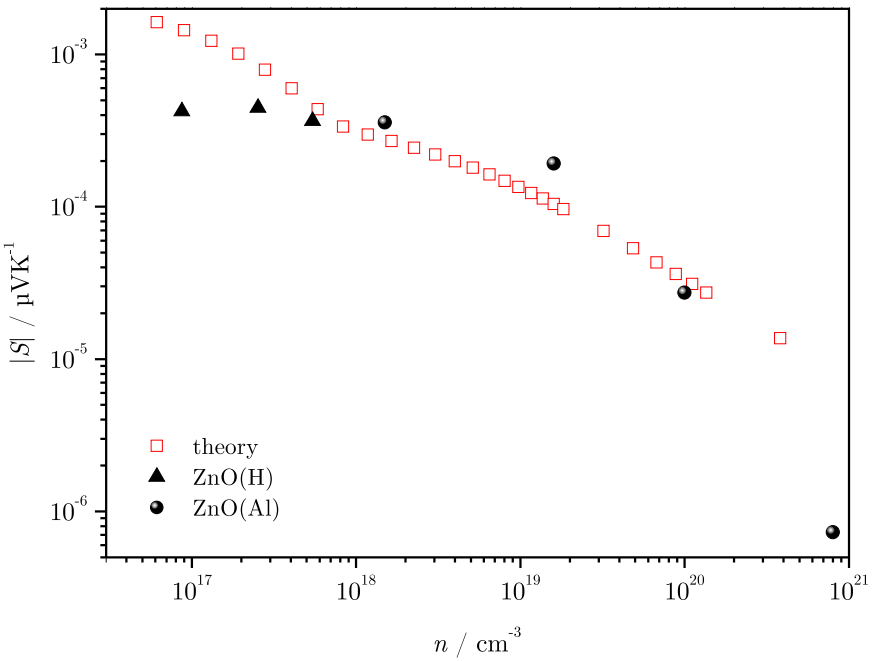

Figure 6.7: Seebeck coefficient as a function of the charge carrier concentration n. For intermediate carrier concentrations the agreement between theory (empty squares) and experiment (filled symbols) is quite good. For higher values of n the assumption of one parabolic band does not hold. For low carrier concentrations the increase of $|S|$ is not as strong as predicted by theory.

the characteristics of the power factor for a given chemical potential as a function of the density of surface states N_T one finds that the power factor is constant for low values of N_T. With a further increase of the density of surface states the power factor decreases strongly and then tends to zero for high values of N_T. The same behaviour is observed for a given value of the chemical potential and a variation of the grain size. It seems that the grain size has only a small effect on the power factor as a function of N_T. Especially a desired enhancement of the power factor is not observed for any of the considered grain sizes in the range from 50 nm to 200 nm.

Above a certain value of the chemical potential, the density of surface states N_T, which determines the height of the barrier, has no further influence on the thermoelectric parameters, e.g. the power factor. In other words a high donor concentration N_D, causes a high effective screening of the Coulomb potential at the grains which decreases the barrier height and width to an extent where it has no further impact on the thermoelectric transport.

To investigate the significance of the model, it is compared with experimental data of the electrical conductivity σ, of the Seebeck coefficient S, and hence of the power factor $S^2\sigma$ as a function of carrier concentration. The experimental values were obtained by taking the measured charge carrier concentrations n from figure 6.1 and then calculating the electrical conductivities after $\sigma = \mu \cdot e \cdot n$. Here a constant value of $\mu = 5.5\,\mathrm{cm}^2/\mathrm{Vs}$ was

assumed, which is in good agreement with experiment for this material [82]. To complete the data for low carrier concentrations measured data points from a sputtered hydrogen doped ZnO series were added.

The theoretical model used is based on one parabolic band with an effective mass of $m_{\text{eff}} = 0.24$ and barrier of a certain height, which has been chosen such that the theoretical data for σ agree as well as possible with the experimental values. As can be seen in figure 6.6 this works well over a wide range of carrier concentrations. With increasing carrier concentration the conductivity at first increases very strongly. With an increasing number of charge carriers the probability to pass the barrier increases significantly and so does the conductivity. The flattening for concentrations higher than $10^{18}\,\text{cm}^{-3}$ is due to the screening of the barrier described above. Above a certain carrier concentration the screening is so high, that the charge carriers no longer "see" the barrier. Effectively the grain boundaries disappear and the material behaves like bulk material.

With the fitting paramters found for the electrical conductivity, the Seebeck coefficient may now be calculated within the same model. The comparison with experiment is shown in figure 6.7. The experimental data for $|S|$ again are taken from figure 6.1 and completed with values from the H doped ZnO series. Now the agreement is good in the intermediate regime only. For high values of n the deviation from the experiment is large, because in this range of high doping, the assumption of a parabolic conduction band does not hold (as indicated in figure 6.2). Therefore this simple model fails for degenerately doped semiconductors. Due to the strong decrease of the conductivity for low n, one would expect an equivalent increase of $|S|$ in this regime. This trend is found in theory only. In the experiment the increase is much less. Whether this deviation stems from a lack of statistics on the experimental side or an oversimplified model on the theoretical side, needs to be clarified in the future.

The deviations found for the Seebeck coefficient become even more pronounced for the power factor, due to its square dependence on the Seebeck coefficient. Nevertheless figure 6.8 indicates that the measured trend can be roughly reflected by the theory. Both curves show a maximum power factor at a charge carrier concentration of about $1.6 \cdot 10^{19}\,\text{cm}^{-3}$. Due to higher Seebeck coefficients in the experiment and almost equal values of σ the power factor peaks at values approximately three times higher than in theory. For very low or very high values of n this difference is even larger, but cannot be distinguished due to a non-logarithmic scaling of the power factor.

In conclusion, a one-band effective-mass model with the assumption of a barrier can reproduce the experimentally found trends suprisingly well. However, the deviations for low and high carrier concentrations, respectively demonstrate the limitations of this model. On the experimental side a higher number of samples in the carrier concentration range of interest needs to be investigated, to obtain a better understanding of the exact progression of S and σ as a function of n.

6.3 Seebeck effect and micro-structuring

Pieces of an as-grown $Zn_{0.98}Al_{0.02}O$ specimen were microstructured in the central area of $5 \times 2.5\,\text{mm}^2$ by photolithography followed by wet-chemical etching. The pattern consisted of a square grid with pitch a. The square-like unit cell had a square-hole (edge length $a/2$) in its center (see figure 6.9). The pitch a varied between 32 and 4 µm. Dividing a by halves corresponds to a doubling of the additional surface due to the hole sidewalls created

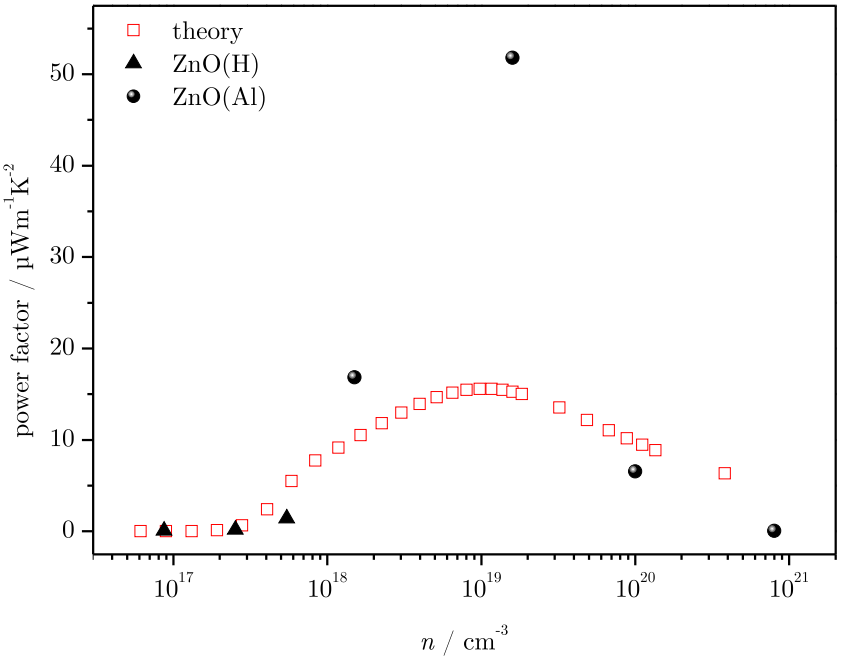

Figure 6.8: Power factor $S^2 \cdot \sigma$ as a function of the charge carrier concentration n. The differences between experiment (filled symbols) and theory (empty squares) originate from the deviations of theoretical and experimental values of the Seebeck coefficient. Nevertheless the general trend can be reproduced.

in the etching process, whilst keeping the sample volume constant. The additional surface is about 6 mm^2 for the smallest pitch. Assuming that every atom at this surface causes a defect, e. g. an electron trap, the total number of free carriers in the microstructured sample is reduced by about 1% compared to the parent thin film. At these high carrier concentrations ($\approx 10^{21}$ cm^{-3}) a loss of 1% should not affect the electrical resistance R dramatically. But as can be seen in figure 6.10 this is not true. With decreasing pitch size the total resistance increases from 4.5 Ω of the reference to 55 Ω for a pitch of 16 µm and 138 Ω for a pitch of 8 µm (all values taken at room temperature). The variation of the resistivity with increasing temperature is very small as expected for such high carrier concentrations. Figure 6.11 shows the Seebeck coefficients S of the series of microstructured $Zn_{0.98}Al_{0.02}O$ samples of different pitch a and of the piece of as-grown $Zn_{0.98}Al_{0.02}O$ (corresponding to $a = \infty$) as a function of temperature. In contrast to the predictions of effective medium theory, a clear dependence on the pitch a of the microstructures is observed. The curves shift to negative Seebeck coefficients with decreasing pitch. The comparably small changes between the samples of nominal pitch of 8 µm and 4 µm are due to the isotropic etching which leads to almost the same hole size in both cases.

To discuss the origin of the observed dependence of R and S on a the following remarks are necessary: (i) As the artificial structuring was performed on the micrometer scale, changes of the densities of states of phonons as well as of electrons can be ruled out. Thus, the observed changes are not due to electronic or phononic confinement. (ii) In

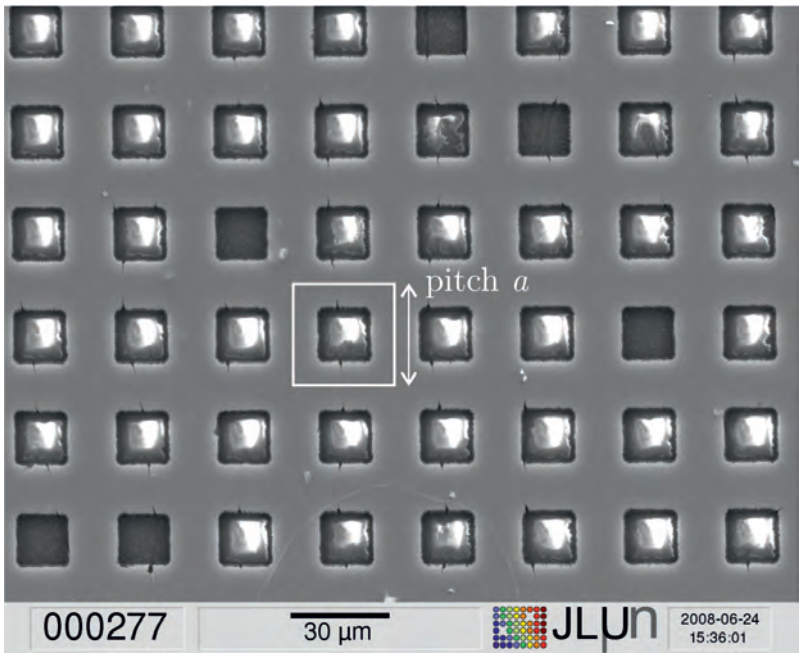

Figure 6.9: SEM image of a microstructured sample with a pitch of $a = 32\,\mu m$. The marked pitch was varied between 32 and 4 µm.

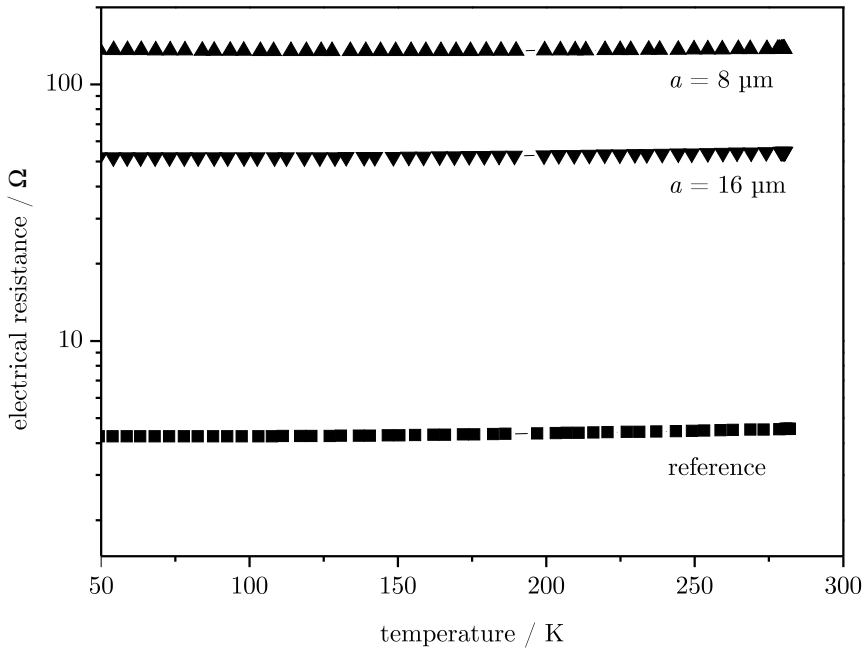

Figure 6.10: Temperature dependence of the resistance of microstructured $Zn_{0.98}Al_{0.02}O$ samples of different pitch a.

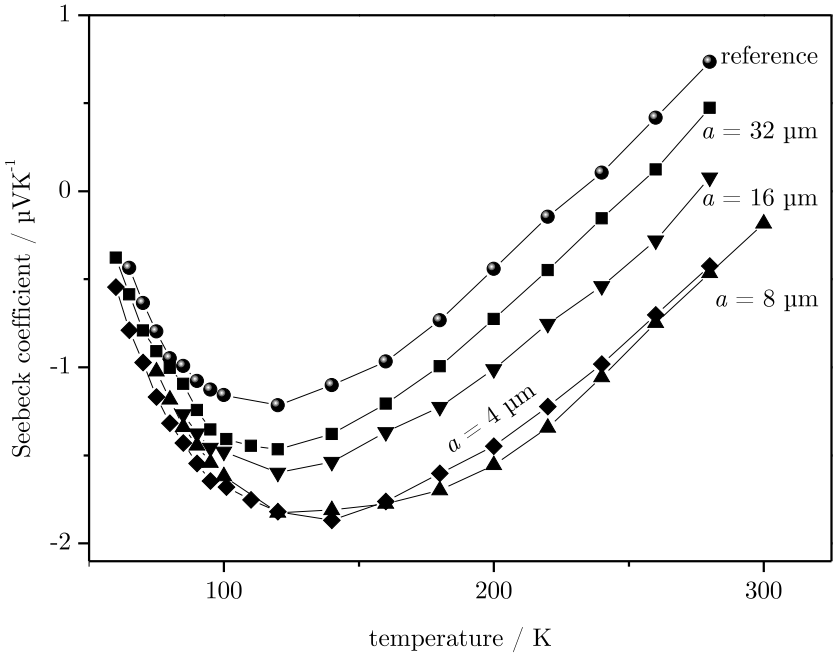

Figure 6.11: Temperature dependent Seebeck coefficients of microstructured $Zn_{0.98}Al_{0.02}O$ samples of different pitch a.

addition to the micrometer scale of the artificial structuring, there are other structural length scales of importance which are the grain size of the crystallites making up the sputtered $Zn_{0.98}Al_{0.02}O$ film as well as the distance between the Al impurities which act as scattering centers for the electrons. The typical diameter of the grains is about 60 nm and the mean distance between impurity ions is about 2 nm, thus both are much smaller than the characteristic length a of the artificial structuring. Moreover, the grain boundaries also serve as barriers for the phonons. Therefore, the mean free paths for electrons and phonons are smaller than the distance between grain boundaries, i. e. the grain size. Consequently, the artificial structuring on the microscale cannot directly affect the mean free paths. As pointed above, the strong changes in R cannot be solely due to electron trapping at the additional surface. There has to be another mechanism that has a bigger influence on the resistance. Figure 6.12 shows an SEM image of the area between two holes of a microstructured sample. In addition to a crack extending through the entire bar between the square holes, one can see small cracks that open up at the edges of each hole. This roughening widening is due to the wet chemical etching process and extends about 2-3 µm into the thin film. The etching rate along the grain boundaries is larger than that of the grains causing the observed morphology at the edges in the wet chemical etching process. This together with the surface region of the hole creates an area of high resistance around each hole. Because the extension of this region is independent of the hole size, its influence on the global resistance of the sample should grow with decreasing pitch size.

To estimate the magnitude of the resistance of this region *NeMo* simulations were carried out. For this bitmaps of 128×128 pixels were drawn simulating the real structures.

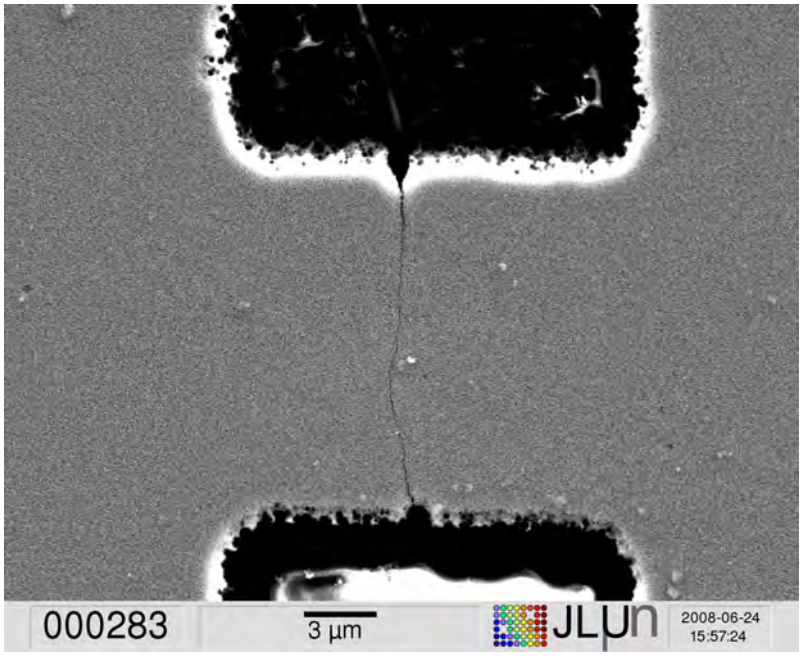

Figure 6.12: SEM image of a thin crack between two holes in the microstructured $Zn_{0.98}Al_{0.02}O$ thin film.

Here it was assumed that one pixel corresponds to 0.5 µm. So the width of this region was set to 6 pixels corresponding to the above estimated 3 µm. For the smallest structures considered, with a pitch of 16 pixels, the highly resistive region is already overlapping between the holes. In this case only two materials had to be accounted for: The hole region, where the resistance was chosen $10^6\times$ higher than the measured reference resistance and the edge region. Here the resistance was adjusted to such a value that the simulated global resistance and the corresponding measured one were in good agreement. Figure 6.13 shows the comparison between simulation (empty symbols) and experimental data (black spheres). All simulated values were normalized to the measured reference value. The upper x-axis corresponds to the simulations and the lower one to the expermiment. A very good agreement for the smallest pitch could be achieved by assuming an edge region resistance that is about 17.5 times higher than the measured reference sample.

For the next bigger pitch size of 32 pixels three different regions had to be taken into account in the simulations. Here the distance between the holes is big enough that the edge regions do not overlap and hence leaves a path of thin-film material. The resistance for the latter was now varied to achieve the best agreement with the expermimental data for this pitch size (16 µm). The other two resistance values remained unchanged. With the three resistance values found in this fashion, the last two pitch sizes were simulated as well. It can be seen that the total resistance drops further and tends to the value of the measured reference indicated by the black line. Nevertheless for a good agreement with the experiment the resistance of the thin film in the simulations had to be chosen about 2.5 times higher than the measured reference resistance. The reason for this may be the existence of the extended cracks which lead to the reduction of possible transport paths in the microstructured samples. Though the unstructured thin film has cracks as well the number of possible paths where electrical transport can circumvent these extended

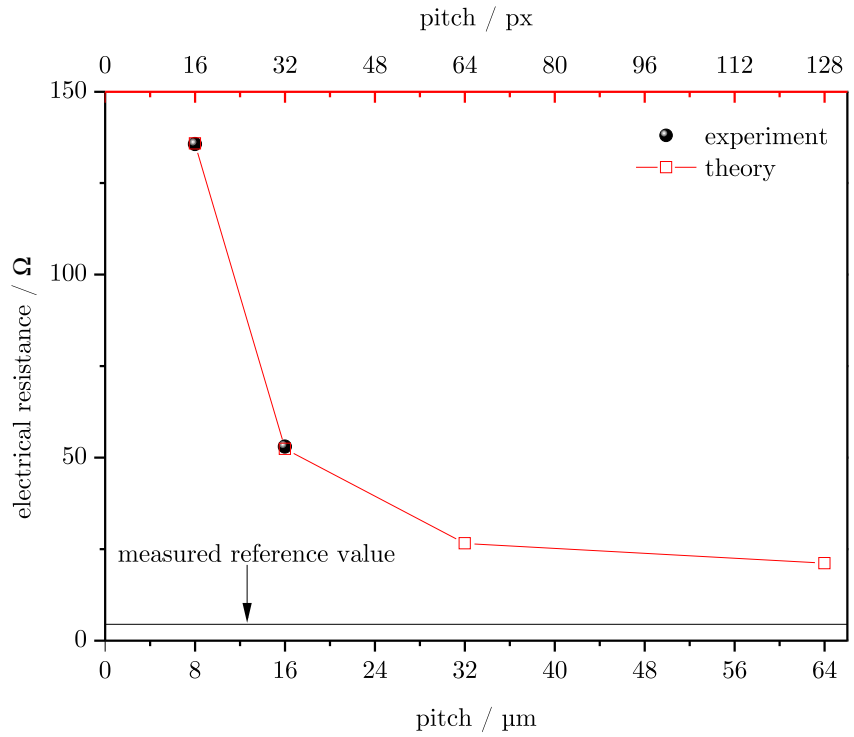

Figure 6.13: Comparison between measured (black spheres) and simulated (empty symbols) resistances of microstructured $Zn_{0.98}Al_{0.02}O$ thin films as a function of pitch size. The black line marks the resistance of the measured reference sample.

cracks is higher than in the structured case, leading to a reduction of the resistance. So for sufficiently high pitch sizes ($> 10\,\mu m$) the resistance of the thin film dominates the electrical transport of the structured samples. Below a critical pitch, where the edge regions start to overlap, the overall resistance of the sample increases strongly.

In the case of simulating the Seebeck coefficient the influence of the edge regions is not so dominant because here additional quatities such as the thermal conductivity as well as Seebeck coefficient itself need to be fed into *NeMo* for each present material. In addition, the cracks play a minor role for S, e.g. the temperature difference across the sample is mainly dominated by the substrate and not by the morphology of the thin film. In figure 6.14 the experimental data at 200 K taken from figure 6.11 are plotted as a function of the pitch a (lower x-axis). The same graph contains *NeMo*-simulations of the Seebeck coefficient (empty symbols) again as a function of the pitch given in pixels (upper x-axis). As for the resistances bitmaps of 128×128 pixels were drawn simulating the real structure. Two examples of these bitmaps can be found as insets in figure 6.14. For the simulations the thermoelectric parameters S, σ, and κ of the three different areas namely thin-film, depletion layer, and substrate region need to be fed into the program. The values of σ and S of the $Zn_{0.98}Al_{0.02}O$ thin-film are known from the experiment. For the Seebeck coefficient a value of $S = -4.4 \cdot 10^{-7}\,\mu V/K$ and for the electrical conductivity $\sigma = 2 \cdot 10^5\,S/m$ were measured. Again the hole region was chosen to have a 10^6 times higher resistivity than the thin film. The resistivity of the depletion layer was now varied

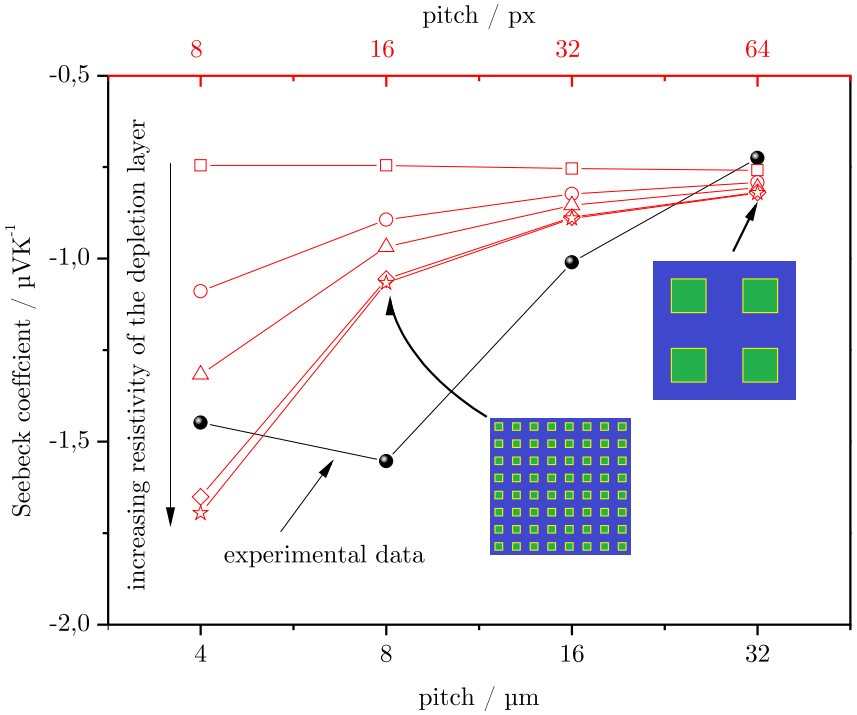

Figure 6.14: Simulation (open symbols) and measurement (black spheres) of the Seebeck coefficient as a function of pitch size. In the simulation the resistivity of the space-charge region was increased, whereas the resistivities of the thin-film and the substrate were kept constant. The insets show pixeled representations of two sample structures of different pitch. The holes are surrounded by a depletion layer of constant width.

to be 2×, 5×, 10×, 100×, and 1000× higher than the resistivity of the $Zn_{0.98}Al_{0.02}O$ layer, respectively. The width of the depletion layer was kept constant at a value of 2 pixel, whereat one pixel was positioned on the thin-film area and the other one on the substrate area. The Seebeck coefficients of the substrate region and the depletion region were adjusted according to $S \propto \rho$, respectively. Because the temperature gradient across the sample is mainly dominated by the substrate, the values for the thermal conductivity of the three different regions were set to unity.

The experimental data in figure 6.14 show an increase of $|S|$ with decreasing pitch. For small values of the resistivity of the depletion region this behaviour cannot be reproduced by the simulation. Here $|S|$ remains almost constant independent of the pitch size. This again shows that small changes in resistivity, e.g. by the assumption of additional surface traps, cannot solely reproduce the measured behaviour. Furthermore it shows the minor role of the geometry. By further increasing the resistivity of the depletion region the quality of the simulated trend can be improved. This is in agreement with the assumption of production process induced cracks that increase the resistivity of the edge region further. The deviation of the trends between experiment and simulation at $a = 4\,\mu m$ is not due to a high conductive depletion region, but comes from isotropic etching leading to almost the same hole size as for a nominal pitch of 8 µm.

6.4 Influence of interface regions on the thermoelectric properties

As mentionend in the introduction a major advantage of semiconductors over metals is the possibility to tune the ratio σ/κ. Furthermore, recent experimental work on ordered nanostructured semiconductors such as superlattices (e.g. GaAs/AlAs [25] or Bi_2Te_3/Sb_2Te_3 superlattices [19] or PbTe/Pb(Sn)SeTe quantum-dot superlattices [121]), but also on inhomogeneous composites consisting of a matrix material with nanometer sized inclusions (e.g. ErAs nanoparticles in $In_{0.53}Ga_{0.47}As$ [122]), clearly demonstrate that nanostructuring as well as composite formation indeed alter the thermoelectric properties such that Z may be significantly increased.

The microscopic origins of an enhancement of Z in nanostructured and composite materials are numerous and have not been fully explored yet. On the one hand, modifications of the density of states, i.e. for phonons as well as electrons, caused by the reduction of the dimensionality and corresponding confinement effects play a major role [15, 17, 123]. On the other hand, there are the effects of grain boundaries or interfaces (e.g. depletion regions or interface charges etc.) between the dissimilar materials forming a composite or nanostructured sample. Interface effects significantly alter the phonon or electron scattering within the sample [91, 124, 125]. For example, the figure of merit Z in granular materials can be optimized by variation of the grain size. This approach makes use of the different dependence of bulk and boundary scattering mechanisms for phonons and electrons on grain size [126]. As elaborated in section 6.2 energy filtering of electrons at grain boundaries may enhance the Seebeck coefficient compared to bulk material with the same free carrier concentration [118]. A mismatch of the acoustic impedances of materials forming an interface may lead to a significant thermal interface resistance [106].

A thorough understanding of the interface structure and its effects on the transport across interfaces will contribute to the optimization of the thermoelectric figure of merit. However, systematic studies of the effects of interfaces on the thermoelectric properties of a composite material can only be carried out using model systems where the number of interfaces and the interface structure can be controlled. A possible approach for achieving the necessary degree of control is to use artificial structuring methods to fabricate the model systems. ZnO is a suitable material system for fabricating such model structures. The reasons are that controlled top-down microfabrication is possible by standard semiconductor technology and that the conductivity of the ZnO semiconductor can be easily varied by orders of magnitude by Al-doping. Here, the effect of different types of interfaces between doped and undoped rf-sputtered ZnO or doped ZnO and nominally insulating ZnS on the thermoelectric properties is studied.

6.4.1 Multilayers

A series of multilayer samples consisting of alternating ZnO and ZnS layers was grown by RF sputtering on float glass substrates. The ZnO is degenerately doped with Al yielding n-type conductivity with a free carrier concentration at room temperature of about $2.0 \times 10^{20}\,\mathrm{cm}^{-3}$, as determined by Hall measurements. The ZnS layers are almost insulating. The total thickness of the layer system is about 1000 nm for the samples with 3, 5, and 7 layers corresponding to nominal thicknesses of individual ZnO layers of 250, 167, and 125 nm, respectively. In addition, a thinner sample with the same ratio of ZnO to ZnS was grown, consisting of 44 layers in total, yielding a nominal thickness of $d = 5\,\mathrm{nm}$

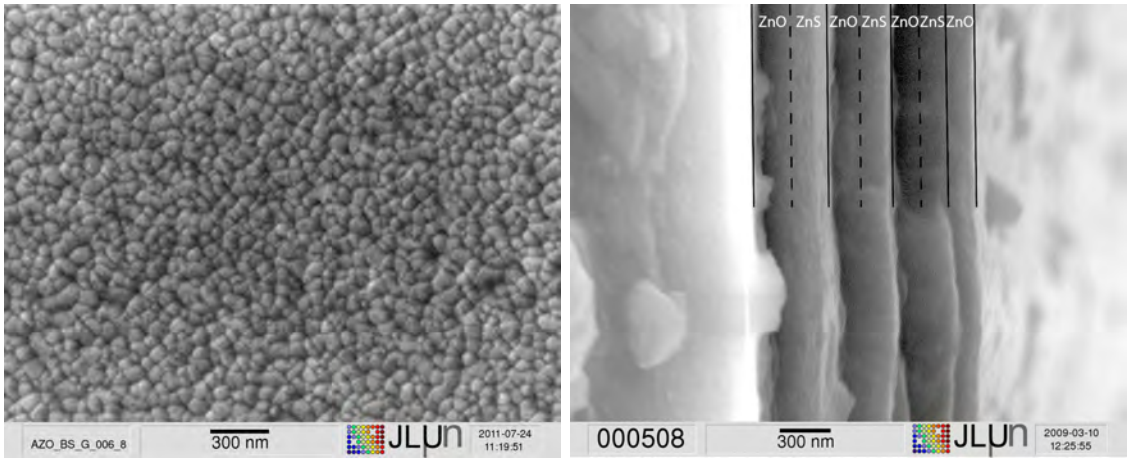

(a) Surface morphology of a sputtered ZnO:(Al) sample.

(b) Multilayer system of seven ZnO/ZnS layers.

Figure 6.15: SEM images of the surface of a sputtered ZnO/ZnS multilayer sample (a) and of the edge of the same sample (b). The positions of the interfaces between ZnO and ZnS on image (b) are indicated by thin lines.

for the individual ZnO layers. Fig. 6.15 depicts two SEM images of the surface (a) and an edge (b) of the multilayer sample with 4 ZnO layers, respectively. The positions of the layers are indicated in the image of the sample edge. The different layer periods can be clearly distinguished. The step-like edges correspond to the ZnO-ZnS interfaces. The ZnS-ZnO interfaces cannot be seen as clearly. It seems that the ZnS grows better on the ZnO than vice versa. In Fig. 6.16 a time-of-flight secondary ion mass spectroscopy (TOF-SIMS) measurement of a ZnO/ZnS multilayer sample shows that both interfaces are sharply defined and that the period of the superlattice is reproducable. The image of the surface of the sample shows an island structure with typical sizes in the range of 50 nm. The island structure is a result of the columnar growth on the glass substrate. It can be anticipated that the surface roughness observed in the SEM image is also a measure of the interface roughness of the ZnO/ZnS interfaces.

Pieces of the samples were contacted with indium for the transport measurements. Indium forms ohmic contacts with ZnO [127]. Temperature-dependent Seebeck coefficient measurements were performed as described in section 3.1 and temperature-dependent Hall and electric conductivity measurements were performed in van-der-Pauw geometry on a different piece of the same specimen (see section 3.3).

Fig. 6.17 shows the measured electric conductivities (a) and the Seebeck coefficients (b) of the four samples as functions of temperature in the range from 30 to 300 K. Clear trends can be observed. The three samples with the wider ZnO layers ($d > 100$ nm) show only a very weak temperature dependence of the conductivity, which is expected for quasi metallic samples, however, it is clearly visible that the conductivity increases with decreasing layer thickness for these samples. The conductivity of the fourth sample shows a stronger temperature dependence, i.e. exhibits more of an activated transport behaviour. Therefore, at low temperatures its conductivity is lower than those of the samples with the wider ZnO layers, but, at room temperature, its conductivity is comparable to that of the sample with the widest ZnO layers of $d = 250$ nm. The Seebeck coefficients of

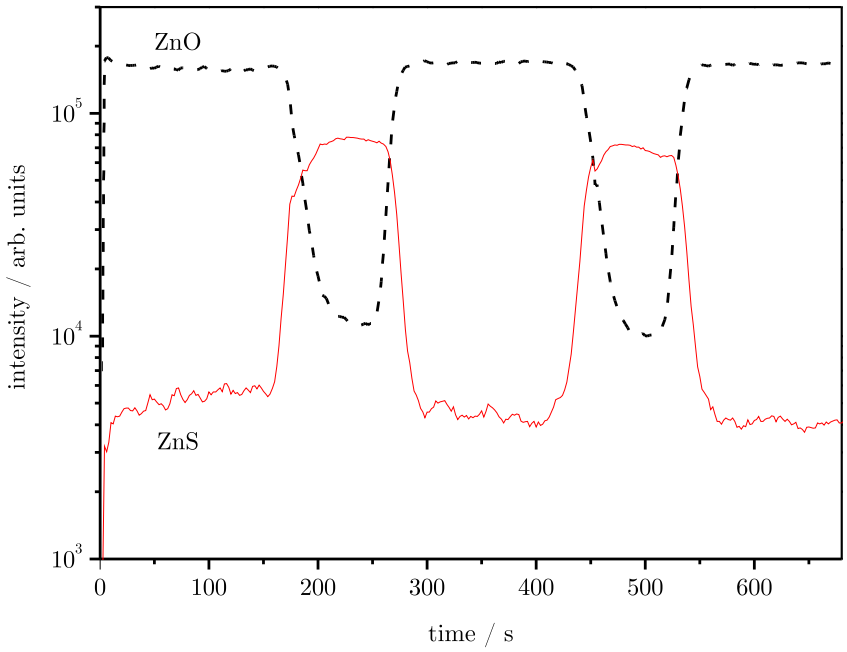

Figure 6.16: Depth profile of a ZnO/ZnS multilayer measured by TOF-SIMS.

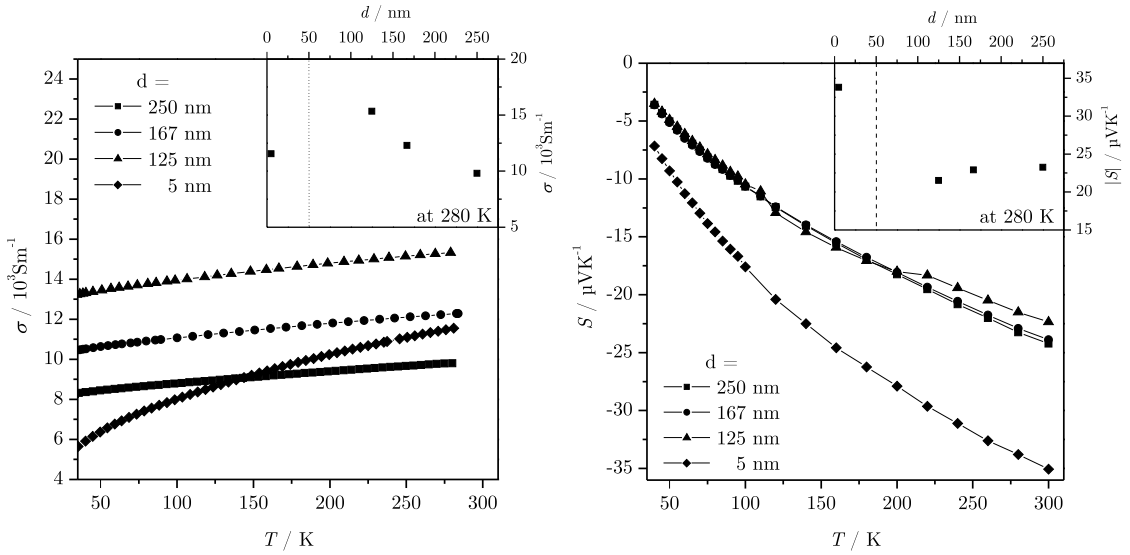

(a) Temperature dependence of the electrical conductivity.

(b) Temperature dependence of the Seebeck coefficient.

Figure 6.17: Temperature dependence of in-plane conductivity σ (a) and Seebeck coefficient S (b) for the series of ZnO/ZnS multilayer samples. The insets show plots of the two transport coefficients at 280 K as a function of the thickness d of the individual ZnO layers.

all four samples are negative as expected due to the dominance of the highly doped, n-type ZnO layers. The decrease of $|S|$ with decreasing temperature as well as values of $S \approx -25\,\mu\mathrm{V/K}$ at room temperature are typical for n-type ZnO of high doping. The results on the three samples with the wide ZnO layers ($d > 100\,\mathrm{nm}$) are very similar in magnitude and temperature behaviour, nevertheless show a continuous change with decreasing layer thickness, i.e. a decrease of $|S|$. For these three samples, this dependence of S on layer thickness d correlates with that of the corresponding σ values, i.e. lower $|S|$ means higher σ value. Against this trend, the sample with ZnO layers of $d = 5\,\mathrm{nm}$ shows a considerably larger absolute value S, despite exhibiting almost the same conductivity σ at room temperature as the samples with the wider ZnO layers. Furthermore, the temperature dependence of S is only slightly more pronounced than for the other samples. The behaviour of S and σ as a function of ZnO layer thickness is summarized in the two insets of the main graphs of Fig. 6.17. In the following it will be demonstrated that the observed behaviour arises due to two different effects, the formation of interface layers of higher conductivity between ZnO and ZnS (dominant at large d) on the one hand and interface roughness effects (dominant at small d) on the other hand.

For the modelling of the thermoelectric properties the network-model *NeMo* for simulating the electric and thermal properties of the multilayer system has been used. The network model for calculating the Seebeck coefficient in a parallel configuration for a system of two ideal layers of different properties, which are used in the following for analysing the dependence of σ and S on d for the three samples with the wide ZnO layers, is very simple. It can be represented by a parallel circuit of two voltage sources each with a series resistance. Since the applied temperature difference across both layers is the same, the voltages in the two layers are proportional to the corresponding Seebeck coefficients. Finally the total Seebeck coefficient is proportional to the total voltage. To derive the total voltage, one has to first calculate the current flow through the parallel circuit:

$$I = \frac{U_1 - U_2}{R_1 + R_2}. \tag{6.3}$$

The voltages across both branches must be the same and equal to the total voltage between the contacts:

$$U = U_1 + \frac{U_2 - U_1}{R_1 + R_2} \cdot R_1 = U_2 + \frac{U_1 - U_2}{R_1 + R_2} \cdot R_2. \tag{6.4}$$

Now the total Seebeck coefficient depending on the electric conductances L_1 and L_2 of the two layers can be written as:

$$S = \frac{U}{\Delta T} = \frac{L_1}{L_1 + L_2} \cdot S_1 + \frac{L_2}{L_1 + L_2} \cdot S_2. \tag{6.5}$$

The expression for the corresponding total electric conductance L is rather trivial for this system:

$$L = L_1 + L_2. \tag{6.6}$$

Going back to the dependence of the conductivity and the Seebeck coefficients depicted in the insets of the two graphs of figure 6.17, the increase of the conductivity (in conjunction with the decrease of the Seebeck coefficient) with decreasing layer thickness d needs to be explained. In the parallel transport configuration, the insulating ZnS layers (which basically have conductance $L_{\mathrm{ZnS}} = 0$) need to be considered neither in case of electric transport (Eq. (6.6)) nor in case of the Seebeck effect (Eq. (6.5)). However, it may be

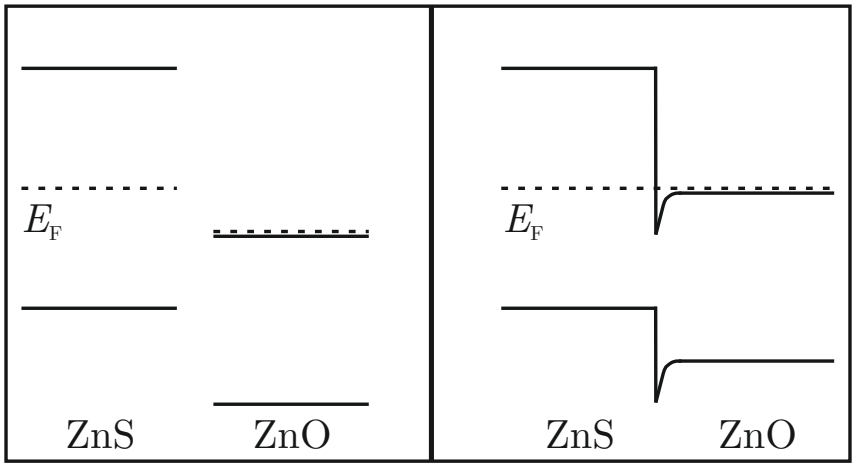

Figure 6.18: Scheme of the band alignment between insulating ZnS and n-type ZnO.

anticipated from the band alignment between insulating ZnS and n-type ZnO depicted in figure 6.18, that, in addition to the transport channel through the bulk of the wide ZnO layers, a second parallel transport channel of higher conductivity arises at interfaces due to the band bending which leads to an accumulation of electrons. This assumption is further corroborated by the analysis of both data sets in the two main graphs of figure 6.19 which show plots of σ and S versus d^{-1}. The analysis is based on the following considerations. Assuming an interface region of width $\delta < d/2$ on either side of the wide ZnO layers, where δ is the same for all $d > 100\,\mathrm{nm}$. Replacing the conductances L by conductivities σ and taking into account the sample geometry, one obtains from Eq. (6.6) for the electrical conductivity σ:

$$\sigma = 2\delta(\sigma_{\mathrm{int}} - \sigma_{\mathrm{bulk}})\frac{1}{d} + \sigma_{\mathrm{bulk}} \approx 2\delta\sigma_{\mathrm{int}}\frac{1}{d} + \sigma_{\mathrm{bulk}} \tag{6.7}$$

and from Eq. (6.5) for the product σS:

$$\sigma S = 2\delta(\sigma_{\mathrm{int}}S_{\mathrm{int}} - \sigma_{\mathrm{bulk}}S_{\mathrm{bulk}})\frac{1}{d} + \sigma_{\mathrm{bulk}}S_{\mathrm{bulk}} \approx 2\delta\sigma_{\mathrm{int}}S_{\mathrm{int}}\frac{1}{d} + \sigma_{\mathrm{bulk}}S_{\mathrm{bulk}} \tag{6.8}$$

where the approximations, which are used in the following, hold for $\delta << d$. The subscripts 'int' and 'bulk' denote quantities of the interface region and bulk region of the ZnO layer, respectively. The equations are used to fit the experimental data for σ vs d^{-1} and σS vs d^{-1} in the two graphs of figure 6.19. The intersections of the fits with the ordinante axes yield values of $S_{\mathrm{bulk}} = -32\,\mu\mathrm{V/K}$ and $\sigma_{\mathrm{bulk}} = 4200\,\mathrm{S/m}$. The ratio of the slopes yields $S_{\mathrm{int}} = -14\,\mu\mathrm{V/K}$. Finally, assuming $\delta = 10\,\mathrm{nm}$, one obtains $\sigma_{\mathrm{int}} = 70000\,\mathrm{S/m}$. The quality of the fit and the reasonability of the derived values for the transport coefficients support the model despite the few data points considered.

At smaller d, where d becomes comparable to the typical fluctuation length of the interface roughness between insulating ZnS and n-type ZnO and where d becomes close to 2δ, the effect of the surface fluctuations on the transport path will become dominant. This can be understood from the results of *NeMo* calculations of the σ and corresponding S in a parallel transport configuration for different d depicted in figure 6.20. Three examples of the pixel distributions forming the basis of the *NeMo* calculations are depicted as insets of the figure. Each pixel array consists of 110×110 pixels. As in the multilayer samples used in the experiment, the ratio of the total thicknesses of ZnO and ZnS is

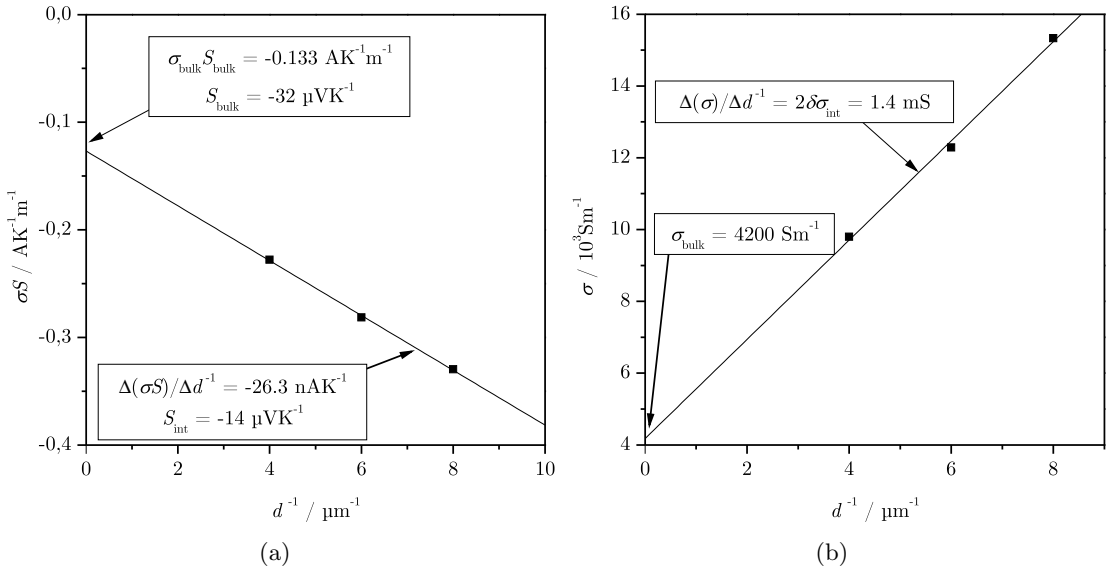

Figure 6.19: Analysis of plots of the conductivity σ (b) and the product of conductivity and Seebeck coefficient σS (a) at 280 K versus reciprocal layer thickness d^{-1} of the ZnO accounting for two transport channels, the first in the bulk of the ZnO layer and the second in interface regions of width δ. The inset shows how the band bending in the interface regions occurs when one Fermi level is established for the entire structure.

kept constant, however, for each layer width d the same roughness of the interface was assumed. For simplicity, it was assumed that thermal resistivity, electric resistivity as well as Seebeck coefficient of ZnS (black pixels) are a thousand times larger than the corresponding quantities of ZnO (white pixels) and that δ is zero, i.e. all ZnO cells have the same properties. The calculated dependence of conductivity σ and Seebeck coefficient S agree with the experimental observations, i.e. a drop of σ and an increase of $|S|$ for small d. Both can be explained by percolation effects which lead to longer transport paths for smaller d and finally force the transport through ZnS pixels when there is no longer a percolation path of ZnO pixels between the contacts.

6.4.2 Lateral structures

A series of bar-shaped samples consisting of lateral arrangements of alternating ZnO:Al and ZnO stripes was fabricated by rf-sputtering and microfabrication techniques on glass substrates. Throughout the series the number of interfaces between ZnO and ZnO:Al was varied whilst the material fractions within the stripe structures were not altered. Each bar is prepared between two ZnO:Al contacts, all stripes of ZnO and ZnO:Al in a bar are of the same width, and the numbers of stripes of the two materials are equal. Thus, the number of ZnO/ZnO:Al interfaces in a sample is the same as the number of stripes. The series consists of four samples with 2, 4, 8, and 16 stripes, respectively, corresponding to stripe widths of 4 mm, 2 mm, 1 mm, and 500 µm.

Samples consisting of a ZnO:Al layer of about 500 nm thickness deposited by rf-sputtering on float glass serve as the starting point of the bar fabrication. The Al donor doping of 2% yields a degenerate n-type material with a free carrier concentration at room

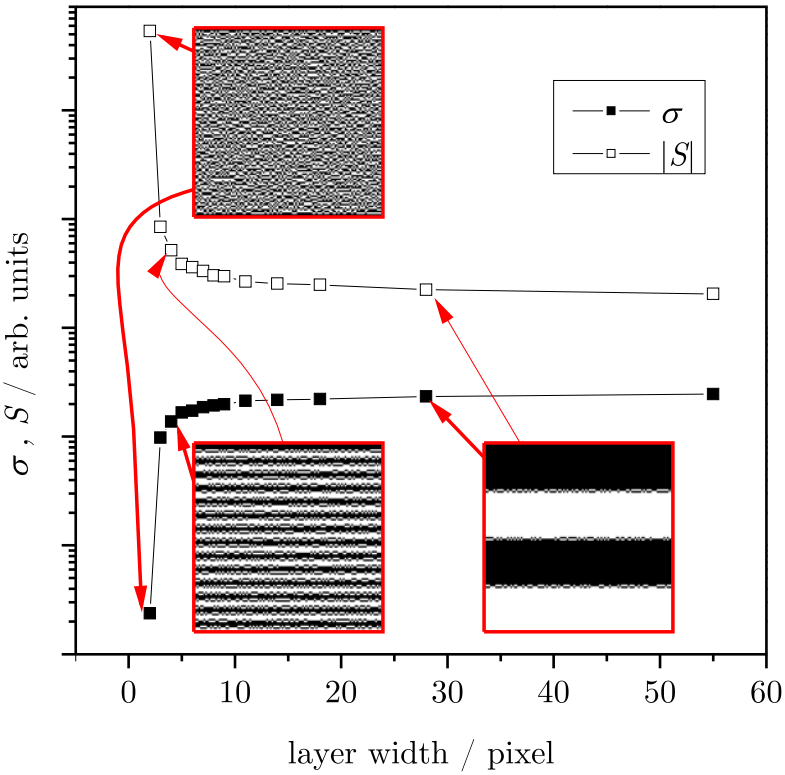

Figure 6.20: Qualitative analysis using the network model of the evolution of the transport coefficients σ and S as a function of layer width d for a multilayer sytem consisting of an insulating and a conducting material in the presence of interface roughness. The images show typical pixel arrays representing the layer system used in the calculation.

temperature of about $1.0 \times 10^{20}\,\mathrm{cm}^{-3}$. As second material undoped ZnO with a much smaller electrical conductivity and a thickness of about 300 nm was deposited onto the structured sample. To produce a pattern of alternating ZnO:Al/ZnO stripes the procedure of the self-aligned pattern transfer process was used which is described in section 4.1. The exact preparation parameters for the sample series can be found in section 4.3 under the subitem ***interfaces with point-wise contacts***. The boundary between stripes shown in the scanning-electron microscopic image in figure 6.21(a) exhibits both wall-like overlaps and moat-like cavities due to shading by the resist mask in the second sputter process. Furthermore, the optical microscope image in figure 6.21(b) reveals a roughness of the interface of about 80 µm which is fabrication induced and corresponds to the spatial resolution of the printed photomask. It is possible to reduce this roughness by using an electron-beam written photomask as shown by the samples presented in section 6.4.4. Nevertheless, a good contact between the two ZnO materials is obtained in the lower regions of the sample.

The stripes of the samples were studied by different methods, e.g. Raman and photoluminescence (PL) spectroscopy. Both measurements were carried out at room temperature using a 325 nm HeCd laser for excitation. Figure 6.22(a) shows the results of the PL measurements of the reference samples and of two of the structured samples. All PL spectra consist of a broad band. The series of sharp features on top of the PL bands are due to res-

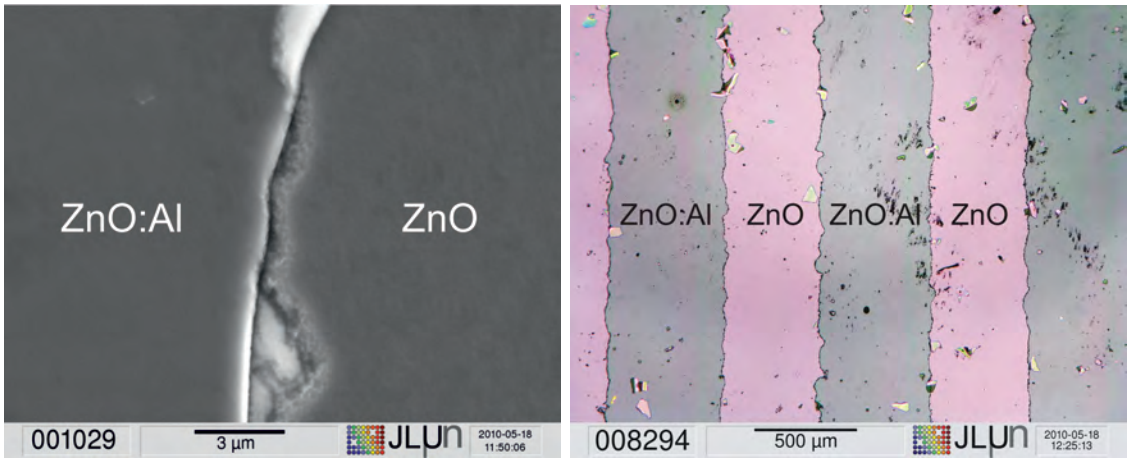

(a) (b)

Figure 6.21: (a) Scanning electron microscopic image of a ZnO/ZnO:Al interface. (b) Optical microscopic image of the ZnO/ZnO:Al alternating stripes with stripe width 500 µm.

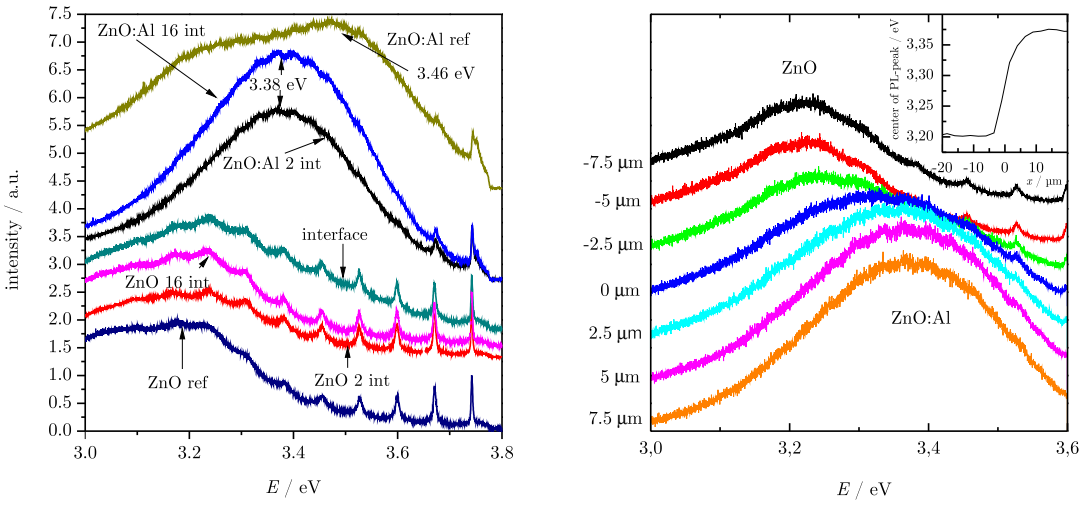

(a) (b)

Figure 6.22: (a) Room-temperature photoluminescence spectra of the ZnO and ZnO:Al references and the alternating stripe samples with 2 and 16 interfaces. (b) PL scan across a ZnO/ZnO:Al interface. Every 2.5 µm a PL spectrum was acquired. The shift of the peak position in the vicinity of the interface becomes clear in the inset.

onant multi-LO-phonon Raman scattering which arises due to the strong electron-phonon coupling in ZnO [128]. The PL spectrum of the ZnO:Al reference is shifted to higher energies than that of the undoped ZnO reference (ref) sample. In particular, it peaks at higher energies than the bandgap of undoped ZnO of 3.37 eV at room temperature. The reason is the so called Burstein-Moss shift which occurs for degenerately n-doped samples due to

conduction band state filling above the metal-insulator transition. The latter occurs at about $4 \times 10^{19}\,\mathrm{cm}^{-3}$ in n-type ZnO. Above this critical doping concentration, the optical band gap increases with $n^{2/3}$ where n is the doping concentration [129]. In addition to the two spectra of the reference samples, spectra of the samples with 16 and 2 interfaces (int), respectively, are shown in the figure. For each of the microstructured samples, two spectra were taken, one at the center of an undoped ZnO stripe and one at the center of a ZnO:Al stripe. The peaks of both spectra taken of the ZnO:Al stripes are shifted to lower energy with respect to the spectrum of the ZnO:Al reference indicating that the carrier concentration in the ZnO:Al stripes is reduced. The shift of the PL corresponds to a reduction of the carrier concentration by about half an order of magnitude. Furthermore, the PL spectra of the undoped ZnO stripes are slightly shifted to higher energies. However, it is not clear whether this shift arises due to increasing carrier concentration, as the carrier concentration in this layer should be still well below that of the metal-insulator transition. The PL spectrum obtained of the boundary region between a ZnO and a ZnO:Al stripe is somewhat of intermediate character. Thus, the PL spectroscopic results give a hint that diffusion of Al could take place in the alternating ZnO:Al/ZnO stripe structures.

To take a closer look at the interface region, the spatial resolution needs to be increased. For this the sample with 8 interfaces was mounted on a x-y-z micrometer stage which has an accuracy of 100 nm for positioning. Now the PL spectra were mapped across the interface in steps of 2.5 µm. The results are shown in figure 6.22(b). Coming from the undoped ZnO one can clearly see the shift of the center of the PL-peak from about 3.2 eV to about 3.4 eV. To obtain an estimate of the dimension of the interface region, the center of the PL-peak is plotted against the distance from the interface in the inset of figure 6.22(b). Here one can see, that the energy-shift of the center of the PL-peak is not changing abruptly at the physical interface between ZnO and ZnO:Al, but the change of position is smeared out when crossing the interface. This means that the Al concentration starts to rise already a few microns before the nominal interface position on the ZnO side and is only at its maximum value several micrometers behind it on the ZnO:Al side. The dimension of this transition region can be determined to be about 20 µm. These findings are further corroborated by the Raman spectra shown in Figure 6.23. On the left side of the figure the Raman spectra of the longitudinal-optical (LO) phonon region of ZnO obtained of the two reference samples differ significantly. The undoped reference sample shows a Lorentzian-like sharp LO phonon signal typical for non-degenerate ZnO, whereas the ZnO:Al reference exhibits an additional broad peak at lower Raman shifts which can be assigned to the L_--mode of the coupled phonon-plasmon which occurs at high doping concentrations [130]. The LO phonon feature in this spectrum arises from the depleted regions of the ZnO:Al close to the surface. Again, the spectra of the ZnO:Al stripes of the ZnO:Al/ZnO bar structures show an intermediate behaviour. The L_--feature is less pronounced as expected for a slightly lower free-carrier concentration n. The LO feature in the spectra of the undoped ZnO stripes is very similar to the corresponding reference sample, however, again no strong dependence of this signal on carrier concentration n is expected below the metal-insulator transition.

Again the interface region was mapped with higher accuracy. This is shown in figure 6.23 (b), where in 2.5 µm intervals Raman spectra were taken. Here the ratio of the characteristic L_--mode of the Al doped ZnO compared to the LO phonon signal typical for non-degenerate ZnO is a measure for the Al concentration. This can be seen in the inset of figure 6.23(b). Similar to the inset of figure 6.22(b) the ratio P1/P2 is increasing constantly within a region of 7.5 µm around $x = 0$, denoting the nominal interface po-

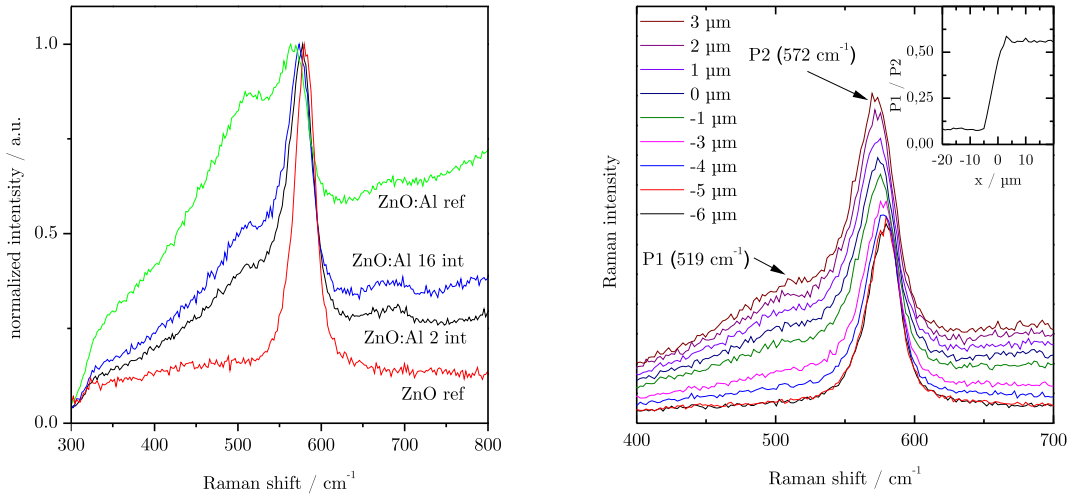

Figure 6.23: (a) Room-temperature Raman spectra of the longitudinal-optical phonon region for the reference samples and the alternating stripe samples with 2 and 16 interfaces. (b) Raman scan across a ZnO/ZnO:Al interface. In certain intervals (every 1-2 µm) a Raman spectrum was measured. The ratio of the broad peak at lower Raman shifts (P1) to the Lorentzian-like sharp LO phonon signal (P2) is plotted against the position on the sample surface with respect to the interface ($x = 0$) in the inset. All spectra were taken with 325 nm excitation.

sition. So the transition is not abrupt. So far, the optical spectroscopic results indicate a diffusion process from Al into the undoped ZnO layers of the alternating ZnO:Al/ZnO microstructures. On the other hand the roughness of the interface, induced by the preparation process of this series (printed mask) is of the same order of magnitude. To be able to distinguish between these two effects, further measurements were performed.

For the macroscopic thermoelectric measurements, the samples were contacted by placing small pieces of indium on top of the ZnO:Al contact pads on either side of the bar structure and afterwards heating the sample in an oven at 400 °C for 10 min in order to diffuse the indium into the contact areas. To avoid reactions with oxygen the procedure was performed in an Ar atmosphere. The contacts obtained show ohmic behaviour. Thermocouples consisting of CuNi/NiCr were soldered into the In contacts for Seebeck and resistivity measurements. The experimental set-up for the thermopower measurements in the temperature range from 50 to 300 K is described in detail in section 3.1.

The results of temperature-dependent measurements of the Seebeck coefficient S and of the resistivity ρ for the entire series of samples are depicted in figure 6.24(a) and (b), respectively. The undoped ZnO reference possesses the highest resistivity and thus also the highest value of the Seebeck coefficient. The temperature dependence of S and ρ are characteristic for a semiconducting sample. The resistivity increases with decreasing temperature and the Seebeck coefficient shows the characteristic phonon drag at low temperatures. On the other hand, the ZnO:Al reference sample shows the lowest resistivity

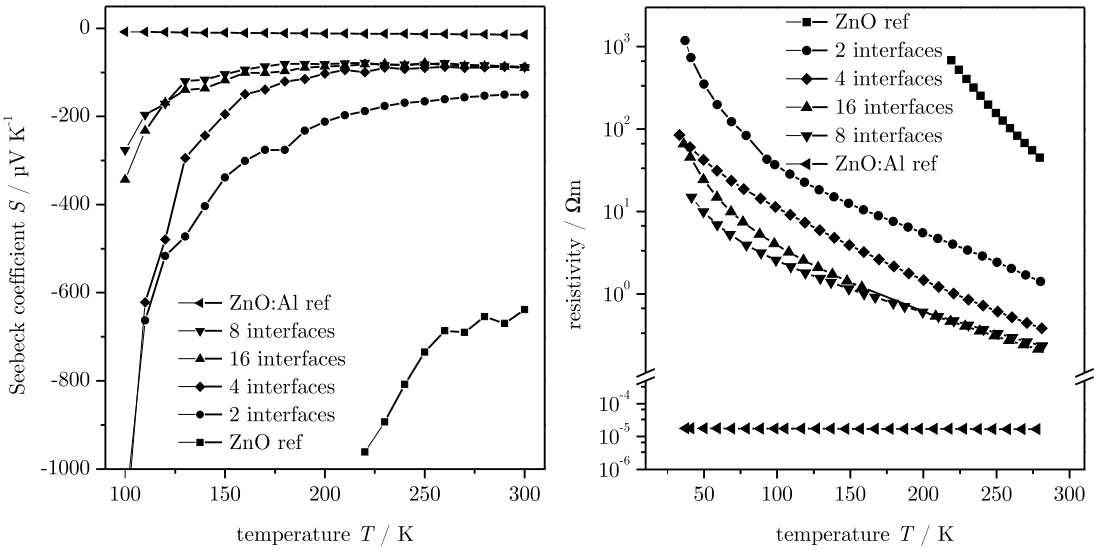

Figure 6.24: (a) Temperature dependence of the Seebeck coefficient of the sample series with increasing number of interfaces. (b) Temperature dependence of the resistivity of the same sample series.

and hence the lowest absolute values of S. Seebeck coefficient as well as resistivity show a weak temperature dependence only as expected in the regime of metallic doping. The series of microstructured bars of ZnO:Al/ZnO stripes shows an intermediate behaviour, both, in terms of the Seebeck effect and the electric resistivity. This is somewhat anticipated considering that all four microstructured samples consist of equal fractions of undoped ZnO and ZnO:Al. In addition, a clear trend is observed throughout the series, the resistivity at all temperatures decreases with decreasing stripe thickness, i.e. increasing number of interfaces. Similarly the absolute value of the Seebeck coefficient S at constant temperature decreases with increasing number of interfaces. This holds in both cases for 2, 4, and 8 interfaces. The results for 16 interfaces are very similar to those with 8 interfaces. If the interface regions played no role in the thermoelectric transport processes, the transport coefficients of all ZnO/ZnO:Al stripe structures would have to be the same, because all four structures of alternating stripes consist of the same amounts of ZnO and ZnO:Al. Thus, the trends in S and ρ for the series are clear proof that the interface regions are of importance for the transport. Moreover, the lowering of the resistivity of the microstructured samples with increasing number of interfaces is in agreement with the assumptions that Al donors diffuse into the undoped regions as well as that the interface between doped and undoped regions is very rough.

The findings are further supported by simulations of the dependence of S and ρ at room temperature on stripe width based on the network model introduced in section 5.3. Further details of this model can as well be found in [131, 132]. To model the diffusion profile of the Al donors, it was assumed that the Al content n in a pixel positioned at x close to an interface centered at x_0 is given by a Fermi-like distribution characterized by a diffusion width v:

$$n(x) = \frac{n_0}{\exp\left(\frac{x-x_0}{v}\right) + 1}. \tag{6.9}$$

Here, $x < x_0$ lies within the nominal ZnO:Al layer and $x > x_0$ in the nominal ZnO layer and n_0 is the nominal Al-content in the ZnO:Al layer. Adding the Al distributions due to diffusion for all interfaces yields Al-profiles for the entire bar structure as plotted in the inset of figure 6.25(b) for different values of the diffusion width v. One can see that these profiles are very similar to the integrated interface scan of the electrical conductivity shown in figure 6.26(a). Here the profile is caused by the interface roughness. For simplicity, it was assumed in the simulations that the Seebeck coefficient S and the electrical conductivity $\sigma = \rho^{-1}$ can be linearly interpolated between the values of the two reference samples. The values are $S = -650\,\mu\mathrm{VK}^{-1}$ for the undoped ZnO reference and $S = -14\,\mu\mathrm{VK}^{-1}$ for the ZnO:Al sample. The corresponding conductivity values are $(45\,\Omega\mathrm{m})^{-1}$ and $(1.7\,\Omega\mathrm{m})^{-1}$, respectively. For simplicity, equal values for the thermal conductivities for both materials were used as no experimental results were available. The left graphs of figure 6.25 show the evolution of the experimental values of S and ρ at room temperature as a function of stripe width. The right graphs show corresponding results calculated as described above for different diffusion width v. The observed trends can be qualitatively reproduced. It can be seen that for ideal interfaces (i.e. $v = 0$) the theoretical values of the resistivity and the Seebeck coefficient are, as expected, independent of stripe width and that in case of Al diffusion (i.e. $v > 0$) the observed trends for S and ρ are the same in experiment and theory. The v of 2 pixels at a stripe width of 50 pixels roughly corresponds to 160 µm interface region at 4 mm stripes. As will be discussed later the measured interface roughness is, with 80 µm in the same regime. If diffusion takes place the width of the diffusion region indicates that the Al diffusion takes place along the grain boundaries of the sputtered samples.

On the other hand, as mentioned earlier in this section, the interface roughness of these samples is in the same order of magnitude ($\approx 80\,\mu\mathrm{m}$). This results in an "interface area" of the same width where the position of the interface cannot be clearly determined. This can be seen in figure 6.26(a) where the local electrical conductivity as a function of space is plotted. If only one single scan is considered a nice sharp step between the conductivities of Al doped and undoped ZnO is observed (dotted line). This changes if one integrates over 50 single scans. Now the defined changeover is smoothed out and, similar to the optical measurements, it becomes impossible to tell where exactly the interface is located. The insets of both figures 6.26(a) and (b) nicely give an impression of the interface roughness. Furthermore measurements of the local electron affininty (figure 6.26(b)) reveal another effect that stems from the production process. The so-called "garden fences" at the interfaces, resulting from material deposited on the resist sidewalls due to an imperfect lift-off, make it almost impossible to precisely locate the actual interface position. With decreasing bar width the interface roughness becomes more important, because the fraction of the "interface area" compared to the total bar area increases. So the actual distance between two highly conducting ZnO:Al bars decreases as well. This might also explain the observed behaviour of the global electrical conductivity and Seebeck coefficient.

Even in alternating ZnO/ZnO:Al structures, which consist of the same host material ZnO, a dependence of the thermoelectric properties on the number of interfaces, i.e. on the interface structure, at constant material fractions is observed. Raman, photoluminescence, and the thermoelectric properties indicate that the observed dependence on the number of interfaces arises either from interface roughness or from diffusion of the Al-donors from the ZnO:Al stripes into the adjacent undoped ZnO stripes. Calculations based on a network model assuming a Fermi-like diffusion profile corroborate these findings and suggest that the region affected by the diffusion is of a width of the order of 100 µm. The activation

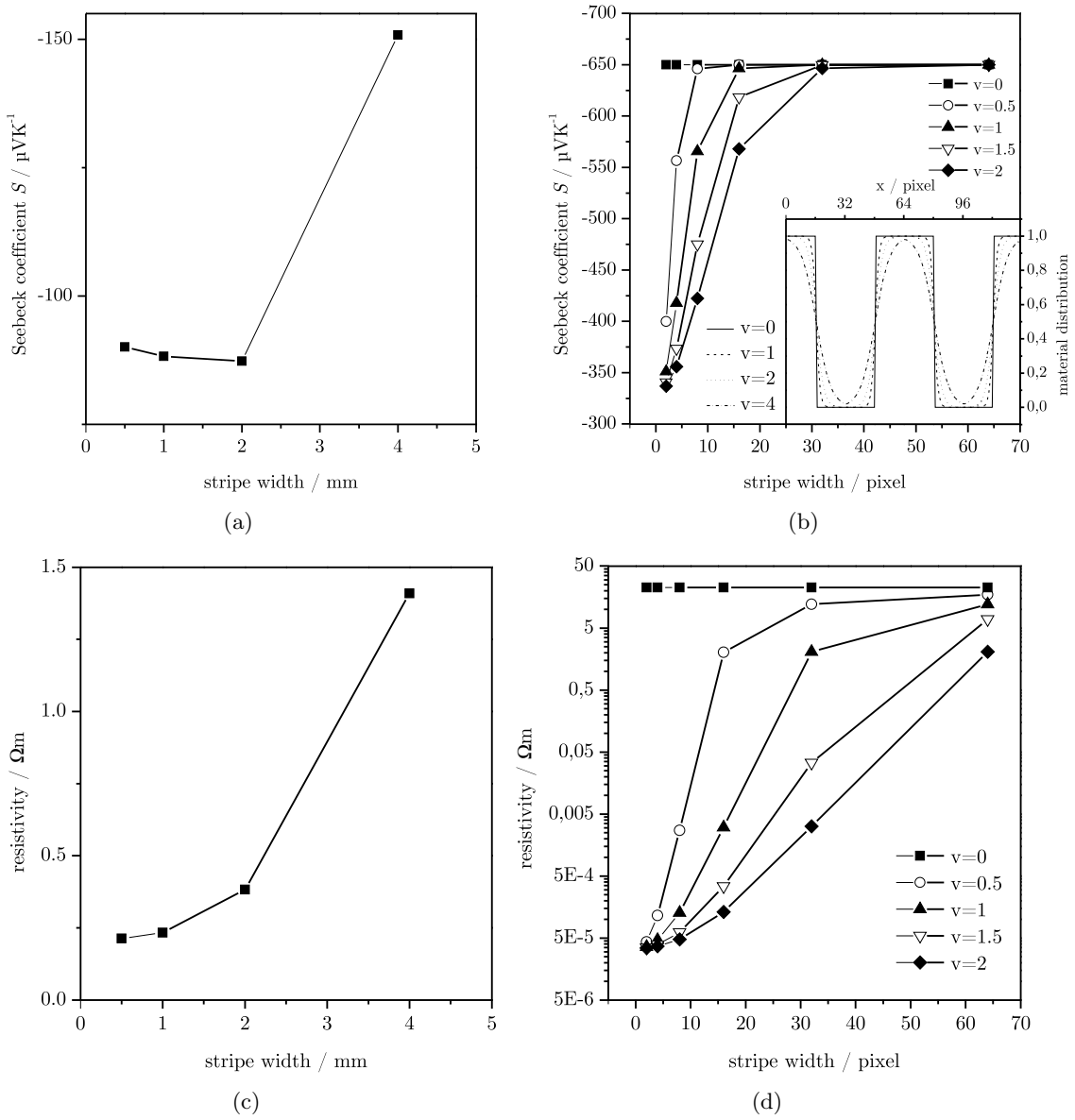

Figure 6.25: Comparison of experimental [left, graphs (a) and (c)] and theoretical [right, graphs (b) and (d)] results for the dependence of the Seebeck coefficient [top, graphs (a) and (b)] and the resistivity [bottom, graphs (c) and (d)] at room temperature as a function of stripe width. The inset shows the diffusion profiles assumed in the calculation arising for different diffusion widths v.

energy of Al-diffusion in bulk crystalline ZnO is 2.74 eV, therefore, the diffusion process is likely to occur along the grain boundaries in these sputtered samples. So far measurements with local probes showed that a lot of interesting effects take place at interfaces that dominate the overall behaviour of the sample. However, further experiments with a higher spatial resolution are required in particular measurements of the in-plane thermal conductivity to be able to distinguish between the two effects of interface roughness and diffusion and hence to obtain a quantitative agreement.

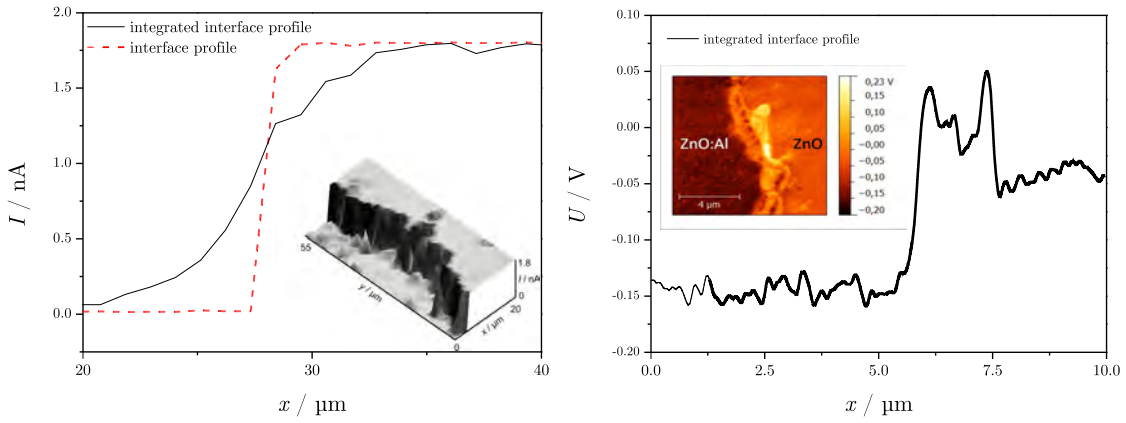

Figure 6.26: (a) Scan of the local electrical conductivity across an interface of a sputtered ZnO/ZnO:Al sample. The red dotted line is one single scan while the black line is the integration over 50 single profiles. (b) Integrated profile across a sputtered ZnO/ZnO:Al interface of the electron affinity. The inset shows the same interface of the Kelvin probe mapping. Both scans were taken with the same AFM however in two different measurement modes (I-Probe and Kelvin-Probe mode).

6.4.3 Scanning probe analysis of the diffusion profile

To clarify whether the Seebeck coefficients of the original sputtered materials changed due to diffusion and roughness effects, measurements of the local Seebeck coefficients at room temperature were performed at DLR Cologne. The local Seebeck measurements were carried out with a microprobe Seebeck measurement technique described in section 3.2.

In figure 6.27 the local Seebeck coefficients of the sample with 500 µm bar-width are shown. One observes steep gradients at the material interfaces and flat plateaus within the material especially in the case of ZnO:Al. The absolute values of the Seebeck coefficient differ from those measured for the respective bulk references. In the case of ZnO:Al the values decrease from -14 µV/K to approximately -25 µV/K while for the undoped ZnO these values increase drastically from -638 µV/K to approximately −100 µV/K. The mean values of the locally measured Seebeck coefficients of the ZnO:Al bars and the ZnO bars of all four samples as well as the reference values are plotted in Fig. 6.28. It seems that the local Seebeck coefficients are independent of the bar-width, since no big deviations occur. If diffusion of aluminum donors from the doped ZnO:Al to the undoped ZnO across the interfaces is assumed, then the interface region itself seems to act as a diffusion barrier slowing the diffusion process down whereas inside the material stripes a fast diffusion occurred. The diffusion barrier and the resulting slow diffusion across the interface can be related to the point-like contacts between ZnO:Al and ZnO at the interfaces while the fast diffusion inside the material is probably due to diffusion paths along grain boundaries.

To estimate the magnitude of the changes of the carrier concentration in the structured samples one may assume Seebeck coefficient $S \propto 1/n$ with n being the carrier concentration distinguishing between the concentration ranges above and below the metal-insulator transition. The Seebeck coefficients of ZnO:Al sputtered samples from Fig. 6.1 have been plotted against the reciprocal values of the known carrier concentrations in fig. 6.29. A

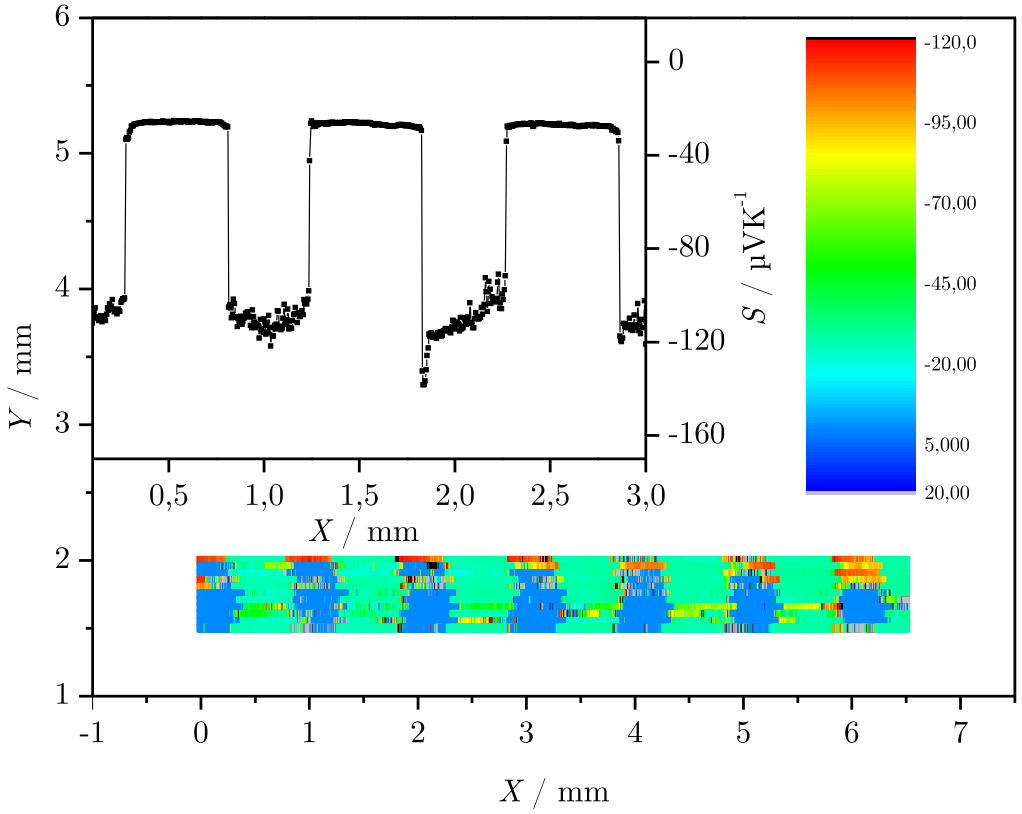

Figure 6.27: Local measurement of the Seebeck coefficient obtained with the microprobe Seebeck technique on a sample with a bar width of 0.5 mm. The two materials can be clearly distinguished: The Al doped ZnO has lower absolute values due to a higher carrier density.

linear fit of the data for both, the metallic and the insulating regimes, was used to estimate the carrier concentrations of the ZnO and the ZnO:Al bars. Both fits should cross at the metal-insulator transition which occurs here for ZnO:Al at about $3.5 \cdot 10^{19}\,\mathrm{cm}^{-3}$. This is in good agreement with the literature values for ZnO found by Özgür et al. [127]. The estimated carrier concentrations for the bar-materials for each sample can be found in table 6.1. As can be seen in the table the sums of the estimated carrier concentrations are roughly constant confirming the assumptions made above about the carrier diffusion.

Using the extracted data set of local Seebeck coefficients and carrier concentrations one can now try to model the global Seebeck coefficients of samples which were already shown in figure 6.24. As a first, very simple estimate, it was assumed that the thermal gradient is constant across the sample's sapphire substrate. As the area ratio of both types of bars is equal, the global Seebeck coefficient is then given by:

$$S_{\mathrm{global}}^{\mathrm{model1}} = \frac{S_{\mathrm{ZnO:Al}} + S_{\mathrm{ZnO}}}{2}. \tag{6.10}$$

The calculated values for all samples are shown in table 6.1. The values obtained are larger than the measured ones. The second estimate makes the assumption that the thermal gradient across the sample is determined by the thermal conductivities of the stripes of the thin-film only. The temperature drop along the sample is the sum of the two

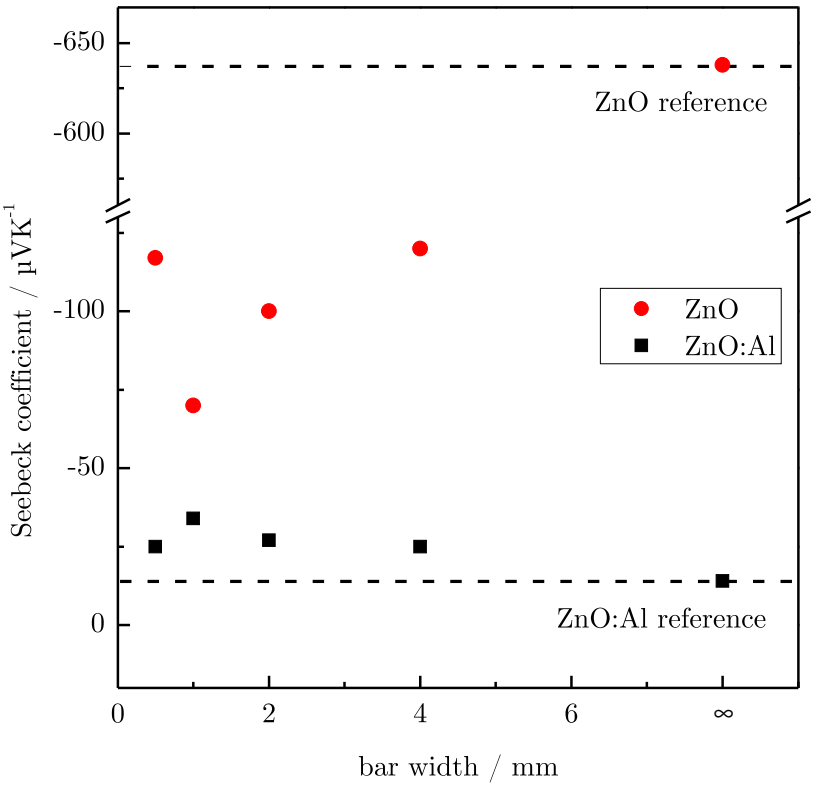

Figure 6.28: Local Seebeck coefficients plotted against the bar width for the entire series of samples and the respective references. The local values show no clear dependence on the width of the stripes.

bar width mm	$n_{\mathrm{ZnO:Al}}$ cm^{-3}	n_{ZnO} cm^{-3}	n_{global} cm^{-3}	$S^{\mathrm{exp}}_{\mathrm{global}}$ $\mu\mathrm{VK}^{-1}$	$S^{\mathrm{model1}}_{\mathrm{global}}$ $\mu\mathrm{VK}^{-1}$	$S^{\mathrm{model2}}_{\mathrm{global}}$ $\mu\mathrm{VK}^{-1}$
0.5	$1.48 \cdot 10^{20}$	$4.98 \cdot 10^{19}$	$1.98 \cdot 10^{20}$	-90	-71	-94
1	$1.24 \cdot 10^{20}$	$7.53 \cdot 10^{19}$	$2.00 \cdot 10^{20}$	-88	-52	-57
2	$1.42 \cdot 10^{20}$	$5.67 \cdot 10^{19}$	$1.99 \cdot 10^{20}$	-87	-64	-80
4	$1.48 \cdot 10^{20}$	$4.87 \cdot 10^{19}$	$1.97 \cdot 10^{20}$	-151	-73	-97

Table 6.1: Summary of the carrier concentrations and the Seebeck coefficients of the four different samples. The local carrier conentrations are interpolated using the fits shown in figure 6.29. The global Seebeck coefficients are calculated by two different models and compared to the global experimental values.

temperature drops along each material $\Delta T_{\mathrm{global}} = \Delta T_{\mathrm{ZnO:Al}} + \Delta T_{\mathrm{ZnO}}$. The temperature difference along all bars of the same material $\Delta T_{\mathrm{ZnO:Al}}$ and ΔT_{ZnO} corresponds to its thermal resistance $\lambda_{\mathrm{ZnO:Al}}$ and λ_{ZnO}, respectively, and the sum of the two resistances $\lambda_{\mathrm{global}} = \lambda_{\mathrm{ZnO:Al}} + \lambda_{\mathrm{ZnO}}$. The temperature drop along the ZnO:Al bars is then given by $\Delta T_{\mathrm{ZnO:Al}} = \lambda_{\mathrm{ZnO:Al}} \cdot \frac{\Delta T_{\mathrm{global}}}{\lambda_{\mathrm{global}}}$. The calculation for ΔT_{ZnO} is analogous. Hence the global Seebeck voltage can be written as the series connection of the bars consisting of the two

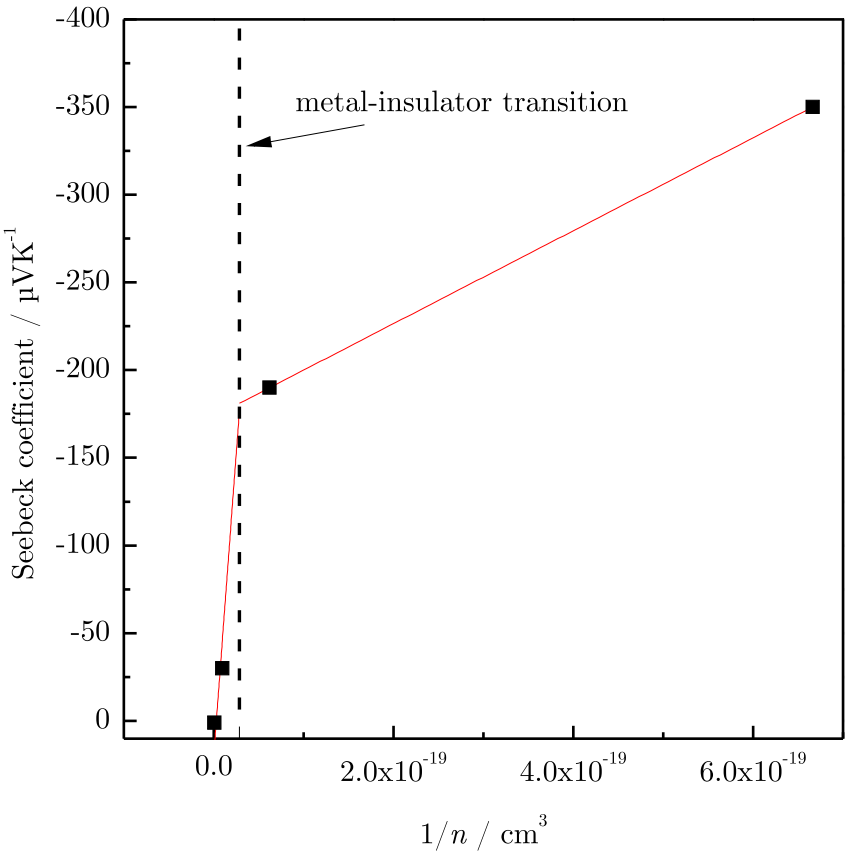

Figure 6.29: Dependence of the Seebeck coefficient on the inverse carrier concentration. The data (black squares) was taken from Fig. 6.1 and the red lines are linear fits. The linear fits cross at $3.5 \cdot 10^{19}\,\mathrm{cm}^{-3}$ which agrees well with the Mott-transition of ZnO.

materials:

$$V_{\mathrm{global}} = S_{\mathrm{ZnO:Al}} \cdot \Delta T_{\mathrm{ZnO:Al}} + S_{\mathrm{ZnO}} \cdot \Delta T_{\mathrm{ZnO}}. \tag{6.11}$$

With the definition of the Seebeck coefficient and the assumptions from above the global Seebeck coefficient can be calculated as:

$$S_{\mathrm{global}}^{\mathrm{model2}} = \frac{S_{\mathrm{ZnO:Al}} \cdot \lambda_{\mathrm{ZnO:Al}} + S_{\mathrm{ZnO}} \cdot \lambda_{\mathrm{ZnO}}}{\lambda_{\mathrm{global}}}. \tag{6.12}$$

If a proportionality of λ to the reciprocal value of the carrier concentration n is assumed, one obtains:

$$S_{\mathrm{global}}^{\mathrm{model2}} = \frac{(S_{\mathrm{ZnO:Al}} \cdot n_{\mathrm{ZnO}} + S_{\mathrm{ZnO}} \cdot n_{\mathrm{ZnO:Al}})}{n_{\mathrm{ZnO:Al}} + n_{\mathrm{ZnO}}}. \tag{6.13}$$

Calculating the global Seebeck coefficients with equation (6.13) leads to the values given in the last column of table 6.1. Again the values of the absolute Seebeck coefficients are larger than in the experiment. The fact that the estimates for both limiting cases give Seebeck coefficients with smaller absolute values than in the experiment, may tentatively be interpreted as a positive effect of the interfaces on the magnitude of the Seebeck effect.

The considerations made assuming a diffusion of Al donors do not totally exclude that the interface roughness of these samples can lead to similar effects. As can be learned from figure 6.27 the values of the Seebeck coefficient of the undoped ZnO vary significantly. So in this case an integration of the Seebeck profile across a bigger area, as in the case of the electrical conductivity, was not possible. This is mainly due to the high electrical resistivity of the ZnO, which is right at the limit of the measurability with the scanning Seebeck microprobe technique. Furthermore, though one can clearly distinguish between the two materials, a highly resolved scan across the interface is still not possible. This, however, is very important to distinguish between these two effects. In addition it would help to clarify why the local measurements show no big dependence on the bar width whereas the global ones do.

The analysis revealed that, assuming a diffusion of Al donors across the interface from the doped material into the undoped one, the absolute values of the global Seebeck coefficients of the samples could be enhanced by the interfaces. This understanding could only be achieved by the combination of global and local measurement techniques. However, similar to the last section, an improvement of the scanning Seebeck microprobe to higher spatial resolution is crucial to fully clarify the origin of the measured behaviour.

6.4.4 Geometry effects and NeMo simulations

The roughness of the interface caused by the printed mask was a motivation to investigate the influence of a controlled interface geometry on the thermoelectric parameters. For this purpose five different structures, as can be seen in figure 6.30, were designed. All different designs have the same number of interfaces, since they have the same bar width of 20 µm. What makes the difference is the length of the interfaces: The structure with the parallel straight interfaces has the shortest interface length of 5000 µm only. This is just the length of the structured part of the sample (cf. figure 4.3). The structures with the teeth in-phase and teeth in counter-phase (figure 6.30d) and e)) are the ones with the longest interfaces, both with a length of 15000 µm. The toothed interface with constant distance and the wavy structured interface are of intermediate length with 7500 µm (figure 6.30b)) and 10000 µm (figure 6.30c)), respectively. As indicated in figure 4.3, all five designs can be realized in a parallel or in a perpendicular transport geometry. This means that the interfaces are aligned parallel or perpendicular to the main direction of transport caused by an applied temperature gradient.

Since the samples only differ in their interface length throughout the series the origin of the differences measured have to be sought in the geometry. A suitable way to investigate the influence of the geometry of the differently shaped bars is to use the network model described in section 5.3. With *NeMo* it is possible, amongst others, to simulate the thermoelectric transport parameters through a sample consisting of different types of materials. In figure 6.30 bitmaps of the five different stucture patterns (columns a) - e)) for three different cases (lines I) - III)) are shown: In the first line only two materials, indicated by different colours, are present. Effects like space-charge regions or depletion layers can now be incorporated by introducing a third “material”, e.g. the black margins in lines II) and III), which show the effect of a growing space charge region from three to seven pixel. Throughout the simulations the width of the space-charge region was varied from 1 pixel to 8 pixel in 1-pixel steps. The space-charge region was always placed on both sides of the bars of one material only (black margins in figure 6.30). After each increase of the width of the space-charge region the fraction between host material and space-charge

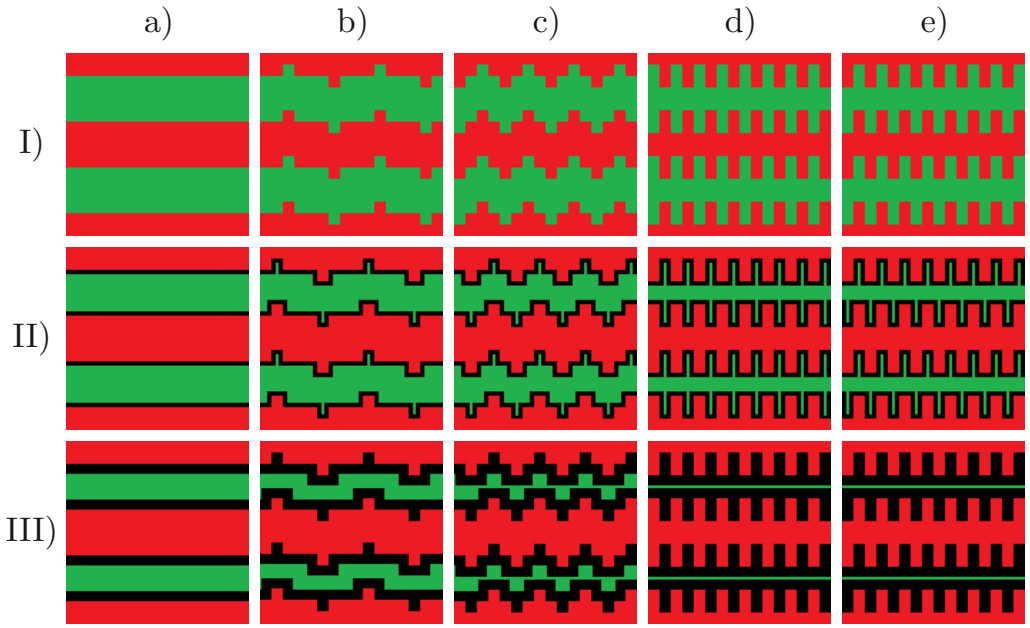

Figure 6.30: 128×128 bitmap-files of the five different geometries which serve as geometrical input data for the network model. Each color represents a different material. For each material input paramters like the electrical conductivity can be chosen by the user. The network model then enables one to calculate the thermoelectric paramters from the left to the right side of the pixel grid. Parallel or perpendicular transport can be realized in the simulation by simply rotating the bitmaps by 90°.

region changes until, at a width of 8 pixels, the structures with the teeth in-phase and teeth in counter-phase are entirely covered by the space-charge region. At this point the simulations equal those of just two materials having resistivities of the space-charge region and of the second material, respectively. The implementation of the space-charge region either into the higher or lower resistivity material could be easily realized by addressing the resistances in an adequate way. These bitmap files serve as geometrical input for *NeMo*. To keep the simulation times moderate a 128×128 pixel grid was chosen. Defining a stripe width of 32 pixels, two bars of each material were included in each simulation. In the samples used in the experiment each bar is 20 µm wide meaning that one pixel of the bitmap corresponds to 0.625 µm on the sample. In *NeMo* the electrodes are always placed on the left and right side of the bitmap, respectively. So the transport is always simulated in horizontal direction. Consequently one can simulate parallel or perpendicular transport by just rotating the bitmaps by 90°.

Two sample series, one in parallel and one in perpendicular transport geometry, were prepared with the self-aligned pattern transfer method. In each series all five patterns were realized. In **perpendicular transport geometry** it is important that both materials have a certain degree of electrical conductance and are in contact to guarantee electrical transport across the entire structure. As a first layer a 200 nm thick MBE grown undoped ZnO film was structured and etched by wet-chemical etching. Again in a second deposition 150 nm of Ga doped ZnO with a higher electrical resistivity was sputtered in between the etched bars yielding an alternating ZnO/ZnO:Ga bar structure. Furthermore the two

materials as thin films have been investigated as references. To enable a comparison the reference samples were structured to have the same geometric dimensions as the patterned fields.

Figure 6.31(a) shows the temperature dependence of the resistivity of the differently structured samples in perpendicular geometry. With decreasing temperature the resistivity increases about one order of magnitude. The variation of the resistivity across the series is about three orders of magnitude. In numbers the two reference samples have resistivities at room temperature of 2.4 Ωm (sputtered ZnO:Ga reference) and $5.7{\cdot}10^{-3}$ Ωm (MBE grown ZnO reference). These values together with the room temperature resistivities of the patterned samples are plotted as a function of interface length in figure 6.32. Furthermore *NeMo* simulations were carried out, to yield a better understanding of the measured trends.

The temperature dependent measurements of the Seebeck coefficient are shown in figure 6.31(c). In a first approximation one would expect that the sample with the highest electrical conductivity has the lowest absolute value of the Seebeck coefficient and vice versa (according to $S \propto \sigma^{-1}$). This trend could not be confirmed in this series. As can be seen in figure 6.31(c) the opposite case is true: The MBE grown reference sample which has the lowest electrical resistivity, has the highest absolute value of Seebeck coefficients with - 434 μVK^{-1} at room temperature. The sputtered reference sample, has the lowest absolute values of S (-140 μVK^{-1} at room temperature). As for the resistivities these two samples mark the limits for this series with the values of all structured samples lying inbetween.

Calculating the power factor for each temperature gives the dependence shown in figure 6.31(e). Of course the unstructured MBE grown reference sample with the highest electrical conductivity and the highest Seebeck coefficient has the highest power factor with 32 $\mu Wm^{-1}K^{-2}$ at 280 K. In general, the order of the structured curves for the power factor is the same as for the electrical conductivity. This shows that the big variation in electrical conductivity dominates the behaviour of the power factor. Due to rather moderate changes of the Seebeck coefficient within the series S does not essentially influence the power factor, despite its quadratic influence. The qualitative progression of the power factor with temperature of one single curve on the other hand is clearly dominated by the quadratic input of the Seebeck coefficient. This becomes clearer with decreasing temperature: Here the electrical conductivity decreases but the Seebeck coefficient increases drastically, leading to an increase of the power factor.

In **parallel transport geometry** the preparation started with a layer of electrical isolating ZnO of 200 nm thickness grown by CVD. After the first etching step by wet chemical etching, 150 nm of Ga doped ZnO was sputtered into the structured ditches. Ga in ZnO is an electron donor leading to n-type doping and to a much higher electrical conductivity compared to the nominal undoped CVD grown ZnO. Consequently the transport parameters should be dominated by the better conducting material. Furthermore, if the geometry has no influence on the transport behaviour, no big differences between the various structures should be observed. Measurements indeed show that the transport is dominated mainly by the material of higher electrical conductivity. The resistivity ρ is shown in figure 6.31(b). No significant changes with temperature in the range from 90 to 280 K can be observed for the different specimens. To give an example, ρ only slightly increases with decreasing temperature, having values of $3.9{\cdot}10^{-3}$ Ωm at 280 K and $4.3{\cdot}10^{-3}$ Ωm at 90 K for the sample with the straight parallel interfaces. The Seebeck coefficients of these samples have been measured in the same temperature range. The temperature depen-

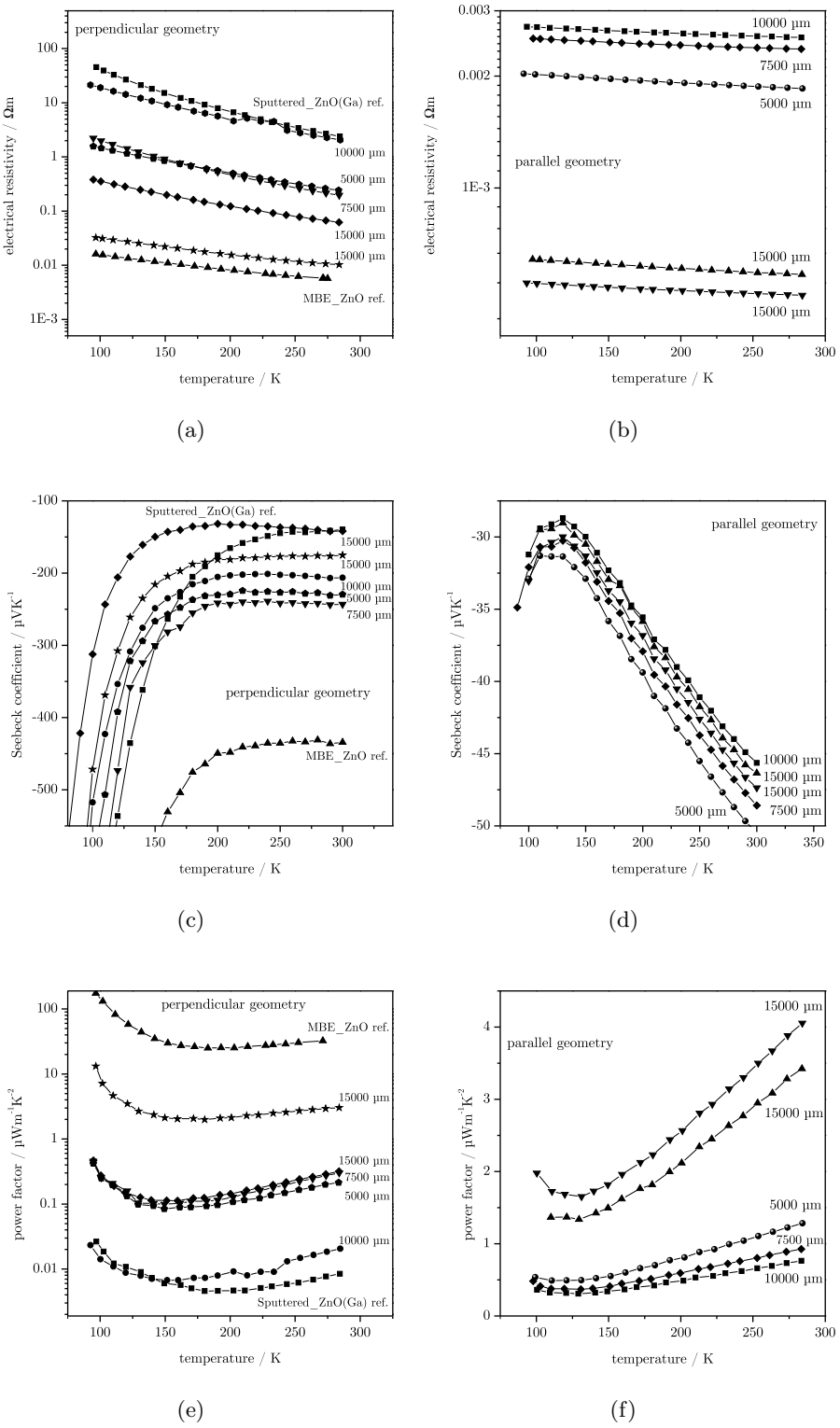

Figure 6.31: Temperature dependence of the electrical resistivity ρ (top row), the Seebeck coefficient S (middle row), and the resulting power factor S^2/ρ (bottom row) of two sample series with different interface lengths. The left column has perpendicular transport geometry and the right column a parallel one.

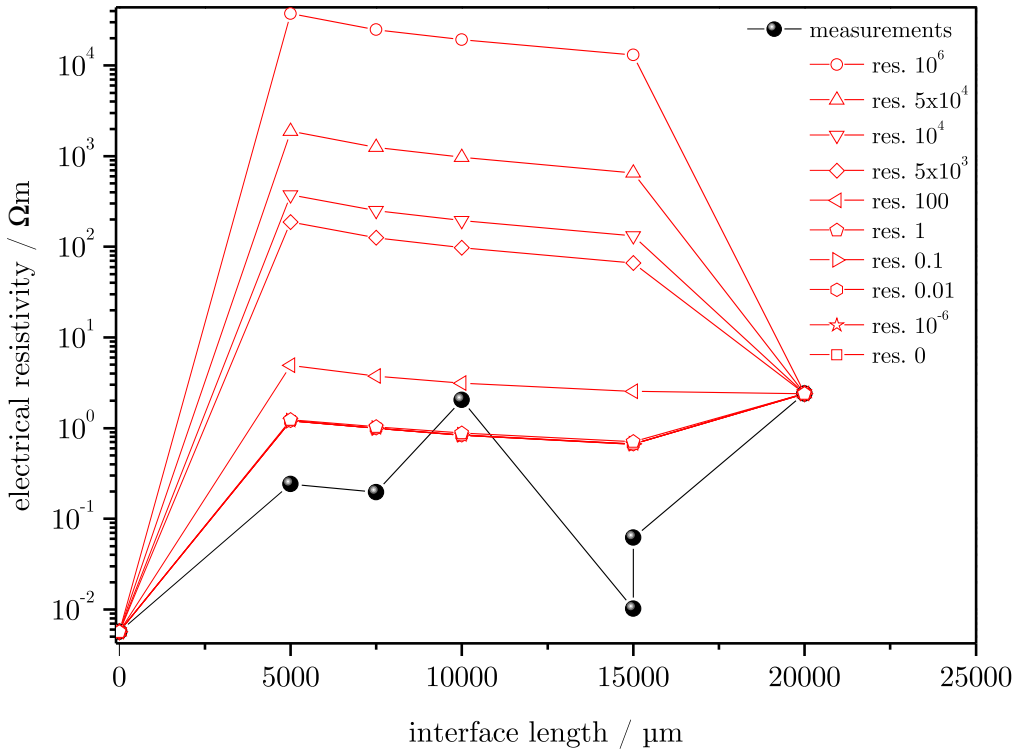

Figure 6.32: *NeMo* simulations of the perpendicular electrical transport across differently shaped interfaces. Due to microstructuring the interface length changes while the number of interface is kept constant throughout the series. The parameter varied in this series of simulations is the interface resistivity, while the ratio of electrical conductance of the two constituent materials is kept at a constant value of 421 to 1, according to the measured ratio of the two reference samples.

dence is shown in figure 6.31(d). All values lie within only 10 µV/K at 300 K (between -45 and -55 µV/K). With decreasing temperature the absolute values of the Seebeck coeffient decrease having a local minimum at about 130 K. Then the absolute values increase again on decreasing the temperature further.

Although the power factor S^2/ρ is proportional to the second power of the Seebeck coefficient, figure 6.31(f) shows that in this case it is dominated by the behaviour of the electrical resistivity ρ. In other words, the small enhancement of S of the samples with high ρ is not large enough to compensate the loss in electrical conductivity, yielding in total smaller values of the power factor. Beside this, the temperature dependence of the power factor is qualitatively dominated by S but quantitatively it shows the same dependence on the interface length than the electrical conductivity.

For the ***NeMo* simulations** the general procedure in both transport geometries was the same: At first the best fit between simulation and experiment for the electrical conductivity was determined. Thereby different assumptions about the interface resistance and the conductance, width and position of the space-charge region were made. For the cases where the agreement was best the Seebeck coefficient was calculated. As for the experiment the power factor was calculated after S^2/ρ.

In a first series of **simulation in perpendicular transport geometry** it was assumed

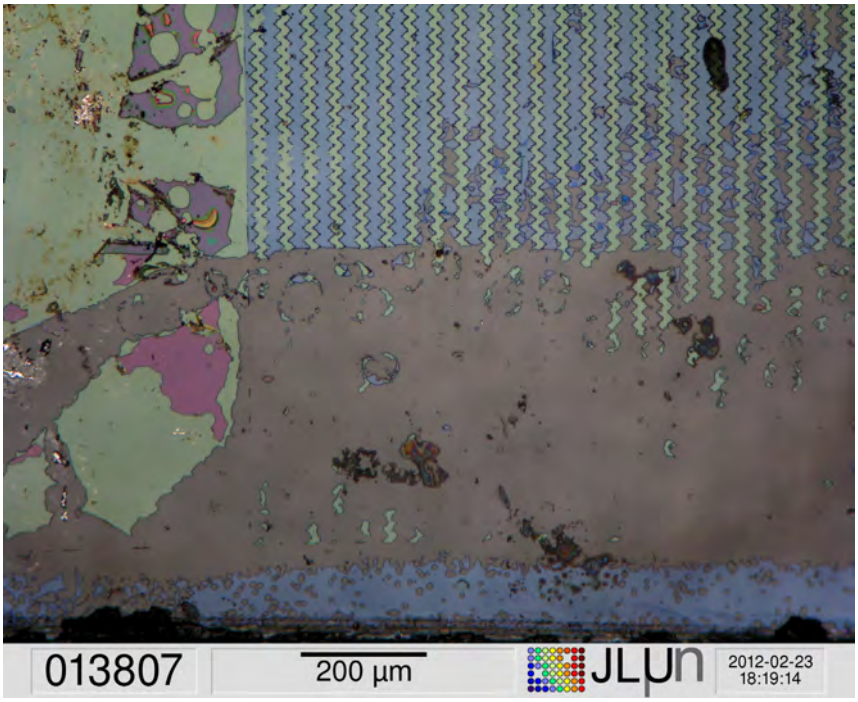

Figure 6.33: Optical image of the sample with an interface length of 10000 µm. One can see that big parts of the structured thin film were removed during lift-off.

that next to the two materials involved, which have a ratio of conductivities of 421/1, a third resistance namely that of the interface is present. This resistance was now varied in the simulations from very high values of 10^6 down to zero. In figure 6.32 the simulated curves for the different interface resistivities as well as the measured values can be seen. All simulations were normalized to the experimental value of the MBE-reference. This does not influence the general trend of the simulations, it only shifts them to the same order of magnitude than the experimental data. In addition it allows the treatment of the input parameters as dimensionless numbers. With decreasing interface resistivity one can see that the curves are shifted to lower resistivity values. This trend however stops below the value of 1. A further reduction even to a value of 0 causes no further decrease of the overall resistivity towards the values of the measured samples. So the assumption of two materials only gives too high simulated resistivity values, even without an interface resistance.

Next to the general shift in the absolute values, there is one point in the experimental data which deviates strongly from the calculated trend: At an interface length of 10000 µm the measured resistivity increases unexpectedly. As can be seen in figure 6.33 big parts of this sample were destroyed during the production process. Here somehow not just the unwanted parts on top of the resist were removed during the lift-off but also big parts of the structured thin film. This resulted in an increase of the electrical resistivity.

To further reduce the differences between simulation and experiment, a space-charge region was introduced. All following simulations were carried out setting the interface resistivity to zero and varying the electrical conductivity, position and width of a space-charge region instead.

In figure 6.34 the simulations for a low resistive space-charge region of different width

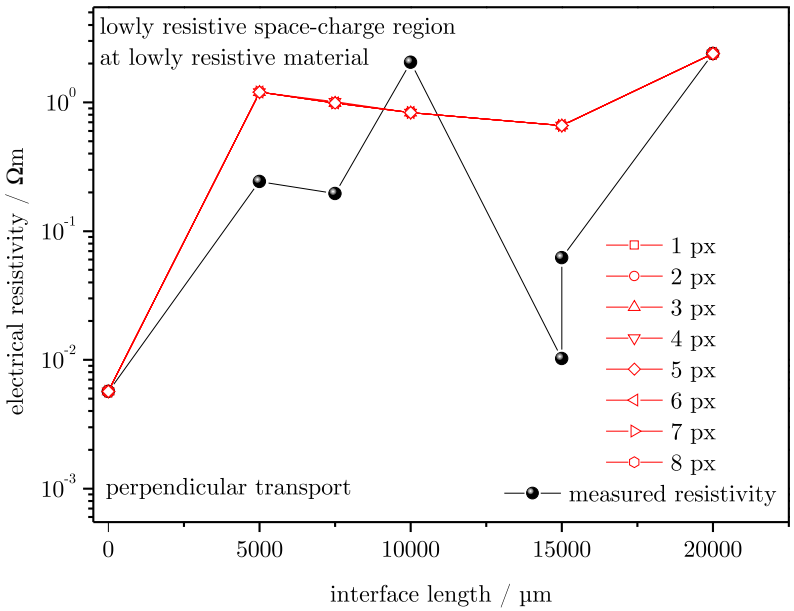

Figure 6.34: *NeMo* simulations of the perpendicular transport through bar structured samples with different interface shapes. The calculations show that the resistivity across the sample series does not change significantly with the width of the low resistive space-charge region placed on the low resistive material.

placed at the low resistive MBE grown material are shown. The values used for the conductivity for the MBE grown ZnO, the sputtered Ga doped ZnO and the space-charge region are 421 to 1 to 10^6, respectively. One can see that a variation of the width of the space-charge region causes no visible changes in the absolute values of the resistivity. From a physics point of view this is expected, since the regions act as additional series resistances of small magnitude improving the already good conductance of this region a little further. So the overall effect compared to the case without a space-charge region is a slight shift to smaller values of the resistivity, independent of the width of the space charge region.

The dependence on the width of the space-charge region becomes more pronounced if a low resistivity space-charge region on the high resistivity material side is assumed. This is shown in figure 6.35: The resistivity decreases with increasing width and simultaneously with growing interface length. This behaviour is structure induced: The shortest path from space-charge region to space-charge region through the high resistivity material decreases as the interface length increases. In addition the fraction of material covered by the space-charge region increases with increasing interface length. This can be seen very well in line III) of figure 6.30. Here the space-charge region (black) has a width of 7 pixel. One can see that for the longest interfaces (structures d) and e) in figure 6.30) only a small part of the host bar is left. Increasing the width further (8 pixel) covers the entire bar of the highly resistive material with the well conducting space-charge region. This explains the drastic drop in resistivity for an interface length of 15000 µm. A similar behaviour

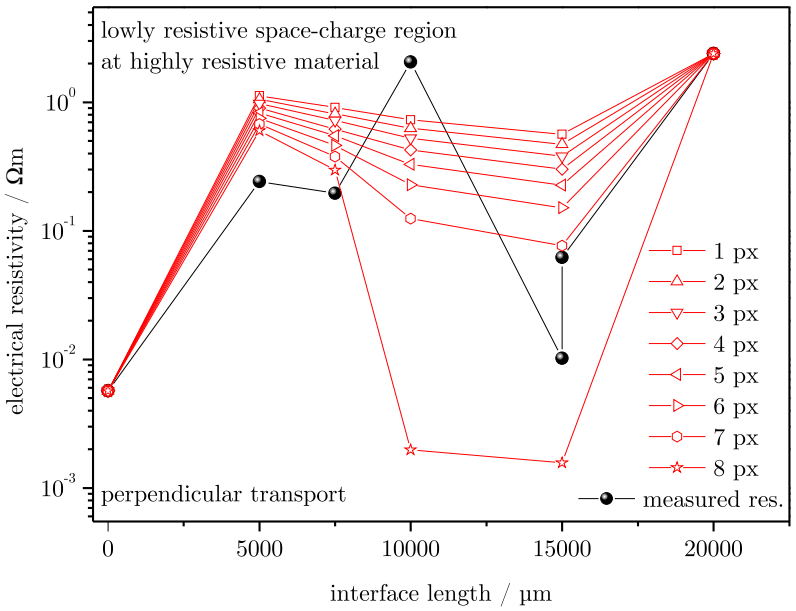

Figure 6.35: *NeMo* simulations of the perpendicular transport through bar structured samples of different interface shapes. The calculations show that the resistivity throughout the sample series shifts towards lower absolute values by increasing the width of the low resistive space-charge region placed on the highly resistive material. At a width between 7 and 8 pixels the agreement with the experiment is best.

is observed for an interface length of 10000 µm (structure c) in figure 6.30). In this case the absolute value of the resistivity is slightly higher, although the space-charge regions overlap as well. This overlapping however is not along the entire bar, but is interrupted by small "islands" of the high resistive material. This shows that these inclusions, even if they are isolated, have an impact on the overall resistivity.

The best agreement between experiment and simulation concerning the electrical resistivity within the three considered cases are summed up in figure 6.36(a). One can see that there is effectively no difference between the case without a space-charge region and that assuming a low resistivity space-charge region on the low resistivity material. Only the substitution of almost the entire high resistivity material with a low resistivity space-charge region gives a good fit of the experiment.

With these parameters simulations of the Seebeck coefficient for the different structures have been carried out. Here not only the conductance of each material has to be inserted, but also the Seebeck coefficient and the thermal conductance. Since the Seebeck coefficients of the reference materials are known, this ratio (3.1:1 for MBE grown:sputtered) was entered for the respective bars. The value for the space-charge region was set to $1.3 \cdot 10^{-3}$, according to the relation of the conductances assumed above. The thermal conductances were all set to 1. This corresponds to the assumption that the differences in thermal conductivity between MBE grown and sputtered material can be neglected because the

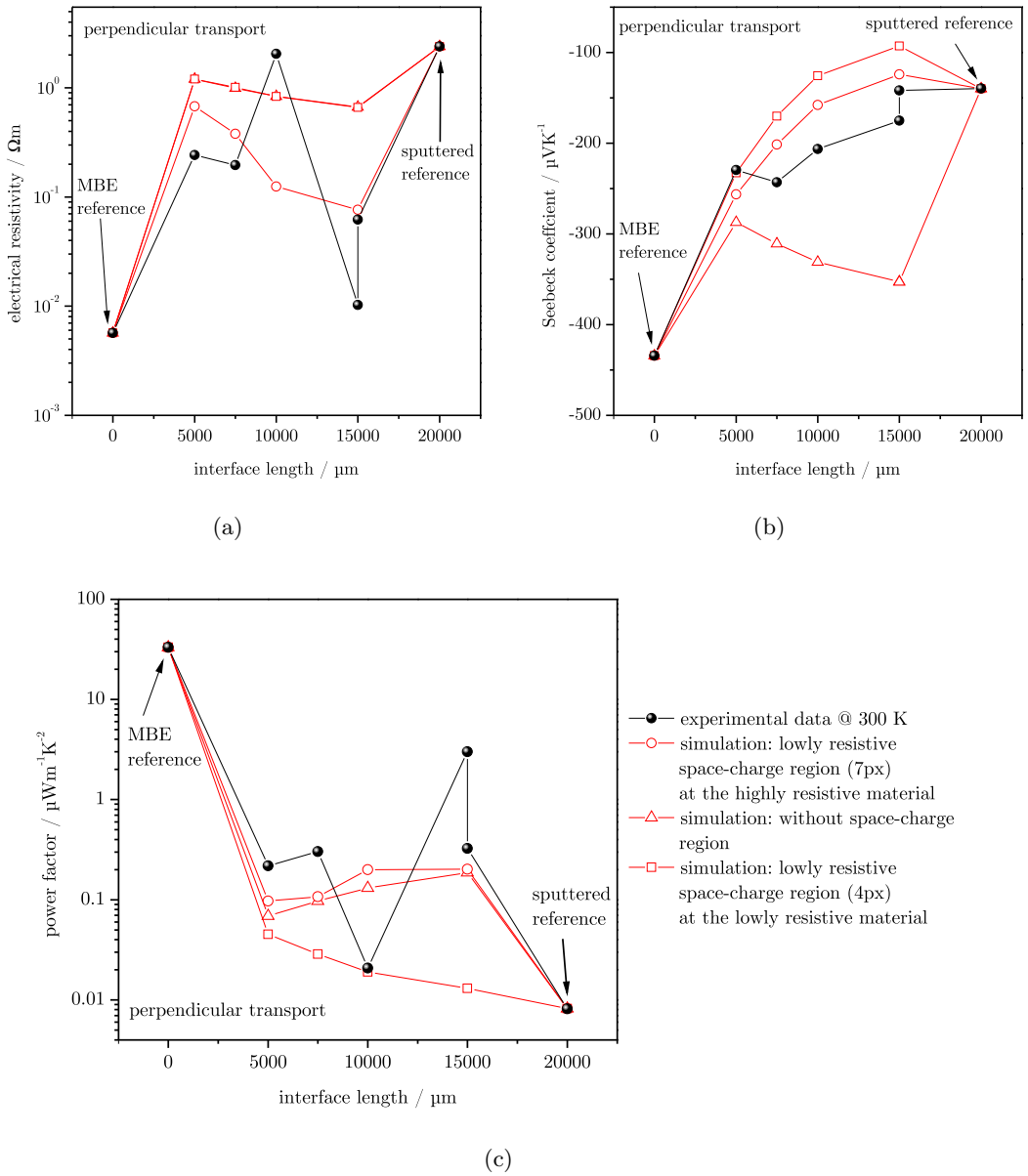

Figure 6.36: *NeMo* simulations of the Seebeck coefficient of structured samples with different interface shapes in perpendiculat geometry.

temperature difference across the sample is mainly determined by the substrate. This is justified in this case due to a highly heat conducting sapphire substrate.

The results together with the measured values at room temperature are shown in figure 6.36(b). Without a space-charge region, the measured trend cannot be simulated. With increasing interface length the calculated $|S|$ is increasing whereas the experimental values decrease. This changes by implementing a low resistivity space-charge region. Placing this region on the low resistivity material already reproduces the experimental trend very nicely. It is remarkable that for the simulations of the Seebeck coefficient the presence of a space-charge has a big influence on the result. The assumption of a low

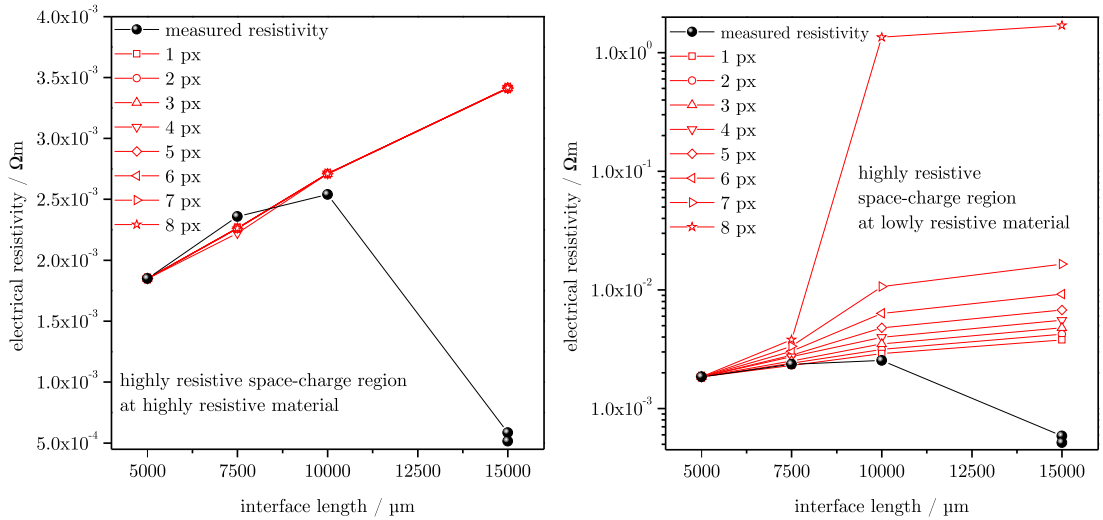

Figure 6.37: *NeMo* of parallel transport simulations assuming a high resistive space-charge region. (a) The space-charge region is positioned on the low conductive material. (b) The space-charge region is positioned on the high conductive material.

resistivity space-charge region on the low resistivity material gives the lowest absolute values of S whereas without a space-charge region the highest $|S|$ values are obtained. For the electrical resistivity these to cases were almost indistinguishable. The reason for this big difference is the very small value of $|S|$ of the space-charge region. As for the electrical conductivity, the best agreement with the experiment can be achieved by assuming a relatively wide space-charge region (7 px) at the high resistivity material.

This is also true for the calculated power factors S^2/ρ shown in figure 6.36(c). Here the subtle interplay between electrical resistivity ρ and Seebeck coefficient S determines the behaviour: Due to comparatively high resistivities dominated by the high resistivity material while having the lowest values of $|S|$ originating from the space-charge region, the combination of a low resistivity space-charge region on the low resistivity material gives the lowest power factors. The further decrease with increasing interface length has to originate from the decrease of the absolute values of the Seebeck coefficient. Without a space-charge region the behaviour of S changes: $|S|$ increases, with increasing interface length, a behaviour that is reflected by the corresponding power factors as well. Though the absolute values of S decreases with increasing interface length for a 7 pixel wide space-charge region of high conductivity on the low conductivity material, the power factors are higher than those without a space-charge region. This is due to the strong reduction in electrical resistivity. The fact that the power factor follows the behaviour of the electrical conductivity point by point further confirms this explanation.

Simulations in parallel transport geometry of the electrical resistivity were carried out, assuming two materials and a space-charge region, all three with different electrical conductivities. Furthermore the width of the space-charge region and its position (on the highly resistive or on the lowly resistive material) were varied. Because no values for the conductivities of the reference materials were available it was assumed that the lowly

resistive material has a thousand times higher electrical conductivity than the highly resistive one. The high resistivity space-charge region was set to resisitivity values a thousand times higher than that of the high resistivity material. On the other hand the low resistivity space-charge region was assumed to have a thousand times higher conductivity than the better conducting material. All simulations were normalized to the measured value of the resistivity of the bar structure with the straight parallel interfaces and a bar width of 20 µm.

Figures 6.37 and 6.38 show the comparison between experiment (black spheres) and simulations of the resistivity as a function of interface length in parallel transport direction. The measured values at 280 K throughout the series have resistivity values between $5 \cdot 10^{-4}\,\Omega$m and $5 \cdot 10^{-3}\,\Omega$m. At first sight no clear trend or dependence can be found. The samples with the longest interfaces of 15000 µm have the highest electrical conductivities. This is somewhat surprising, since one would expect that the more interface states (which may trap free carriers) are available the lower is the electrical conductivity. On the other hand, if a space-charge region of high conductivity at the interface is assumed this region would dominate the electrical transport. In this case an increase of the interface length could explain the measured behaviour.

In the case of simulating a high resistive space-charge region on a high resistive material no big dependence on the width of the space-charge region is obtained in parallel geometry. This is expected, since the main part of the transport is carried by the highly conducting material. Whether the second material is a thousand or a million times higher in resistance does not make a big difference. Nevertheless the agreement with the experiment is quite good except for the interface length of 15000 µm.

The dependence on the width of the space-charge region becomes more pronounced placing the highly resistive space-charge region on the highly conducting bars (figure 6.37(b)). For a width of one pixel again the agreement with the experiment up to 10000 µm of interface length is quite good. But as the width increases further the resistivity increases as well, making the difference between simulated values and experimental values even more drastic with increasing interface length. The measured reduction of the resistivity at 15000 µm cannot be modelled using these parameters. The drastic increase for a width of 8 pixels for the last two points is geometry induced. For these two structures the space-charge regions start to overlap in the middle of the bar, such that the highly conductive transport path in the host material is interrupted.

In figures 6.38(a) and (b) the simulations of the resistivity were carried out assuming parallel transport and highly conducting space-charge regions of different width again positioned on the lowly conducting and highly conducting material, respectively. In this case the width of the space-charge region plays an important role. One can see that up to a width of 3 pixel the behaviour of the simulation is similar to that assuming a highly resistive space-charge region: The resistivity increases with increasing interface length. However as the width reaches 4 pixels the resistivity drops down to values below the measured ones. Furthermore the simulations now show qualitatively the same behaviour as the experiment: Up to an interface length of 10000 µm the resistivity increases with increasing length, then suddenly drops down even below the value of the sample with the unstructured interfaces. But what happens at the transition from 3 to 4 pixel of space-charge region that can cause such a drastic change in the transport behaviour? The explanation is, that at a width of 4 pixels the teeth in the artificial interface structures are completely filled by the space-charge region. This enables a more direct transport path through the highly conducting region of the bar. The higher the reduction in path

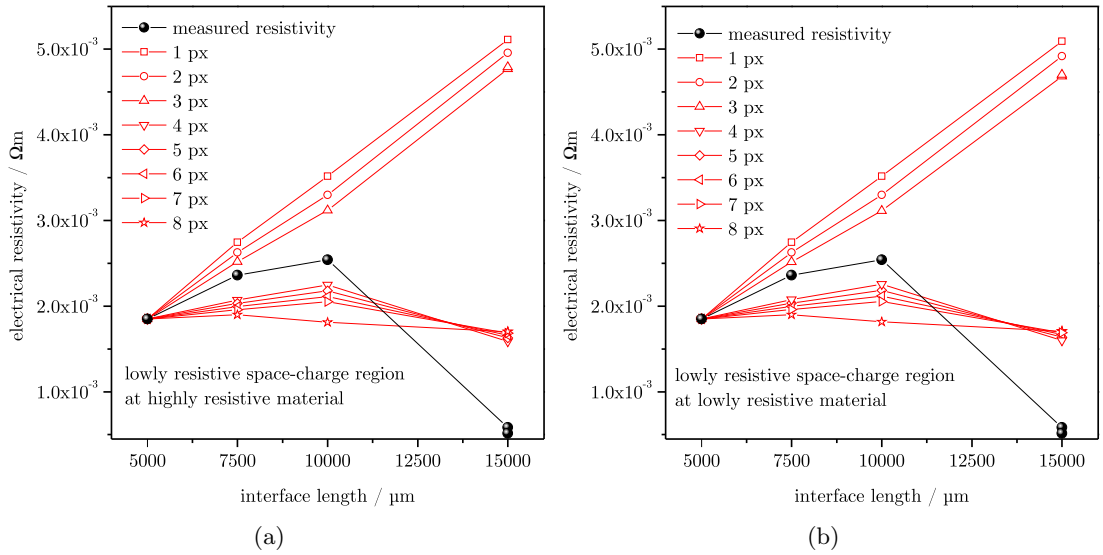

Figure 6.38: *NeMo* of parallel transport simulations assuming a high conductive space-charge region. (a) The space-charge region is positioned on the low conductive material. (b) The space-charge region is positioned on the high conductive material.

length the more pronounced should be the reduction in resistivity. This explains the drop of the resistivity for the interface length of 15000 µm. Here the effective shortening of the transport path is maximal within the sample series. Why the drop in the experiment is even more pronounced is not clarified yet. Fact is that the experiment can be very well simulated assuming of a low resistivity space-charge region. Whether this region is positioned on the high or low conductive material is of minor importance, as both graphs of figure 6.38 are almost identical. This again shows, that the space-charge region carries the major part of the electrical transport. A further increase of the width of this region to 5, 6 or 7 pixels has no big impact on the transport behaviour. A 8 pixel wide space-charge region finally makes the resistivity almost independent of interface length.

Similar to the simulations in perpendicular transport geometry, the best fit of the electrical resistivity of each considered parameter combination is summarized in figure 6.39(a). The decrease in resistivity for an interface length of 15000 µm can only be simulated assuming a highly conducting space-charge region.

The simulations of S as a function of interface length are shown in figure 6.39(b). As for the simulations in perpendicular geometry only those values for the pixel width and electrical conductivity were used for the simulations where the agreement for the resistivity was best in each of the four observed cases. The values for the thermal conductivities for all three regions were set to 1, assuming that the substrate carriers the major part of the heat transport. As input for the Seebeck coefficients of the low conductive material a value of -50 µV/K was taken. For the other two regions S was changed according to the respective change in resistance. Here the simulations were normalized again to those of the sample with 5000 µm interface length. As can be seen in figure 6.39(b) the measured trend cannot be simulated very well in any of the four cases. The assumption of a high resistive space-charge region leads to continuous increase of $|S|$ with increasing interface length, independent of the position of the space-charge region. This changes assuming a

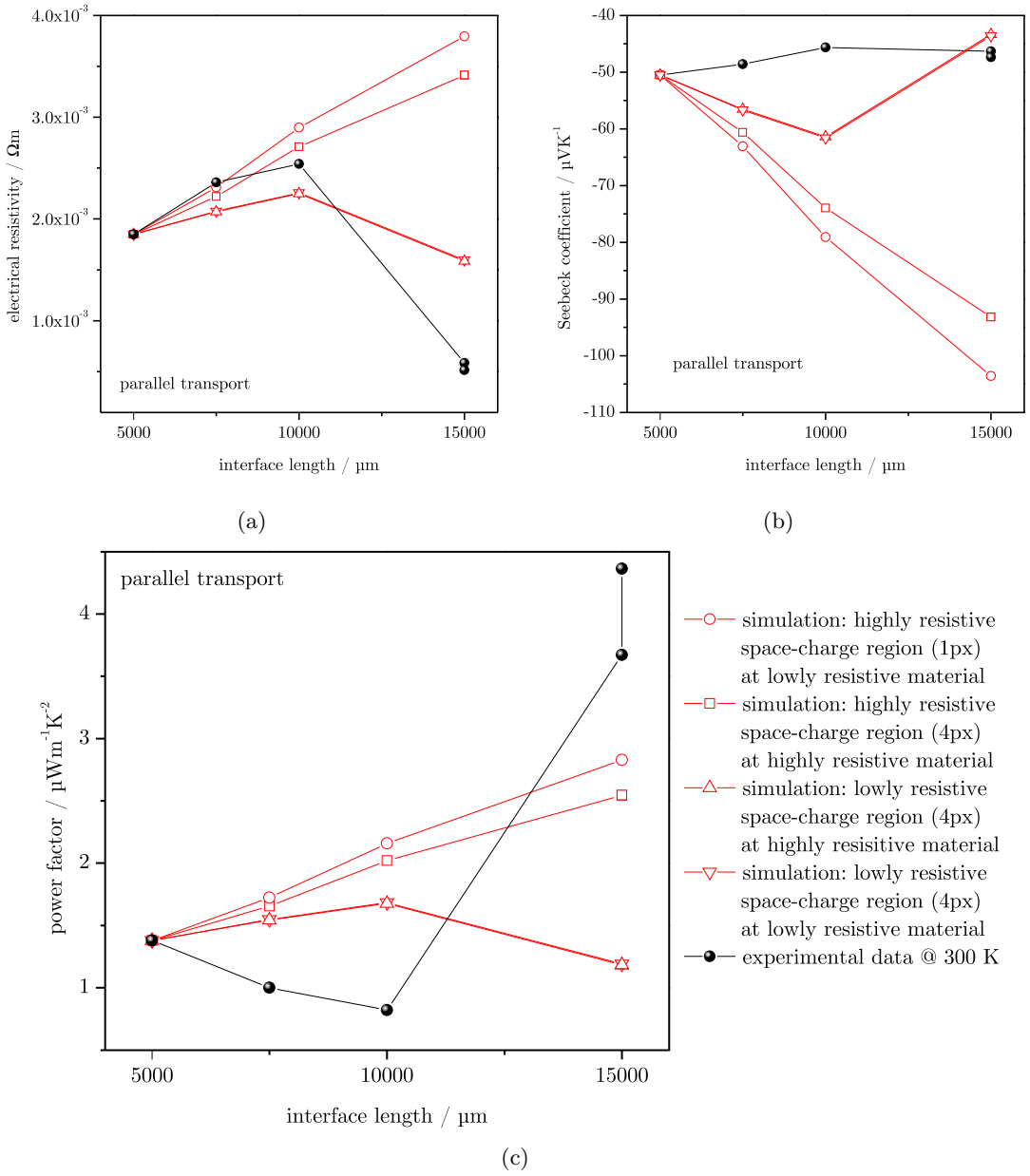

Figure 6.39: Summary of the best *NeMo* simulation fits of the electrical conductivity, the Seebeck coefficient and the power factor of structured samples with different interface shapes in parallel geometry.

low resistive space-charge region. After increasing with increasing interface length, the absolute value of the Seebeck coefficient decreases again for a 15000 µm long interface. This is probably due to the direct path that occurs for these samples at a space-charge region width of 4 pixel. The failure in reproducing the measured trend is most likely due to the lack of experimental data for the Seebeck coefficient of the reference materials.

The errors made in the simulations of S dominate the calculation in the power factors shown in figure 6.39(c). Here the dependence on the interface length is mainly affected

by the Seebeck coefficient. Where $|S|$ increases with increasing interface length the power factor also increases. For a highly conducting space-charge region the power factor peaks at 10000 µm, whereas it increases further for the assumption of a high resistivity space-charge region. The measured power factor however decreases with increasing interface length to then strongly increase again.

In conclusion, the simulations for both geometries suggest a highly conducting space-charge region placed at the low conductivity material. However in both cases it could not be claryfied whether this assumption is true. In perpendicular geomtry the interfaces have point contacts, but the MBE grown ZnO of higher electrical conductivity is nominal undoped so that a diffusion into the sputtered material can be ruled out. The good electrical conductivity comes from a high carrier mobilty, which for this material is about hundred times higher than the one of the sputtered counterpart. A clarification whether this high mobilty alone can have such a big influence or if other effects may occur at the interfaces is still missing so far.

In parallel geometry the situation is even more complicated. Here the two materials were separated by gap during the production process. So again the diffusion of Ga into the electrical isolating CVD grown ZnO can be excluded. The origin of a potential highly conducting interface region on this material still needs to be claryfied. In both cases only local measurements of the electrical conductivity can reveal the real nature of the interface.

Summary

The typical and best understood thermoelectric materials such as Bi_2Te_3 or PbTe so far are based on Te. Unfortunately, when it comes to a mass application of thermoelectric devices, estimations show that the tellurium resources will be consumed very quickly. Hence it is worth trying to develop novel thermoelectric materials which are more sustainable and "green". Exemplarily the thermoelectric properties of ZnO as an ideal model system were investigated in the framework of this thesis.

A major advantage of ZnO is that thin-films can be grown by various methods. Their carrier concentrations can be easily influenced during growth, e.g. n-type doping over a wide range, or after growth, e.g. by annealing. The change in carrier concentration has a big impact on the Seebeck coefficient. Investigations of degenerately doped ZnO:Al and subsequent annealing in air showed that at very high carrier concentrations, where the samples have metallic character, a sign reversal of S may occur. Although the sample is clearly n-type, small positive Seebeck coefficients can be measured, changing their sign with decreasing temperature. This is due to changes of the density of states at the Fermi-energy in a degenerately doped semiconductor.

In the case of sputtered ZnO films grain boundary states cause a bending of the conduction band forming a so called double Schottky barrier. This leads to a redistribution of the energy of the charge carriers before and after the barrier. This energy filtering effect (charge carriers with energies lower than the potential height are backscattered) is supposed to lead to an enhancement of the power factor. Measurements combined with calculations within a one band effective mass model showed that an increase of the power factor with increasing carrier concentration only works to a certain extend. If the carrier concentration exceeds a certain value, screening effects diminish the barrier height and width leading to a decrease of the power factor. Here the maximum of the power factor was found for $n = 1.6 \cdot 10^{19}\,\mathrm{cm}^{-3}$.

In many cases improved thermoelectric properties of the nanostructured material compared to the respective bulk could be shown. Here ZnO has the big advantage that nanofabrication techniques known from the semiconductor industry can be applied to this material as well. Etching a regular square-hole pattern into a thin sputtered ZnO film showed a shift of $|S|$ to higher values with decreasing hole size. This can be explained by the generated additional sample surface whilst keeping its volume constant causing additional defects, e.g. electron traps, that can reduce the total number of free carriers, as well as a rough surface morphology. Simulations of the patterned material assuming a depletion region of constant width could reproduce the measured trend nicely.

In nanostructured materials surface and interface effects become dominant. The investigation and understanding of these interface effects and their influence on the thermoelectric properties was the main focus of this work. One of the simplest ways to generate interfaces is by growing multilayer structures. Here a sample series of alternating ZnO/ZnS layers was investigated in in-plane geometry. The findings gave hints for the formation of interface layers of very high electrical conductivity between ZnO and ZnS, dominating the transport behaviour at large layer thicknesses ($d > 100\,\mathrm{nm}$). At smaller d, where

d becomes comparable to the typical fluctuation length of the interface roughness, the transport path (and hence the thermoelectric properties) is strongly determined by the surface fluctuations. These results could be approved qualitatively by *NeMo* simulations.

Stronger impact on the thermoelectric parameters, especially on the thermal conductivity, were found in cross plane direction, i.e. perpendicular to the interfaces. Unfortunately measurements of multilayers in cross-plane direction are very difficult to perform. To overcome this problem lateral structuring of thin-films offers attractive possibilities. To realize bar structures of alternating materials the method of self-aligned pattern transfer was developed and employed. With a simple printed mask a series of bar-shaped samples of alternating ZnO:Al and ZnO stripes was fabricated. Varying the number of interfaces between the two materials whilst keeping the material fractions constant, revealed interesting results. Raman, photoluminescence and thermoelectric measurements were performed globally and locally. The observed dependence on the number of interfaces can be explained by two effects. One assumes a diffusion of Al-donors from the ZnO:Al stripes into the adjacent undoped ZnO stripes. Calculations based on a network model assuming a Fermi-like diffusion profile corroborate these findings and suggest that the region affected by the diffusion is of a width of the order of 100 µm. The activation energy of Al-diffusion in bulk crystalline ZnO is 2.74 eV, therefore, the diffusion process is likely to occur along the grain boundaries in these sputtered samples. On the other hand local probes of the electrical conductivity give hint to the assumption that the measured global effects can also be explained by the interface roughness which, for this sample series, was in the same order of magnitude (about 80 µm).

A scanning probe analysis of the diffusion profile revealed further that the interface structure hinders the diffusion process as the diffusion across the interface is slower than along the grain boundaries. In addition, the measurements give evidence that the absolute values of the global Seebeck coefficients of the samples is enhanced by the interfaces.

Not just the number of interfaces but also their shape has an influence on the thermoelectric properties. This is true not only for the transport perpendicular to the interfaces but also in parallel transport direction. Again with the method of self-aligned pattern transfer two series of samples consisting of alternating high and low electrical conducting material, one in parallel and the other in perpendicular geometry, were fabricated. The number of interfaces as well as the material fractions were not altered. The changing parameter throughout the series was the interface length. Supported by numerous *NeMo* simulations the results indicated that the thermoelectric propeties across the sample is dominated by the shortest path of electrical conductance. The transport path is strongly influenced by assuming space-charge regions of different width and conductivity. Best agreement between experiment and simulations in both geometries has been achieved by replacing a certain fraction of the lowly conducting material with a highly conducting space-charge region. However, the origin of this highly conducting surface region requires further clarifications.

Due to its high Seebeck coefficients and the possibilty to tune the electrical conductivity by doping, ZnO is a promising candidate for an environmentally friendly and sustainable n-type thermoelectric material. In addition, as presented within this work, the possibilities to tune and even improve these properties are manifold. The fact that its thermal conductivity is quite high may be overcome by a combination with ZnS. This back door shown by theory, however still needs to be approved by experiment. First measurements of the local thermal conductivity on an alternating ZnO/ZnO:Ga bar structure, however show clear differences between the two areas, although it is the same host material (figure 6.40).

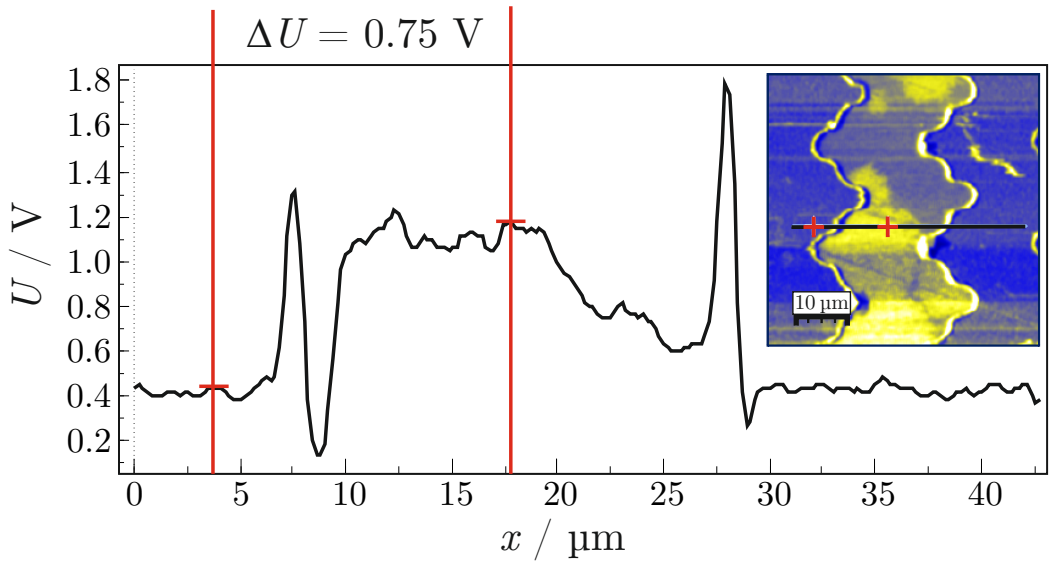

Figure 6.40: Scan of the local thermal conductivity of a structured sample. The alternating materials of the bar strucutre are CVD-grown ZnO and sputtered Ga doped ZnO. The bar strucutres have an artificial interface roughness. The different thermal conductivities are indicated by different heating voltages that are necessary to keep a constant temperature at the sample surface. This is shown in the inset by different colours. The red crosses in the inset correspond to the red lines in the graph.

This motivates attempts of producing alternating ZnO/ZnS bar structures where the thermal conductivity is dominated by the incompatible phonon dispersion relations of the two materials. The electrical conductivity on the other hand can be tuned by doping and by tuning the interface properties. As shown in this work the possiblities here are manifold. Furthermore, it was also shown that due to microstructuring the power factors were only tuned within the limits of the two constituent materials. It was not possible so far to gain higher power factors than those of the as grown material. This implies that interface strucuturing here only brings an enhancement of the total figure of merit, if its benefit due to a reduction of the thermal conductivity exceeds its loss in the power factor.

To be able to evaluate all occuring effects on the micrometer scale it is crucial to apply local probes for measuring the thermoelectric parameters. Only with the knowledge about the local effects it is possible to interpret their impact on the global quantities properly. This in turn enables theoretical predictions to find the best thermoelectric performance for each type of device.

Concerning the application of ZnO in a thermoelectric generator, an adequate p-type counterpart needs to be found. First experiments show, that Cu_xO might fulfill all necessary requirements.

Bibliography

[1] T. J. Seebeck, *Magnetische Polarisation der Metalle und Erze durch Temperatur-Differenz*, Abhandlungen der Königlichen Preußischen Akademie der Wissenschaften zu Berlin 265 (1822-1823)

[2] E. Altenkirch, *Über den Nutzeffekt der Thermosäule*, Physikalische Zeitschrift **10**, 560–580 (1909)

[3] E. Altenkirch, *Elektrothermische Kälteerzeugung und reversible elektrische Heizung*, Physikalische Zeitschrift **12**, 920–924 (1911)

[4] R. Franz, G. Wiedemann, *Ueber die Wärme-Leitungsfähigkeit der Metalle*, Annalen der Physik **165**, 497–531 (1853), ISSN 1521-3889, doi: 10.1002/andp.18531650802

[5] L. Lorenz, *Bestimmung der Wärmegrade in absolutem Maaße*, Annalen der Physik **223**, 429–452 (1872), ISSN 1521-3889, doi:10.1002/andp.18722231107

[6] J. R. Sootsman, D. Y. Chung, M. G. Kanatzidis, *Alte und neue Konzepte für thermoelektrische Materialien*, Angewandte Chemie **121**, 8768–8792 (2009)

[7] G. A. Slack, *CRC Handbook of Thermoelectrics*, CRC, Boca Raton, FL (1995)

[8] B. Sales, B. Chakoumakos, D. Mandrus, J. Sharp, *Atomic displacement parameters and the lattice thermal conductivity of clathrate-like thermoelectric compounds*, Journal of Solid State Chemistry **146**, 528–532 (1999), ISSN 0022-4596, doi:10.1006/jssc.1999.8354

[9] J. Dong, O. F. Sankey, G. K. Ramachandran, P. F. McMillan, *Chemical trends of the rattling phonon modes in alloyed germanium clathrates*, Journal of Applied Physics **87**, 7726–7734 (2000), doi:10.1063/1.373447

[10] J. Martin, G. S. Nolas, H. Wang, J. Yang, *Thermoelectric properties of silicon-germanium type I clathrates*, Journal of Applied Physics **102**, 103719 (2007), doi: 10.1063/1.2817400

[11] A. Saramat, G. Svensson, A. E. C. Palmqvist, C. Stiewe, E. Mueller, D. Platzek, S. G. K. Williams, D. M. Rowe, J. D. Bryan, G. D. Stucky, *Large thermoelectric figure of merit at high temperature in Czochralski-grown clathrate $Ba_8Ga_{16}Ge_{30}$*, Journal of Applied Physics **99**, 023708 (2006), doi: 10.1063/1.2163979

[12] J.-H. Kim, N. L. Okamoto, K. Kishida, K. Tanaka, H. Inui, *High thermoelectric performance of type-III clathrate compounds of the Ba-Ge-Ga system*, Acta Materialia **54**, 2057–2062 (2006), ISSN 1359-6454

[13] A. Bentien, M. Christensen, J. D. Bryan, A. Sanchez, S. Paschen, F. Steglich, G. D. Stucky, B. B. Iversen, *Thermal conductivity of thermoelectric clathrates*, Phys. Rev. B **69**, 045107 (2004), doi:10.1103/PhysRevB.69.045107

[14] G. K. H. Madsen, K. Schwarz, P. Blaha, D. J. Singh, *Electronic structure and transport in type-I and type-VIII clathrates containing strontium, barium, and europium*, Phys. Rev. B **68**, 125212 (2003), doi:10.1103/PhysRevB.68.125212

[15] L. D. Hicks, M. S. Dresselhaus, *Effect of quantum-well structures on the thermoelectric figure of merit*, Phys. Rev. B **47**, 12727–12731 (1993)

[16] L. D. Hicks, M. S. Dresselhaus, *Thermoelectric figure of merit of a one-dimensional conductor*, Phys. Rev. B **47**, 16631–16634 (1993)

[17] M. Dresselhaus, G. Chen, M. Tang, R. Yang, H. Lee, D. Wang, Z. Ren, J.-P. Fleurial, P. Gogna, *New directions for low-dimensional thermoelectric materials*, Adv. Mater. **19**, 1043–1053 (2007), ISSN 1521-4095

[18] R. Venkatasubramanian, *Lattice thermal conductivity reduction and phonon localizationlike behavior in superlattice structures*, Phys. Rev. B **61**, 3091–3097 (2000), doi:10.1103/PhysRevB.61.3091

[19] R. Venkatasubramanian, E. Siivola, T. Colpitts, B. O'Quinn, *Thin-film thermoelectric devices with high room-temperature figures of merit*, Nature **413**, 597–602 (2001), ISSN 0028-0836

[20] J. König, M. Winkler, S. Buller, W. Bensch, U. Schürmann, L. Kienle, H. Böttner, *Bi_2Te_3- Sb_2Te_3 superlattices grown by nanoalloying*, Journal of Electronic Materials **40**, 1266–1270 (2011), ISSN 0361-5235, 10.1007/s11664-011-1578-0

[21] N. Peranio, M. Winkler, Z. Aabdin, J. König, H. Böttner, O. Eibl, *Room temperature MBE deposition of Bi_2Te_3 and Sb_2Te_3 thin films with low charge carrier densities*, physica status solidi (a) 1–5 (2011), ISSN 1862-6319, doi:10.1002/pssa.201127440

[22] M. Bachmann, M. Czerner, S. Edalati-Boostan, C. Heiliger, *Atomistic Green's Function Method supported by ab initio Calculations : Application to phonon transport in ZnO and ZnS* (2011), http://arxiv.org/abs/1111.2540

[23] B. Yang, G. Chen, *Partially coherent phonon heat conduction in superlattices*, Phys. Rev. B **67**, 195311 (2003), doi:10.1103/PhysRevB.67.195311

[24] G. Chen, *Thermal conductivity and ballistic-phonon transport in the cross-plane direction of superlattices*, Phys. Rev. B **57**, 14958–14973 (1998), doi:10.1103/PhysRevB.57.14958

[25] W. S. Capinski, H. J. Maris, T. Ruf, M. Cardona, K. Ploog, D. S. Katzer, *Thermal-conductivity measurements of GaAs/AlAs superlattices using a picosecond optical pump-and-probe technique*, Phys. Rev. B **59**, 8105–8113 (1999), doi:10.1103/PhysRevB.59.8105

[26] W. Müller, D. Bertram, H. T. Grahn, K. von Klitzing, K. Ploog, *Competition between thermally induced resonant tunneling and phonon-assisted tunneling in semiconductor superlattices*, Phys. Rev. B **50**, 10998–11001 (1994), doi: 10.1103/PhysRevB.50.10998

[27] B. C. Daly, H. J. Maris, Y. Tanaka, S. Tamura, *Molecular dynamics calculation of the in-plane thermal conductivity of GaAs/AlAs superlattices*, Phys. Rev. B **67**, 033308 (2003), doi:10.1103/PhysRevB.67.033308

[28] T. Yao, *Thermal properties of AlAs/GaAs superlattices*, Applied Physics Letters **51**, 1798–1800 (1987), ISSN 00036951, doi:DOI:10.1063/1.98526

[29] W. E. Bies, R. J. Radtke, H. Ehrenreich, *Phonon dispersion effects and the thermal conductivity reduction in GaAs/AlAs superlattices*, Journal of Applied Physics **88**, 1498–1503 (2000), ISSN 00218979, doi:DOI:10.1063/1.373845

[30] Ü. Özgür, X. Gu, S. Chevtchenko, J. Spradlin, S. Cho, H. Morko, F. Pollak, H. Everitt, B. Nemeth, J. Nause, *Thermal conductivity of bulk ZnO after different thermal treatments*, Journal of Electronic Materials **35**, 550–555 (2006), ISSN 0361-5235, 10.1007/s11664-006-0098-9

[31] T. Olorunyolemi, A. Birnboim, Y. Carmel, O. C. Wilson, I. K. Lloyd, S. Smith, R. Campbell, *Thermal conductivity of zinc oxide: From green to sintered state*, Journal of the American Ceramic Society **85**, 1249–1253 (2002), ISSN 1551-2916, doi:10.1111/j.1151-2916.2002.tb00253.x

[32] T. Tsubota, M. Ohtaki, K. Eguchi, H. Arai, *Transport properties and thermoelectric performance of* $(Zn_{1-y}Mg_y)_{1-x}Al_xO$, J. Mater. Chem. **8**, 409–412 (1998), ISSN 0959-9428

[33] K. F. Cai, E. Müller, C. Drasar, A. Mrotzek, *Preparation and thermoelectric properties of Al-doped ZnO ceramics*, Materials Science and Engineering B **104**, 45–48 (2003), ISSN 0921-5107

[34] S. Katsuyama, Y. Takagi, M. Ito, K. Majima, H. Nagai, H. Sakai, K. Yoshimura, K. Kosuge, *Thermoelectric properties of* $(Zn_{1-y}Mg_y)_{1-x}Al_xO$ *ceramics prepared by the polymerized complex method*, Journal of Applied Physics **92**, 1391–1398 (2002), ISSN 00218979, doi:DOI:10.1063/1.1489091

[35] M. Ohtaki, K. Araki, K. Yamamoto, *High thermoelectric performance of dually doped ZnO ceramics*, Journal of Electronic Materials **38**, 1234–1238 (2009), ISSN 0361-5235, 10.1007/s11664-009-0816-1

[36] H. Hillmer, A. Forchel, R. Sauer, C. W. Tu, *Interface-roughness-controlled exciton mobilities in* $GaAs/Al_{0.37}Ga_{0.63}As$ *quantum wells*, Phys. Rev. B **42**, 3220–3223 (1990), doi:10.1103/PhysRevB.42.3220

[37] G. Fasol, M. Tanaka, H. Sakaki, Y. Horikoshi, *Interface roughness and the dispersion of confined LO phonons in GaAs/AlAs quantum wells*, Phys. Rev. B **38**, 6056–6065 (1988), doi:10.1103/PhysRevB.38.6056

[38] T. Watanabe, S. Tsurekawa, *The control of brittleness and development of desirable mechanical properties in polycrystalline systems by grain boundary engineering*, Acta Materialia **47**, 4171–4185 (1999), ISSN 1359-6454

[39] T. Watanabe, *Structural effects on grain boundary segregation, hardening and fracture*, Journal de Physique Colloques **46**, C4–555–C4–566 (1985), doi: 10.1051/jphyscol:1985462

[40] T. Watanabe, *Grain boundary design and control for high temperature materials*, Materials Science and Engineering: A **166**, 11–28 (1993), ISSN 0921-5093

[41] A. Schwartz, *The potential engineering of grain boundaries through thermomechanical processing*, JOM Journal of the Minerals, Metals and Materials Society **50**, 50–55 (1998), ISSN 1047-4838, doi:10.1007/s11837-998-0250-5

[42] J. Alvarez-Quintana, E. Martnez, E. Prez-Tijerina, S. A. Prez-Garca, J. Rodrguez-Viejo, *Temperature dependent thermal conductivity of polycrystalline ZnO films*, Journal of Applied Physics **107**, 063713 (2010), ISSN 00218979, doi: 10.1063/1.3330755

[43] Z. X. Huang, Z. A. Tang, J. Yu, S. Bai, *Thermal conductivity of nanoscale polycrystalline ZnO thin films*, Physica B: Condensed Matter **406**, 818–823 (2011), ISSN 0921-4526, doi:10.1016/j.physb.2010.11.099

[44] K. T. Igamberdiev, S. U. Yuldashev, S. S. Kurbanov, T. W. Kang, P. K. Khabibullaev, S. M. Rakhimova, V. O. Pelenovich, A. G. Shashkov, *Thermal properties of semiconductor zinc oxide nanostructures*, Journal of Engineering Physics and Thermophysics **83**, 863 – 868 (2010)

[45] *http://www.bp.com/statisticalreview, bp statistical review of world energy* (2010)

[46] S. Pacala, R. Socolow, *Stabilization wedges: Solving the climate problem for the next 50 years with current technologies*, Science **305**, 968–972 (2004)

[47] M. I. Hoffert, K. Caldeira, A. K. Jain, E. F. Haites, L. D. D. Harvey, S. D. Potter, M. E. Schlesinger, S. H. Schneider, R. G. Watts, T. M. L. Wigley, D. J. Wuebbles, *Energy implications of future stabilization of atmospheric CO_2 content*, Nature **395**, 881–884 (1998), ISSN 0028-0836

[48] *2008 solar technologies market report*, Technical report, U.S. Department of Energy (2010)

[49] A. Feltrin, A. Freundlich, *Material considerations for terawatt level deployment of photovoltaics*, Renewable Energy **33**, 180–185 (2008), ISSN 0960-1481, doi:DOI: 10.1016/j.renene.2007.05.024, e-MRS 2006 Symposium M: Materials, Devices and Prospects for Sustainable Energy, 2006 Spring Meeting of the European Materials Research Society

[50] Bundesverband der Energie- und Wasserwirtschaft, http://www.bdew.de (2011)

[51] J. Vásquez, M. Sanz-Bobi, R. Palacios, A. Arenas, *State of the art of thermoelectric generators based on heat recovered from the exhaust gases of automobiles*, http://www.iit.upcomillas.es/docs/02JVA03.pdf

[52] G. Homm, P. J. Klar, *Thermoelectric materials - compromising between high efficiency and materials abundance*, physica status solidi (RRL) - Rapid Research Letters **5**, 324–331 (2011), ISSN 1862-6270, doi:10.1002/pssr.201105084

[53] G. J. Snyder, E. S. Toberer, *Complex thermoelectric materials*, Nat. Mater. **7**, 105–114 (2008), ISSN 1476-1122

[54] M. Ohtaki, T. Tsubota, K. Eguchi, H. Arai, *High-temperature thermoelectric properties of $(Zn_{1-x}Al_x)O$*, Journal of Applied Physics **79**, 1816–1818 (1996)

[55] C. B. Vining, *Thermoelectric Properties of Silicides* 1–18, http://cvining.com/system/files/articles/vining/Vining-CRC-1995.pdf

[56] A. Patyk, *Thermoelectrics: Impacts on the environment and sustainability*, Journal of Electronic Materials **39**, 2023–2028 (2009)

[57] Verband der deutschen Automobilindustrie (VDA), Annual Report, Frankfurt (2009)

[58] http://www.usgs.gov/minerals/pubs/commodity (2005), US Geological Survey (USGS), Mineral Commodities Summaries

[59] http://www.ist.fraunhofer.de/kompetenz/funktion/trans-parent/frames.html

[60] T. Tritt, H. Böttner, L. Chen, *Thermoelectrics: Direct solar thermal energy conversion*, MRS Bulletin **33**, 366 (2008)

[61] *http://srdata.nist.gov/its90/main/*

[62] J. Nyström, *Thomson coefficients for Copper at high temperatures*, Arkiv För Matematik, Astronomi och Fysik **34A**, 1–27 (1947)

[63] J. Robert R. Heikes, Roland W. Ure, *Thermoelectricity: Science and Engineering*, Interscience Publishers, New York, London (1961)

[64] H. Overhof, P. Thomas, *Electronic transport in hydrogenated amorphous semiconductors*, Springer, Berlin (1989)

[65] D. Platzek, G. Karpinski, C. Drasar, E. Müller, *Seebeck Scanning Microprobe for Thermoelectric FGM*, in *Materials Science Forum*, volume 492, 587–592, Trans Tech Publ (2005)

[66] J. Yaeger, M. Hrusch-Tupta, editors, *Low Level Measurements Handbook: Precision DC Current, Voltage, and Resistance Measurements*, Keithley Instruments Inc., 6 edition (2004)

[67] L. J. van der Pauw, *A method of measuring the resistivity and Hall coeffcient on lamellae of arbitrary shape*, Philips Tech. Rev. **20**, 220 (1958/59)

[68] L. J. van der Pauw, *A method of measuring specific resistivity and Hall effect of discs of arbitrary shape*, Philips Res. Repts. **13**, 1–9 (1958)

[69] E. Synge, *A suggested method for extending microscopic resolution into the ultra-microscopic region*, Philosophical Magazine Series 7 **6**, 356–362 (1928), doi: 10.1080/14786440808564615

[70] E. Synge, *XXIII. An application of piezo-electricity to microscopy*, Philosophical Magazine Series 7 **13**, 297–300 (1932), doi:10.1080/14786443209461931

[71] G. Binnig, H. Rohrer, C. Gerber, E. Weibel, *Tunneling through a controllable vacuum gap*, Applied Physics Letters **40**, 178–180 (1982), doi:10.1063/1.92999

[72] G. Binnig, H. Rohrer, *Scanning tunneling microscopy*, Surface Science **126**, 236 – 244 (1983), ISSN 0039-6028, doi:10.1016/0039-6028(83)90716-1

[73] G. Binnig, C. F. Quate, C. Gerber, *Atomic Force Microscope*, Phys. Rev. Lett. **56**, 930–933 (1986), doi:10.1103/PhysRevLett.56.930

[74] F. J. Giessibl, *Advances in atomic force microscopy*, Rev. Mod. Phys. **75**, 949–983 (2003), doi:10.1103/RevModPhys.75.949

[75] F. Ruiz, W. D. Sun, F. H. Pollak, C. Venkatraman, *Determination of the thermal conductivity of diamond-like nanocomposite films using a scanning thermal microscope*, Applied Physics Letters **73**, 1802–1804 (1998), doi:10.1063/1.122287

[76] A. Hammiche, H. M. Pollock, M. Song, D. J. Hourston, *Sub-surface imaging by scanning thermal microscopy*, Measurement Science and Technology **7**, 142 (1996)

[77] A. Hammiche, M. Reading, H. M. Pollock, M. Song, D. J. Hourston, *Localized thermal analysis using a miniaturized resistive probe*, Review of Scientific Instruments **67**, 4268–4274 (1996), doi:10.1063/1.1147525

[78] R. B. Dinwiddie, R. J. Pylkki, P. E. West, Therm. Conduct. **22**, 668 (1994)

[79] J. Weidlein, U. Müller, K. Denicke, *Schwingungsspektroskopie - Eine Einführung*, Georg Thieme Verlag Stuttgart (1988)

[80] C. Raman, K. Krishnan, *A new type of secondary radiation*, Nature **121**, 501–502 (1928)

[81] M. J. Madou, *Fundamentals of Microfabrication - The Science of Miniaturization*, CRCPress (2002), ISBN 0-8493-0826-7

[82] M. Piechotka, *Magnetotransport und Untersuchungen von Ätzschädigungen an mikrostrukturierten $Zn_{1-x}Al_xO$- und ZnO-Schichten*, Diploma thesis, Justus-Liebig-Universität Gießen (2008)

[83] F. Völklein, T. Zetterer, *Praxiswissen Mikrosystemtechnik*, Vieweg Praxiswissen (2006), ISBN 3-528-13891-2

[84] M. T. Elm, T. Henning, P. J. Klar, B. Szyszka, *Effects of artificially structured micrometer holes on the transport behavior of Al-doped ZnO layers*, Applied Physics Letters **93**, 232101 (2008), ISSN 00036951, doi:10.1063/1.3040312

[85] micro resist technology GmbH, Koepenicker Straße 325, 12555 Berlin-Koepenick, Germany, *ma-N 400 and ma-N 1400 - Negative Tone Photoresists* (2011)

[86] P. Debye, *Zur Theorie der spezifischen Wärmen*, Annalen der Physik **344**, 789–839 (1912), ISSN 1521-3889, doi:10.1002/andp.19123441404

[87] C. Kittel, *Einführung in die Festkörperphysik*, R. Oldenbourg Verlag GmbH, München; 14. Auflage (2006)

[88] R. Peierls, *Zur kinetischen Theorie der Wärmeleitung in Kristallen*, Annalen der Physik **395**, 1055–1101 (1929), ISSN 1521-3889, doi:10.1002/andp.19293950803

[89] A. Eucken, *Über die Temperaturabhängigkeit der Wärmeleitfähigkeit fester Nichtmetalle*, Annalen der Physik **339**, 185–221 (1911), ISSN 1521-3889, doi:10.1002/andp.19113390202

[90] H. Goldsmid, *Thermoelectric Refrigeration*, Pion Limited, London (1986)

[91] H. Goldsmid, A. Penn, *Boundary scattering of phonons in solid solutions*, Physics Letters A **27**, 523 – 524 (1968), ISSN 0375-9601, doi:10.1016/0375-9601(68)90898-0

[92] R. Paul, *Halbleiterphysik*, Dr. Alfred Hüthig Verlag Heidelberg (1975)

[93] M. Bachmann, M. Czerner, C. Heiliger, *Calculation of Thermoelectric Transport Properties in Heterostructures*, Journal of Electronic Materials **40**, 577–582 (2011), ISSN 0361-5235, 10.1007/s11664-010-1458-z

[94] J. Y. W. Seto, *The electrical properties of polycrystalline silicon films*, Journal of Applied Physics **46**, 5247–5254 (1975), doi:10.1063/1.321593

[95] S. Datta, *Electronic Transport in Mesoscopic Systems*, Cambridge University Press (1995), ISBN-13: 978-0521599436

[96] S. Datta, *Quantum Transport: Atom to Transistor*, Cambridge University Press (2005), ISBN-13: 978-0521631457

[97] C. Heiliger, M. Czerner, B. Y. Yavorsky, I. Mertig, M. D. Stiles, *Implementation of a nonequilibrium Green's function method to calculate spin-transfer torque*, Journal of Applied Physics **103**, 07A709 (2008), doi:10.1063/1.2835071

[98] C. Jeong, R. Kim, M. Luisier, S. Datta, M. Lundstrom, *On Landauer versus Boltzmann and full band versus effective mass evaluation of thermoelectric transport coefficients*, Journal of Applied Physics **107**, 023707 (2010), doi:10.1063/1.3291120

[99] U. Sivan, Y. Imry, *Multichannel Landauer formula for thermoelectric transport with application to thermopower near the mobility edge*, Phys. Rev. B **33**, 551–558 (1986), doi:10.1103/PhysRevB.33.551

[100] C. R. Proetto, *Thermopower oscillations of a quantum-point contact*, Phys. Rev. B **44**, 9096–9099 (1991), doi:10.1103/PhysRevB.44.9096

[101] X. Gonze, G.-M. Rignanese, M. Verstraete, J.-M. Beuken, Y. Pouillon, R. Caracas, F. Jollet, M. Torrent, G. Zerah, M. Mikami, P. Ghosez, M. Veithen, J.-Y. Raty, V. Olevano, F. Bruneval, L. Reining, R. Godby, G. Onida, D. R. Hamann, D. C. Allan, *A brief introduction to the ABINIT software package*, Zeitschrift für Kristallographie **220**, 558–562 (2005)

[102] W. Zhang, T. S. Fisher, N. Mingo, *The Atomistic Green's Function Method: An Efficient Simulation Approach for Nanoscale Phonon Transport*, Numerical Heat Transfer, Part B: Fundamentals **51**, 333–349 (2007), doi:10.1080/10407790601144755

[103] W. Zhang, T. S. Fisher, N. Mingo, *Simulation of Interfacial Phonon Transport in Si–Ge Heterostructures Using an Atomistic Green's Function Method*, Journal of Heat Transfer **129**, 483–491 (2007), doi:10.1115/1.2709656

[104] N. Mingo, L. Yang, *Phonon transport in nanowires coated with an amorphous material: An atomistic Green's function approach*, Phys. Rev. B **68**, 245406 (2003), doi:10.1103/PhysRevB.68.245406

[105] P. E. Hopkins, P. M. Norris, M. S. Tsegaye, A. W. Ghosh, *Extracting phonon thermal conductance across atomic junctions: Nonequilibrium Green's function approach compared to semiclassical methods*, Journal of Applied Physics **106**, 063503 (2009), doi:10.1063/1.3212974

[106] E. T. Swartz, R. O. Pohl, *Thermal boundary resistance*, Rev. Mod. Phys. **61**, 605–668 (1989), doi:10.1103/RevModPhys.61.605

[107] X. Gonze, *First-principles responses of solids to atomic displacements and homogeneous electric fields: Implementation of a conjugate-gradient algorithm*, Phys. Rev. B **55**, 10337–10354 (1997), doi:10.1103/PhysRevB.55.10337

[108] X. Gonze, C. Lee, *Dynamical matrices, Born effective charges, dielectric permittivity tensors, and interatomic force constants from density-functional perturbation theory*, Phys. Rev. B **55**, 10355–10368 (1997), doi:10.1103/PhysRevB.55.10355

[109] N. Troullier, J. L. Martins, *Efficient pseudopotentials for plane-wave calculations*, Phys. Rev. B **43**, 1993–2006 (1991), doi:10.1103/PhysRevB.43.1993

[110] X. Zhang, B. Sun, H. Guo, N. Tetreault, H. Giessen, R. H. Friend, *Large-area two-dimensional photonic crystals of metallic nanocylinders based on colloidal gold nanoparticles*, Applied Physics Letters **90**, 133114 (2007), doi: 10.1063/1.2717567

[111] W. Seifert, M. Ueltzen, E. Müller, *One-dimensional Modelling of Thermoelectric Cooling*, physica status solidi (a) **194**, 277–290 (2002), ISSN 1521-396X, doi:10.1002/1521-396X(200211)194:1¡277::AID-PSSA277¿3.0.CO;2-5

[112] S. Major, A. Banerjee, K. L. Chopra, *Annealing studies of undoped and indium-doped films of zinc oxide*, Thin Solid Films **122**, 31 – 43 (1984), ISSN 0040-6090, doi:DOI: 10.1016/0040-6090(84)90376-6

[113] H. P. R. Frederikse, *Thermoelectric power of Germanium below room temperature*, Physical Review **92**, 248–252 (1953)

[114] C. Herring, *Theory of the thermoelectric power of semiconductors*, Physical Review **96**, 1163–1187 (1954)

[115] E. Bruno, B. Ginatempo, E. Guiliano, A. Ruban, Y. Vekilov, *Fermi surfaces and electronic topological transitions in metallic solid solutions*, Physics Reports **249**, 353 – 419 (1994), ISSN 0370-1573, doi:10.1016/0370-1573(94)90056-6

[116] J. Serre, A. Ghazali, *From band tailing to impurity-band formation and discussion of localization in doped semiconductors: A multiple-scattering approach*, Phys. Rev. B **28**, 4704–4715 (1983)

[117] N. F. Mott, H. Jones, *The theory of the properties of metals and alloys*, Clarendon Press, Oxford (1936)

[118] K. Kishimoto, M. Tsukamoto, T. Koyanagi, *Temperature dependence of the Seebeck coefficient and the potential barrier scattering of n-type PbTe films prepared on heated glass substrates by RF sputtering*, Journal of Applied Physics **92**, 5331–5339 (2002)

[119] J. Bardeen, *Surface states and rectification at a metal semi-conductor contact*, Physical Review **71**, 717–727 (1947)

[120] M. Bachmann, M. Czerner, C. Heiliger, *The ineffectiveness of energy filtering at grain boundaries for thermoelectric materials*, to be published

[121] T. C. Harman, P. J. Taylor, M. P. Walsh, B. E. LaForge, *Quantum Dot Superlattice Thermoelectric Materials and Devices*, Science **297**, 2229–2232 (2002)

[122] W. Kim, J. Zide, A. Gossard, D. Klenov, S. Stemmer, A. Shakouri, A. Majumdar, *Thermal Conductivity Reduction and Thermoelectric Figure of Merit Increase by Embedding Nanoparticles in Crystalline Semiconductors*, Phys. Rev. Lett. **96**, 045901–1–045901–4 (2006)

[123] L. D. Hicks, T. C. Harman, M. S. Dresselhaus, *Use of quantum-well superlattices to obtain a high figure of merit from nonconventional thermoelectric materials*, Applied Physics Letters **63**, 3230–3232 (1993)

[124] S. V. Faleev, F. m. c. Léonard, *Theory of enhancement of thermoelectric properties of materials with nanoinclusions*, Phys. Rev. B **77**, 214304 (2008), doi: 10.1103/PhysRevB.77.214304

[125] K. M. Katika, L. Pilon, *The effect of nanoparticles on the thermal conductivity of crystalline thin films at low temperatures*, Journal of Applied Physics **103**, 114308 (2008), doi:10.1063/1.2937208

[126] J. Sharp, S. Poon, H. Goldsmid, *Boundary scattering and the thermoelectric figure of merit*, phys. stat. sol. (a) **187**, 507–516 (2001), ISSN 1521-396X

[127] Ü. Özgür, Y. I. Alivov, C. Liu, A. Teke, M. A. Reshchikov, S. Dogan, V. Avrutin, S.-J. Cho, H. Morkoc, *A comprehensive review of ZnO materials and devices*, Journal of Applied Physics **98, 041301**, 1–103 (2005)

[128] V. V. Ursaki, I. M. Tiginyanu, V. V. Zalamai, E. V. Rusu, G. A. Emelchenko, V. M. Masalov, E. N. Samarov, *Multiphonon resonant Raman scattering in* ZnO *crystals and nanostructured layers*, Phys. Rev. B **70**, 155204 (2004), doi:10.1103/PhysRevB.70.155204

[129] J. G. Lu, S. Fujita, T. Kawaharamura, H. Nishinaka, Y. Kamada, T. Ohshima, Z. Z. Ye, Y. J. Zeng, Y. Z. Zhang, L. P. Zhu, H. P. He, B. H. Zhao, *Carrier concentration dependence of band gap shift in n-type ZnO:Al films*, Journal of Applied Physics **101**, 083705 (2007), doi:10.1063/1.2721374

[130] G. Abstreiter, M. Cardona, A. Pinczuk, *Light Scattering in Solids IV*, Springer, Berlin (1984)

[131] F. Gather, C. Heiliger, P. Klar, *Nemo: A network model program for analyzing the thermoelectric properties of meso and nanostructured composite materials*, Progress in Solid State Chemistry – (2011), ISSN 0079-6786, doi: 10.1016/j.progsolidstchem.2011.10.001

[132] F. Gather, C. Heiliger, P. J. Klar, *Modeling of interface roughness in thermoelectric composite materials*, Journal of Physics: Condensed Matter **23**, 335301 (2011)

List of publications

- G. Homm, P. J. Klar, J. Teubert, W. Heimbrodt, *Seebeck coefficients of n-type (Ga,In)(N,As), (B,Ga,In)As, and GaAs*, Appl. Phys. Lett. **93**, 042107 (2008)
- G. Homm, J. Teubert, T. Henning, P. J. Klar, B. Szyszka, *Seebeck effect of as-grown and micro-structured metallic (Zn,Al)O*, Phys. Status Solidi C **7**, 1602 (2010)
- G. Homm, M. Piechotka, A. Kronenberger, A. Laufer, F. Gather, D. Hartung, C. Heiliger, B. K. Meyer, P. J. Klar, S. O. Steinmüller, J. Janek, *Thermoelectric measurements on sputtered ZnO/ZnS multilayers*, ICT 2009 Proceedings, J. Electron. Mater. **39**, 1504 (2010)
- G. Homm, S. Petznick, F. Gather, T. Henning, C. Heiliger, B. K. Meyer und P. J. Klar, *Effect of Interface Regions on the Thermoelectric Properties of Alternating ZnO/ZnO:Al Stripe Structures*, ICT 2010 Proceedings, J. Electron. Mater. **40**, 801 (2011)
- G. Homm, and P. J. Klar, *Thermoelectric materials - Compromising between high efficiency and materials abundance*, physica status solidi (RRL) - Rapid Research Letters **5**, 324 (2011)
- G. Homm, F. Gather, A. Kronenberger, M. Becker, B. K. Meyer, P. J. Klar, P. Ziolkowski, and E. Müller, *Correlation of local and global thermoelectric properties in laterally structured thermoelectric materials*, ECT 2011 Proceedings, submitted to AIP Conference Proceedings (2011)
- G. Homm, S. Petznick, T. Henning, and P. J. Klar, *Photolithography and self-aligned subtractive and additive patterning of conductive materials* in Materials Science and Technology, ISBN 978-953-51-0193-2, Intech open access publisher (2012)

Acknowledgements

Diese Arbeit ist erst durch die Mithilfe vieler Personen in meinem universitären - , aber auch im privaten Umfeld möglich geworden. Hier sei nun den Wichtigsten dafür gedankt. Bei der Reihenfolge möge man mir jedoch nicht allzuviel Absicht unterstellen. Jeder wird sicher selbst einen guten Grund dafür finden, warum seine Unterstützung die Wichtigste war.
Besonders danke ich:

Prof. Dr. Peter J. Klar für die Aufnahme in seine Arbeitsgruppe und die langjährige (es sind mittlerweile tatsächlich fünf Jahre) wunderbare Betreuung.

Prof. Dr. Bruno K. Meyer nicht nur für die Übernahme des Zweitgutachtens, sondern auch viele amüsante, teilweise zungenbrecherische Stunden im Blauen Salon.

Dr. Torsten Henning für die stets kompetente Hilfe beim Lösen vieler Probleme im Reinraum.

Dem Büro der Dienstältesten für ein echt tolles Klima am Arbeitsplatz; ich bin wirklich nie mit einem unangenehmen Gefühl ins Institut gegangen - im einzelnen Markus Piechotka für fachliche Ratschläge mit Hand und Fuß und für seinen scharfsinnigen Sinn für Humor , Dr. Matthias 'Max' Elm für seine stets gute Laune (außer beim Bonden), David Hartung für seine stetige Hilfsbereitschaft, oft auch auerhalb der Arbeitszeiten, Thomas Sander merci ... beaucoup für viele Hilfestellungen die optischen Messungen betreffend sowie sein offensichtliches Unvermögen ein "Nein" über die Lippen zu bringen, und als Ehemaliger dieses eloquenten Kreises Dr. Jörg Teubert für die ausgezeichnete Einführung in die Thermoelektrik und dafür dass er stets ein offenes Ohr für mich hatte.

Dem Nachbar-Büro für viel gute Laune - im einzelnen Julian Benz für zahlreiche Tips und Tricks im Reinraum, Sabrina Darmawi dafür, dass man auch mal Gespräche über andere Themen als Physik führen konnte, Steve Petznik dafür, dass er mich ein Stück in der Thermoelektrik begleitet hat, und last but not least Martin Fischer für zeitnahes und zuverlässiges Trockenätzen .

Dem Kinderzimmer für ihren jugedlichen Übermut - im einzelnen Florian Gather für seine kompetente Unterstützung beim Arbeiten mit dem Netzwerkmodell, Christian Will für viele Transport-Messungen, Tobias Lind dafür, dass er sich entschieden hat Thermoelektriker zu werden, um den ersten auf Oxiden basierernden Thermogenerator zu bauen.

Der AG Heiliger für den stets netten Empfang und die enge Zusammenarbeit in der Thermoelektrik - vor allem Prof. Dr. Christian Heiliger für viele interessante Gespräche (nicht immer nur über Thermoelektik) sowie Michael Bachmann für seine theoretischen Rechnungen zum thermoelektrischen Transport über Korngrenzen und seine stetigen Bemühungen

sein Wissen mit mir zu teilen.

Für die Bereitstellung der Proben: Prof. Dr. Martin Eickhoff für MBE gewachsene ZnO Schichten, Dr. Stefan Lautenschläger sowie Dr. Sebastian Eisermann für die CVD gewachsenen ZnO Schichten, Dr. Bernd Szyszka und vor allem Achim Kronenberger für die zahlreichen gesputterten Proben, denen ich im Reinraum teilweise übel mitgespielt habe bis etwas verwertbares heraus gekommen ist.

Allen Korrekturlesern.

Meinen Freunden die neben der Uni wieder für den nötigen Abstand zur Physik gesorgt haben.

Meiner Familie für viele Dinge, die ich hier im einzelnen gar nicht aufzählen kann. Kurz gesagt habe ich bei ihr immer genau die Unterstützung bekommen, die ich in dem Moment gebraucht habe.

Meiner Süßen, Gaby, dafür, dass sie immer an mich geglaubt hat und mir damit die Kraft gegeben hat, diese Arbeit nicht nur anzugehen sondern auch zu beenden.

VIELEN DANK!

Ich erkläre:

Ich habe die vorgelegte Dissertation selbstständig und ohne unerlaubte fremde Hilfe und nur mit den Hilfen angefertigt, die ich in der Dissertation angegeben habe. Alle Textstellen, die wörtlich oder sinngemäß aus veröffentlichten Schriften entnommen sind, und alle Angaben, die auf mündlichen Auskünften beruhen, sind als solche kenntlich gemacht. Bei den von mir durchgeführten und in der Dissertation erwähnten Untersuchungen habe ich die Grundsätze guter wissenschaftlicher Praxis, wie sie in der Satzung der Justus-Liebig Universität Gießen zur Sicherung guter wissenschaftlicher Praxis niedergelegt sind, eingehalten.

Gert Homm